

Ring of fire as a novel approach to study cycling aerodynamics

Spoelstra, A.M.C.M.G.

DOI

[10.4233/uuid:5b51be97-aca7-4935-836a-be9b75f819df](https://doi.org/10.4233/uuid:5b51be97-aca7-4935-836a-be9b75f819df)

Publication date

2022

Document Version

Final published version

Citation (APA)

Spoelstra, A. M. C. M. G. (2022). *Ring of fire as a novel approach to study cycling aerodynamics*. [Dissertation (TU Delft), Delft University of Technology]. <https://doi.org/10.4233/uuid:5b51be97-aca7-4935-836a-be9b75f819df>

Important note

To cite this publication, please use the final published version (if applicable). Please check the document version above.

Copyright

Other than for strictly personal use, it is not permitted to download, forward or distribute the text or part of it, without the consent of the author(s) and/or copyright holder(s), unless the work is under an open content license such as Creative Commons.

Takedown policy

Please contact us and provide details if you believe this document breaches copyrights. We will remove access to the work immediately and investigate your claim.

**RING OF FIRE AS A NOVEL APPROACH TO STUDY
CYCLING AERODYNAMICS**



RING OF FIRE AS A NOVEL APPROACH TO STUDY CYCLING AERODYNAMICS

Dissertation

for the purpose of obtaining the degree of doctor
at Delft University of Technology,
by the authority of the Rector Magnificus, Prof.dr.ir. T.H.J.J. van der Hagen,
chair of the Board for Doctorates,
to be defended publicly on
Friday 18 February 2022 at 12:30 o'clock

by

Alexander Marc Carl Maartin Graad SPOELSTRA

Master of Science in Aerospace Engineering,
Delft University of Technology, the Netherlands,
born in Halle, Belgium.

This dissertation has been approved by the promotors.

Composition of the doctoral committee:

Rector Magnificus,	chairperson
Prof.dr.ir. F. Scarano,	Delft University of Technology, promotor
Dr.ir. A. Sciacchitano,	Delft University of Technology, copromotor

Independent members:

Prof.dr.ir. W. van de Water,	Delft University of Technology
Prof.dr.ir. B.J.E. Blocken,	Eindhoven University of Technology
Dr.ir. T.N. Crouch,	Monash University
Dr.ir. D.E. Rival,	Queen's University
Ir. H.H. Ubbens,	Team DSM
Prof.dr.ir. L.L.M. Veldhuis,	Delft University of Technology, reserve member



Keywords: Large scale PIV, Helium Filled Soap Bubbles, On-site drag evaluation, sports aerodynamics

Cover design: Irene Rodríguez Martín

ISBN 978-94-6366-467-7

Copyright © 2021 by A.M.C.M.G. Spoelstra

Printed by Ipskamp printing

An electronic version of this dissertation is available at

<http://repository.tudelft.nl/>.

In memory of my mother



CONTENTS

Summary	xi
Samenvatting	xiii
I Prologue	1
1 Introduction	3
2 Cycling aerodynamics	9
2.1 History	10
2.2 Importance of aerodynamics in cycling	12
2.3 Aerodynamic research methods.	13
2.3.1 Wind tunnel	13
2.3.2 Computational fluid dynamics (CFD)	14
2.3.3 Track and road tests	15
2.4 Single-rider aerodynamics	16
2.4.1 Cyclist position and geometry	16
2.4.2 Cyclist flow topology.	18
2.5 Multi-rider aerodynamics and drafting	22
2.5.1 Effect of distance.	23
2.5.2 Effect of cyclist size, posture and position	25
2.5.3 Drag reduction of leading cyclist.	28
2.5.4 Flow topology	29
3 Particle Image Velocimetry	33
3.1 Working principle.	34
3.2 Stereoscopic PIV	35
3.3 Large-scale PIV	36
3.3.1 Helium-filled soap bubbles tracers.	36
3.3.2 State-of-the-art HFSB seeding systems.	37
3.4 Loads determination from PIV	38
3.4.1 Momentum integral contour-approach	38
3.4.2 Pressure evaluation from PIV	40
3.5 PIV in cycling aerodynamic research	41
3.6 The Ring of Fire	43
II Development and assessment of the Ring of Fire system	45
4 Feasibility and full scale assessment	47
4.1 Introduction	48

4.2	Methodology	48
4.3	Experimental setup and procedures	50
4.3.1	Experimental facilities and cycling conditions	51
4.3.2	PIV instrumentation, imaging and data acquisition	51
4.3.3	Data processing	55
4.3.4	Measurement procedure.	57
4.4	Results and discussion	58
4.4.1	Quantitative flow visualization.	58
4.4.2	Aerodynamic drag analysis.	62
4.5	Conclusions.	65
5	Assessment of Ring of Fire drag resolution	67
5.1	Introduction	68
5.2	Power meter drag evaluation technique.	68
5.3	Experimental setup and procedures	69
5.3.1	Test facility and subject	69
5.3.2	Power meter measurement system.	71
5.3.3	Ring of Fire measurement system	71
5.3.4	Measurement protocol.	72
5.4	Data reduction and analysis techniques	72
5.4.1	Power meter	72
5.4.2	Ring of Fire: particle image velocimetry	73
5.4.3	Ring of Fire: control volume approach.	74
5.5	Results and discussion	75
5.5.1	<i>A priori</i> uncertainty estimation	75
5.5.2	Effect of mass conservation	77
5.5.3	Sensitivity to the measurement's spatial resolution	78
5.5.4	Comparison with power meter drag estimation	79
5.6	Conclusions.	81
III	Applications	83
6	Drafting in cycling	85
6.1	Introduction	86
6.2	Adaptation of the methodology.	87
6.3	Experimental setup and procedures	88
6.3.1	Facility and experimental conditions	88
6.3.2	PIV system	89
6.3.3	Data reduction.	89
6.4	Results and discussion	91
6.4.1	Effect of the human factor	91
6.4.2	Single cyclist	92
6.4.3	Tandem configuration	95
6.4.4	Modelling drag reduction	99
6.5	Conclusions.	101

7	Speed skating	103
7.1	Introduction	104
7.2	Experimental setup and procedures	105
7.2.1	Test facility and subjects	105
7.2.2	PIV system	107
7.2.3	Measurement procedure.	107
7.2.4	Data reduction.	108
7.3	Results	109
7.3.1	Environmental airflow conditions before transit	109
7.3.2	Flow visualizations for the different skating phases	111
7.3.3	Flow visualizations for skater A: Two arms vs. one arm on the back (Case 1)	112
7.3.4	Flow visualizations for skater B: Low trunk vs. high trunk (Case 2)	114
7.3.5	Drag analysis.	115
7.4	Conclusions.	118
IV	Epilogue	119
8	Conclusions and outlook	121
8.1	Measurement system	122
8.1.1	Feasibility and full scale assessment	122
8.1.2	Assessment of the drag resolution	122
8.2	Applications in speed sports	123
8.2.1	Drafting in cycling	123
8.2.2	Speed skating	123
8.3	Outlook	124
8.3.1	Application in automotive industry	124
8.3.2	Future prospects.	126
A	Energized mass concept for drag determination	127
	References	131
	Acknowledgements	143
	Curriculum Vitæ	145
	List of Publications	147



SUMMARY

The research presented in this thesis introduces a new measurement concept for on-site aerodynamic measurements based on large-scale stereoscopic particle image velocimetry (stereo-PIV) measurements past an athlete, a vehicle or an object travelling through a quiescent environment. The analysis of the momentum deficit past the transit poses the basis to estimate the aerodynamic drag. For such an approach, where the object crosses the illuminated measurement plane, the experimental method is referred with the name “Ring of Fire” (RoF).

The first part of this work presents the development and assessment of the Ring of Fire concept through the study of cycling aerodynamics. A feasibility study is performed in which two RoF experiments with a cyclist are conducted, indoor and outdoor, mimicking respectively track and road cycling. During these experiments attention is placed on the effects of the environmental conditions and the confinement of the measurement region. Furthermore, the experiments cover different postures of the cyclist (time trial and upright) with the aim to directly measure the effect of posture on aerodynamic drag and its detectability with the RoF. Despite differences between the two experiments in the cyclist geometry, bike geometry, and the cycling speed, the flow fields in the near wake of the riders compare well between both experiments and to literature. In terms of drag estimation, a clear distinction in upright vs. time trial drag area is found for both experiments, with the upright posture yielding higher drag area by about 20-35% with respect to the time trial posture. The comparison of these drag values with literature data, however, could not yield a conclusive assessment, given the large dispersion (approx. 50%) of the literature data due to many varying parameters, like rider posture, bikes geometries and testing conditions. Furthermore, the uncertainty of the measured drag and its dependency upon experimental conditions and the image processing parameters have not yet been addressed. Knowledge of the minimum detectable drag variation is relevant when measurements are intended to perform aerodynamic optimisation, therefore, a sensitivity analysis is conducted that assesses how the estimated drag is affected by the choice of PIV image processing parameters. The size of the cross-section considered in the control volume formulation is also investigated. It is found that the accuracy of the estimated drag depends on the procedure used to detect the edge of the momentum deficit region in the wake. Moreover imposing mass conservation yields the most accurate drag measurements. The drag estimation has little dependence upon the spatial resolution of the measurement as long as the interrogation window size stays within 5% to 25% of the equivalent diameter of the object cross section. In addition, the drag values obtained with the RoF are compared against the drag estimates from simultaneously acquired power meter data. To assess the agreement between the two approaches in different regimes, drag variations are introduced by different cyclist postures, as well as varying garments. Regardless of the underlying input parameters in the power meter model, both small- and large scale deltas are well captured by both the Ring of Fire

technique and the power meter approach. The uncertainty on the average drag measurements from the RoF is within 5%.

The second part of this work implements the findings and conclusions from part 1 and presents two applications in speed sports studied with the Ring of Fire. Firstly, the effect of drafting in cycling is investigated. More precisely, the amount of drag reduction experienced by a trailing cyclist in a tandem formation is investigated at different lateral and longitudinal separations. The longitudinal displacement of the drafters varied between 0.32 m and 0.85 m and the lateral displacement varied between ± 0.20 m among different runs. The results show that the amount of drag reduction for the trailing rider is mainly caused by the change in inflow conditions and that its aerodynamic advantage decreases with increasing lateral and longitudinal separation between riders, where the lateral distance is found to produce a more rapid effect. Based on these results a model is introduced that predicts the aerodynamic gain of the trailing rider based on his or her position with respect to the leading rider. Validation of the model with data from literature shows that in the near wake the model prediction is in line with literature, with an overestimation of the drag reduction when the longitudinal distance is between 0.1 m and 0.3 m. Secondly, the applicability of the RoF to speed skating is demonstrated. An aerodynamic assessment is presented of two elite skaters, each in two different skating configurations at the ice-rink Thialf in Heerenveen, the Netherlands. Both skaters transit 20 times through the RoF, 10 in each skating configurations. Athlete A skates with two hands on the back and with one arm on the back and one loose. Athlete B skates with both arms loose for all the runs, but was varying his knee and trunk angles. All tests were performed at a nominal speed of 11 m/s. Firstly, the wake velocity fields of skater A, with two hands on the back, are presented throughout five different phases of the skate stroke. Significant variations in the distribution of the velocity deficit downstream of the athlete are observed, which suggest corresponding variations in the skater's aerodynamic drag. Secondly, average streamwise velocity and vorticity field for all 4 different postures are presented and compared. Finally, the results show that the difference in drag between two arms loose and one arm loose was found to be not statistically significant. Conversely, the optimization of the trunk and knee angles results in a reduction by 7.5% of the skater's drag.

SAMENVATTING

Het in dit boek gepresenteerde onderzoek introduceert een nieuw meetconcept voor aerodynamische metingen ter plaatse, gebaseerd op grootschalige stereoscopische Particle Image Velocimetry (stereo-PIV) metingen langs een voorwerp of een voertuig dat door een stilstaande omgeving rijdt. De analyse van het impulsverschil tussen de omstandigheden vóór en na de doortocht vormt de basis voor de schatting van de luchtweerstand. Dergelijke methode, waarbij het voorwerp het verlichte meetvlak doorkruist, wordt benoemd met de naam "Ring of Fire" (RoF).

Het eerste deel van dit werk presenteert de ontwikkeling en beoordeling van het Ring of Fire-concept aan de hand van de studie van de fietsaerodynamica. Er wordt een haalbaarheidsstudie uitgevoerd waarbij twee RoF-experimenten met een wielrenner worden uitgevoerd, binnen en buiten, waarbij respectievelijk baan- en wegwielrennen worden nagebootst. Tijdens deze experimenten wordt aandacht besteed aan de effecten van de omgevingsomstandigheden en de begrenzing van het meetgebied. Bovendien bestrijken de experimenten verschillende houdingen van de fietser (tijdrit en rechtopzittend) met het doel het effect van de houding op de luchtweerstand en de detecteerbaarheid daarvan met de RoF rechtstreeks te meten. Ondanks verschillen tussen de twee experimenten in de geometrie van de fietser, het fietsmodel en de fietssnelheid, zijn de stromingsvelden in het zog van de fietsers goed vergelijkbaar tussen beide experimenten en met de literatuur. Wat betreft de schatting van de luchtweerstand is er een duidelijk verschil tussen de rechtopzittende positie en de tijdritpositie, waarbij de rechtopzittende positie een 20-35% hogere luchtweerstand oplevert ten opzichte van de tijdrit positie. De vergelijking van deze weerstandswaarden met literatuurgegevens kon echter geen sluitende beoordeling opleveren, gezien de grote spreiding (ca. 50%) van de literatuurgegevens als gevolg van vele uiteenlopende parameters, zoals de houding van de berijder, de geometrie van de fiets en de testomstandigheden. Bovendien zijn de onzekerheid van de gemeten weerstand en de afhankelijkheid daarvan van de experimentele omstandigheden en de beeldbewerkingsparameters nog niet onderzocht. Kennis van de minimaal waarneembare weerstandsvariatie is relevant wanneer metingen bedoeld zijn om aerodynamische optimalisatie uit te voeren, daarom wordt een gevoeligheidsanalyse uitgevoerd die nagaat hoe de geschatte weerstand wordt beïnvloed door de keuze van PIV beeldverwerkingsparameters. De grootte van de dwarsdoorsnede die in wordt gebruikt in de controle volume benadering wordt eveneens onderzocht. Gebleken is dat de nauwkeurigheid van de geschatte luchtweerstand afhangt van de procedure die wordt gebruikt om de rand van het zog te detecteren. Bovendien levert het opleggen van behoud van massa de nauwkeurigste weerstandsmetingen op. De schatting van de luchtweerstand is weinig afhankelijk van de ruimtelijke resolutie van de meting, zolang de grootte van het kleinste meetvenster binnen 5% tot 25% van de equivalente diameter van de doorsnede van het object blijft. Bovendien worden de met de RoF verkregen weerstandswaarden vergeleken met de schattingen van de weerstand uit gelijktijdig verkregen vermogensmeter-

gegevens. Om de overeenkomst tussen de twee benaderingen in verschillende regimes te beoordelen, worden luchtweerstandvariaties geïntroduceerd door verschillende houdingen van de fietser, alsmede door verschillende kledingstukken. Ongeacht de onderliggende inputparameters in het vermogensmetermodel, worden zowel kleine als grote delta's goed in beeld gebracht door zowel de Ring of Fire-techniek als de vermogensmeter methode. De onzekerheid op de gemiddelde weerstandsmetingen van de RoF ligt binnen 5%.

Het tweede deel van dit werk implementeert de bevindingen en conclusies uit deel 1 en presenteert twee toepassingen in snelheidssporten die met de Ring of Fire zijn bestudeerd. Ten eerste wordt het effect van draften in wielrennen onderzocht. Meer bepaald wordt de mate van luchtweerstandvermindering die een achtervolgende fietser in een tandemformatie ondervindt, onderzocht bij verschillende laterale en longitudinale afstanden. De longitudinale verplaatsing van de achtervolgende wielrenner varieerde tussen 0.32 m en 0.85 m en de laterale verplaatsing varieerde tussen ± 0.20 m bij de verschillende testen. De resultaten tonen aan dat de vermindering van de luchtweerstand van de achtervolgende renner voornamelijk wordt veroorzaakt door de verandering in de instroomomstandigheden en dat zijn aerodynamische voordeel afneemt met toenemende laterale en longitudinale afstand tussen de renners, waarbij de laterale afstand een groter effect blijkt te hebben. Gebaseerd op deze resultaten wordt een model geïntroduceerd dat de aerodynamische winst van de achteropkomende rijder voorspelt op basis van zijn of haar positie ten opzichte van de leidende rijder. Validatie van het model met gegevens uit de literatuur laat zien dat de modelvoorspelling in het kielzog in overeenstemming is met de literatuur, met een overschatting van de luchtweerstandvermindering wanneer de lengteafstand tussen 0.1 m en 0.3 m ligt. Ten tweede wordt de toepasbaarheid van de RoF op schaatsen aangetoond. Een aerodynamische beoordeling wordt gepresenteerd van twee topschaatsers, elk in twee verschillende schaatsconfiguraties op de ijsbaan Thialf in Heerenveen, Nederland. Beide schaatsers passeren 20 keer door de RoF, 10 keer in elke schaatsconfiguratie. Atleet A schaatst met twee handen op de rug en met één arm op de rug en één los. Atleet B schaatst met beide armen los voor alle testen, maar varieerde zijn knie- en romphoeken. Alle proeven werden uitgevoerd bij een nominale snelheid van 11 m/s. Ten eerste worden de zogsnelheidsvelden van schaatser A, met twee handen op de rug, gepresenteerd voor vijf verschillende fasen van de schaatsslag. Significante variaties in de verdeling van het snelheidsveld stroomafwaarts van de atleet worden waargenomen, wat overeenkomstige variaties in de aerodynamische weerstand van de schaatser suggereert. Ten tweede worden de gemiddelde stroomsnelheden en het vorticitetsveld voor de vier verschillende houdingen gepresenteerd en vergeleken. Tenslotte tonen de resultaten aan dat het verschil in luchtweerstand tussen twee armen los en één arm los niet statistisch significant is. Daarentegen resulteert de optimalisatie van de romp- en kniehoeken in een vermindering van de luchtweerstand van de schaatser met 7.5%.

I

PROLOGUE



1

INTRODUCTION

Do or do not. There is no try.

Master Yoda - Star wars

Versailles, 23 July 1989. The final stage of the 76th Tour de France, an individual time trial of 24.5 km into Paris. At the start, Laurent Fignon had a comfortable 50 seconds lead on Greg LeMond in the general classification and he was deemed safe, as LeMond would have to make up more than two seconds per kilometer. LeMond, however, completed the stage with an average speed of 54.545 km/h, the fastest individual time trial in the Tour de France until then. Fignon finished in a time that was 58 seconds slower than LeMond, which costed him the victory (Huizinga, 2020).

Comparing the equipment of both riders in Figure 1.1 it is observed that LeMond was equipped with several aerodynamic accessories that gave him the advantage over Fignon: a bicycle with airfoil shaped tubing, a Lycra skinsuit, innovative clip-on triathlon bars, an aerodynamic helmet, an aero water bottle and a disc rear wheel, whereas Fignon used a standard bicycle with cow horn handlebars, front and rear disc wheels, and no helmet (Kyle, 1989). With the knowledge of nowadays, we could safely say that Greg LeMond won that Tour de France thanks to aerodynamics.



Figure 1.1: Pictures taken during the final time trial in the Tour de France of 1989: (a) Laurent Fignon and (b) Greg Lemond

Since the Tour de France in 1989 an ever-increasing effort was made to minimize the aerodynamic drag in cycling. This is maybe the most pronounced in triathlon, where, compared to professional cycling, the rules concerning frame geometry, rider seating position, hydration, and other storage systems, are more relaxed (Crouch et al., 2017). The advancements in aerodynamic optimization are apparent in Figure 1.2.

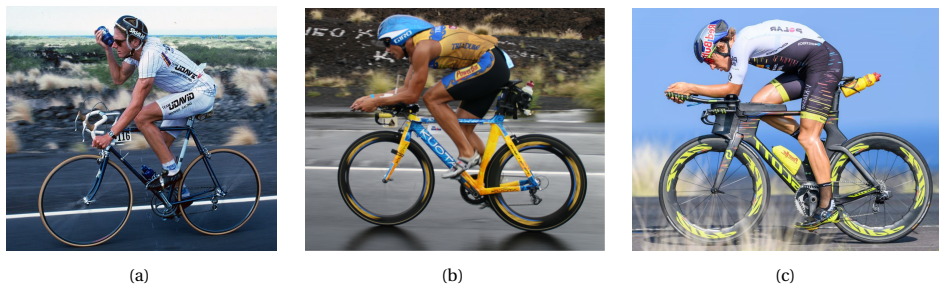


Figure 1.2: (a) Triathlete on normal road bike, 1982. (Allen, 1982) (b) Triathlete breaking course record with 4:18h, 2006. (Hill, 2006) (c) Triathlete riding third fastest bike time in 2017 with 4:14h. (Rauschendorfer, 2017)

During the last four decades the round frame tubes were replaced with airfoil shaped elements and integrated cables and storage solutions were employed to further decrease the drag of the bike. Furthermore, deep rim bike wheels, aerodynamically shaped helmets, and long-sleeve skin suits proved to be very effective in the pursuit of drag reduction. In their efforts to improve the aerodynamic efficiency, athletes and coaches are now focussing on the smallest details. Figure 1.3 shows an example where a titanium aero bar pair has been individually designed and 3D printed for a customized fit with the athlete's arm, closing the existing gap between the round tubed extension and the lower arm itself. This novel solution is claimed to lower the aerodynamic drag by 1–2%.



Figure 1.3: (a) Baseline extension bar setup, with existing gap (Hilger, 2018). (b) Innovative 3D printed aerobars, individually shaped to fit the cyclist's arm (Rauschendorfer, 2018).

Aerodynamics optimizations of athletes generally consist of measurements of aerodynamic loads through wind tunnel experiments (Figure 1.4a). The aerodynamic force is directly measured by connecting the cyclist or model to a force balance. These types of measurements are very accurate and repeatable; however, in some cases they struggle to reproduce realistic conditions due to, for example, the presence of model supports, the dynamical situation to be simulated (e.g. a cycling or running athlete or rotating wheels), the ground effect, or the scale of the object. As a result, the problem is often simplified, reverting to a stationary scaled model to match the constraints imposed by the wind tunnel size and the measurement techniques used for the aerodynamic analysis. Furthermore, some specific cases such as the study of accelerating or decelerating, cornering, or the effects of cycling in group are difficult to reproduce in the wind tunnel environment.

A higher level of realism in the experimental conditions can be obtained by field tests (Figure 1.4b). Established methods for determining on-road aerodynamic drag are the coast-down (Buckley, 1995) and steady-state torque tests (Debraux et al., 2011). The former estimates the aerodynamic drag by the rate of deceleration, the latter utilizes the power output to extract the aerodynamic resistance based on the balance of power. In recent years, the steady-state torque test has become the most practised method in cycling. Compared to the coast down method, the steady torque method has the advantage that it can measure all forces opposing the cycling movement. However, it has the disadvantage that the torque sensor is expensive. When comparing both on-site techniques

with wind tunnel measurements, the advantages of more realistic flow conditions and lower costs are counterbalanced by an increased uncertainty deriving from additional error sources, such as the less-controlled atmospheric conditions and the physical modelling of non-aerodynamic resistance forces, e.g. due to rolling resistance and drive train losses. Moreover, while the on-site techniques adopted so far do provide direct access to the aerodynamic drag, they give no indication of the flow behaviour. The latter is necessary when the physical sources of aerodynamic drag need to be identified and possibly minimised.

When the primary interest of the research is the flow visualisation, the investigation can be conducted by means of computational fluid dynamics (CFD) simulations (Figure 1.4c). Advancements in meshing and turbulence modelling in recent years have made CFD a popular method of investigating cycling aerodynamics (Blocken et al., 2013; Defraeye et al., 2014; Griffith et al., 2014, among others). CFD simulations have several clear advantages. They allow full control of the cyclists' posture, as well as of the incoming flow properties; furthermore, they provide both the aerodynamic drag and the flow field around the cyclists. The aerodynamic forces can even be broken up into their constituent viscous and pressure components, which is useful for flow diagnostics. However, when applied to three-dimensional unsteady flows such as those around athletes, these simulations often suffer from low accuracy and require validation experiments. Furthermore, steady models are typically used, which give little information about the actual aerodynamics occurring during competitions, when the athlete is in motion. Finally, skin properties such as surface roughness of garments cannot be accurately modelled in numerical simulations.

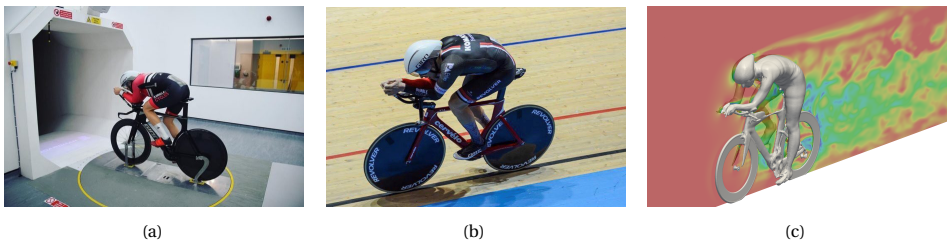


Figure 1.4: Aerodynamic research methods in cycling: (a) Wind tunnel testing (Revolver, 2021) (b) Field testing (Revolver, 2021) (c) CFD simulations (Duncan, 2017)

There seems to be an important disconnection in conventional methods of aerodynamic analysis (wind tunnel, CFD and track tests) between quantitative drag determination, flow field visualization and reproducibility of realistic conditions. Current approaches for estimating drag rely upon force measurements in wind tunnels, determination of the mechanical power delivered by the athlete during training, or computer simulations. The first two types of measurements are “blind”, in that they do not provide a cause-effect relation between the flow behaviour and the resulting aerodynamic drag. Hence, they fail to provide in-depth understanding, precluding a systematic optimisation that minimise the drag. CFD simulations, on the other hand, lack the accuracy required to optimise small-scale changes. As is summarised in Table 1.1, there is currently no measurement technique available that combines high accuracy drag measurements,

high realism, and flow visualization capabilities.

Table 1.1: Summary of the advantages and disadvantages of the current state-of-the-art methods of assessment

	Accurate drag measurements	Flow visualizations	High realism
Wind tunnel	+	+/-	-
CFD	-	+	-
Track tests	-	-	+

This booklet therefore introduces a new measurement system, the Ring of Fire (RoF), that fulfils all these requirements. It is based on large-scale stereoscopic particle image velocimetry (stereo-PIV) measurements past an object or a vehicle travelling through a quiescent environment. The analysis of the momentum difference between the conditions prior to and after the transit poses the basis to estimate the aerodynamic drag. Figure 1.5 presents a schematic representation of how the Ring of Fire initially was envisaged when the idea was introduced by Sciacchitano et al. (2015). The RoF has the potential to enable systematic aerodynamic training for athletes, replacing lengthy and subjective trial-and-error training procedures. Along with its applications in speed sports, it can be relevant to the automotive sector. It can aid in investigating the flow field around ground vehicles in test tracks aimed at minimizing CO_2 emissions, and it can provide experimental evidence for three-dimensional unsteady flows that cannot be validated via wind tunnel experiments; CFD developers (research groups in academia as well as R&D engineers in companies) can use it to validate turbulence models.

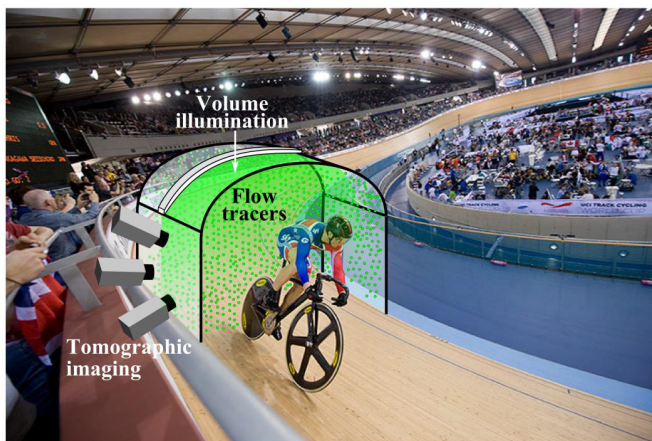


Figure 1.5: Schematic representation of the Ring of Fire concept for on-site aerodynamic measurements as envisaged by Sciacchitano et al. (2015)

As an initial study of the Ring of Fire towards the envisaged use for large-scale industrial applications, Terra et al. (2017) carried out a small-scale version of this proposed technique, measuring the aerodynamic drag of a sphere with a diameter of 0.1 m. The

authors introduced a system based on tomographic-PIV and helium-filled soap bubbles (HFSB).

The next two chapters provide the reader with the necessary background on cycling aerodynamics (Chapter 2) and on the particle image velocimetry (PIV) measurement technique (Chapter 3). After that, the dissertation is divided into two parts. The first part (Chapters 4 and 5) assesses the practical implementation of the RoF towards its use for large-scale applications. To do so, time-resolved stereo-PIV measurements are conducted on a cyclist. The second part of this dissertation (Chapters 6 and 7) implements the findings and conclusions from part 1 and presents two applications in speed sports studied with the RoF. Chapter 6 investigates the effect of drafting in cycling. Chapter 7 demonstrates the applicability of the RoF to speed skating.

2

CYCLING AERODYNAMICS

This chapter reviews and analyses the relevant literature on cycling aerodynamics. First Section 2.1 presents a comprehensive overview of the history of the subject. In Section 2.2, the importance of aerodynamics in cycling is discussed in relation to the cycling power model. The different methods of assessing aerodynamic drag in cycling are discussed and compared in Section 2.3. Sections 2.4 and 2.5 address the literature on the state of knowledge about the aerodynamics of individual and drafting cyclists, respectively.

2.1. HISTORY

Who was the first to invent the bicycle? The answer is a bit trickier than one might imagine. In 1817 the German baron Karl von Drais invented the forerunner of the bicycle, the *Laufmaschine* (running machine), or Dandy horse as it was popularly called (Figure 2.1). This two-wheeled balance bike made from wood, with both wheels in-line, was propelled by the rider pushing along the ground with the feet as in regular walking or running. The front wheel and handlebar assembly were hinged to allow steering. The machine weighed 22 kilograms and on his first ride, the baron was able to cover 13 kilometers in approximately 1 hour.

Von Drais is generally regarded as the father of the bicycle because of this early invention. However, the bicycle as we know it today has emerged in the nineteenth century due to the efforts of many different inventors, who improved upon the early design of von Drais. Several French inventors, among which Pierre Lallement, Pierre Michaux, and Ernest Michaux, built prototypes with pedals attached to the front wheel at the beginning of the 1860s. These were the first machines to be labelled "bicycles," but their bumpy ride earned them the nickname "boneshakers."

After the introduction of these bicycles, cycling races started to be organized everywhere. On May 31, 1868, at the Park of Saint-Cloud in Paris, the first recorded cycling race took place over 1,200 meters. James Moore, an expatriate Englishman who rode a bicycle with sturdy rubber tires, won the race. With the growing popularity of cycling races also came the need for faster bicycles. The pedalling mechanism mentioned above was directly connected to the front wheel (Sharp, 1896), posing one significant limitation: the wheel-to-crank revolution ratio was one and could not be changed. In hopes of adding speed, inventors such as Eugène Meyer and James Starley invented new models with an oversized front wheel, which increased the path length covered per crank revolution. These oddly shaped machines, known as "penny-farthings" or "ordinaries," were very popular in the 1870s and 1880s, and helped to create the first bicycle clubs and competitive races. A picture taken during one of such penny-farthing races is shown in Figure 2.2.



Figure 2.1: *Laufmaschine* (Sharp, 1896)



Figure 2.2: Picture of a penny-farthing race (Andrews, 2021)

Thanks to the increased pace provided by these penny-farthing bikes, one of the most prestigious cycling competitions, the world hour record (WHR), was born. Frank Dodds

in the cyclist's posture on the bicycle. Two of the most striking cycling postures of that time were the 'Obree posture' and the 'superman posture'. The former was thought of by Scottish cyclist Graeme Obree ('the flying Scotsman'). His bicycle set-up allowed him to ride with his head down and hands tucked in underneath his chest. The latter posture positioned the arms stretched out straight in front of the body. This posture was used by Chris Boardman when he set the longest recorded distance to date of 56,375 m in 1996. As a consequence, the UCI prohibited such extreme bike designs in 2000, and the records were split into two categories based on the equipment used: "best human effort" and "world record". As a result, the world-hour record was returned to the one set by Merckx in 1972. The third and final period began in 2014, when the UCI relaxed regulations on the bicycle and equipment to encourage the use of current technology used in endurance track events, resulting in yet another rapid rise in the hour record, now known as the "unified hour record". With a breathtaking distance of 55,089 meters, Victor Campenaerts holds the existing world hour record.

2.2. IMPORTANCE OF AERODYNAMICS IN CYCLING

To understand the importance of aerodynamics in cycling from a quantitative perspective, it is necessary to look at the mechanics and dynamics of the distribution of cycling power, i.e. if a cyclist produces 300 W of power, how much of that power is required to overcome aerodynamic resistance?

Cyclists expend their energy to overcome resistive forces that oppose their forward motion, comprising rolling and gradient resistance, friction forces in drivetrain and bearings components, bump losses and finally the aerodynamic drag. Any unbalance between these forces results in acceleration or deceleration of the cyclist. During acceleration and deceleration, inertial effects play an additional role. A schematic, shown in Figure 2.4, highlights the origin of the drag components encountered during cycling.

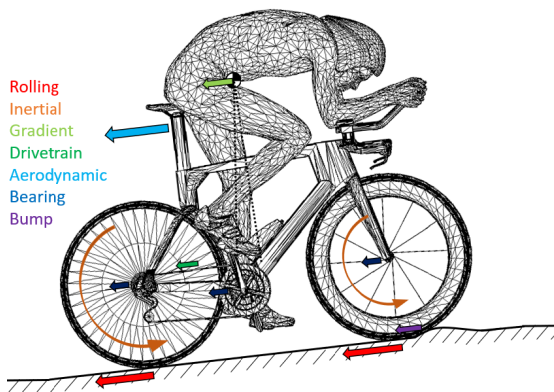


Figure 2.4: Schematic representation of opposing forces during cycling (Hirsch, 2018)

A well established and validated mathematical model for cycling power was given by Martin et al. (1998). Assuming that the cyclist is riding over a surface with minimum undulations and thus bump losses can be neglected, the model provides an expression

for the total resistance experienced by a cyclist ($F_{cyclist}$) in terms of the above mentioned forces.

$$F_{cyclist} = D_{aero} + D_{rolling} + D_{drivetrain} + D_{bearing} + D_{inertial} + D_{gravitational} \quad (2.1)$$

Martin et al. (1998) reported an increasing aerodynamic resistance accounting for 56 % to 96 % of the total resistive force with increasing cycling velocity (7 m/s - 11 m/s). While the aerodynamic resistance increases with the square of velocity, rolling resistance can be considered independent from speed, as stated in Grappe et al. (1997). Empirical expressions for the drivetrain and bearing losses are given in section 5.2 and, according to Wilson et al. (2004), together they account for less than 5 % of the total resistance in racing conditions. Thus, it is evident that aerodynamics plays a major role in improving the performance of cyclists.

The aerodynamic drag is generated by the difference in velocity (U) between the object and air:

$$D_{aero} = 0.5\rho U^2 C_d A \quad (2.2)$$

where ρ is the air density, C_d is the drag coefficient, and A is the frontal area of the cyclist. Instead of considering the latter two separately, the aerodynamic performance of cyclists is generally expressed by the drag area, $C_d A$ [m^2].

2.3. AERODYNAMIC RESEARCH METHODS

2.3.1. WIND TUNNEL

Most experimental research in sport aerodynamics is performed in wind tunnels since it offers a controlled environment that can be adjusted for an extensive range of conditions. Opposite to what happens in reality where the object is moving while the fluid is relatively stationary, in a wind tunnel the object is stationary and the air is blown around it. Typical wind tunnel measurements focus on quantitative measurements of forces and moments using a six-component force balance (e.g. Zdravkovich, 1990), which are known for their very high precision (up to 0.0003% of the full scale load, Tropea et al., 2016). However, these are only 'blind' measurements as they do not give you any information on the flow field around the object. Recent developments in flow measurement techniques such as pressure taps and probes (see Figure 2.5), hot wire anemometry and PIV have made it possible to perform both qualitative and quantitative flow measurements which provide useful information for flow diagnostics and topological analysis.

Despite the good controllability and the high precision of wind tunnel measurements, they often have to deal with uncertainties typically arising from scaling effects, relative-to-ground motion modelling, model blockage, low freestream turbulence levels, and interference of the support (Barlow et al., 1999; Páscoa et al., 2012), which brings the experiment far from real-life conditions. Experiments with scaled-down models typically lead to a Reynolds number an order of magnitude lower than full-scale, such as the water tunnel experiments by Barry et al. (2016b). In this particular case, it was found that the diffusion of flow structures was higher compared to the full-scale results. Full-scale experiments on the other hand, might have to deal with blockage effects affecting the



Figure 2.5: Single rider setup with a pressure wake rake 600mm downstream of athlete. (Barry, 2015)

measured force. The measurements of Zdravkovich (1996) were known to have blockage of up to 15%, requiring corrections on the measured forces. However, it is not clear from the report whether the author had included such corrections. Next, in the absence of a rolling floor a static wind tunnel floor boundary layer can develop, which interacts with the model. Possible ways of mitigating this effect is the use of a short and raised platform or a moving floor arrangement. Wind tunnel facilities are designed to operate at very low freestream turbulence conditions along with high flow uniformity as this is essential for repeatability of results. However, the freestream conditions of on-site sports environments are characterized by gusts, atmospheric turbulence, air currents, etc. which affect flow phenomena such as transition, separation, and reattachment especially for bluff bodies such as cyclists. Therefore, findings from wind tunnel tests may deviate from reality.

2.3.2. COMPUTATIONAL FLUID DYNAMICS (CFD)

Advancements in computational modelling in recent years have made computational fluid dynamics (CFD) increasingly attractive for aerodynamic investigations in sports (Hanna, 2012). Numerical simulations have studied the flow around bicycle components (Godo et al., 2009), individual cyclists (Figure 2.6, Griffith et al., 2014), and groups of cyclists (Blocken et al., 2018). The main benefit of CFD is its ability to obtain the full flow field information necessary to evaluate the aerodynamic forces. In addition, CFD allows for the aerodynamic forces acting on a cyclist to be split into the viscous and pressure force components. Finally, with CFD it is possible to easily vary parameters to perform an optimization of the athletes' position, equipment, etc.

In general, CFD simulations are classified into direct numerical simulations (DNS), large eddy simulations (LES) and Reynolds Averaged Navier-Stokes (RANS) approaches, corresponding to decreasing accuracy and increasing model complexity respectively. Defraeye et al. (2010b) compared the performance of different turbulence-modelling techniques, such as steady RANS, with several $k-\epsilon$ and $k-\omega$ turbulence models, and unsteady LES. They concluded that the $k-\epsilon$ model is most suited to predict the aerodynamic drag of cyclists, with an underestimation of 4% compared to the corresponding

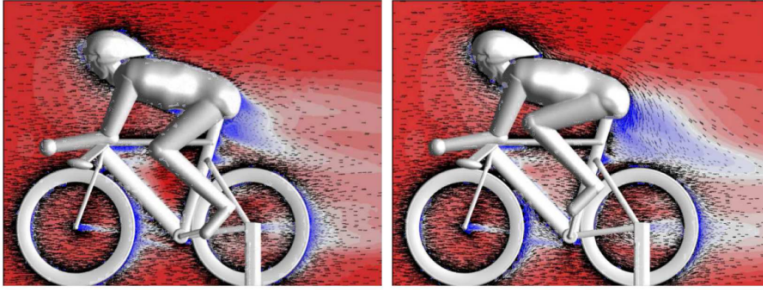


Figure 2.6: Contours of time averaged streamwise velocity taken from transient numerical simulations in a centreline plane of a cyclist; (left) 15° crank angle, (right) 75° crank angle. Colour contours range from $0.3U$ to $1.1U$, with $U=16$ m/s (Griffith et al., 2014).

wind tunnel result.

Even though CFD shows great advantages for aerodynamic investigations in sports, as shown in Gardan et al. (2017), the results should be interpreted with caution. The use of simplifications, such as only taking the rider into consideration and not the bike, modelling smooth surfaces over the entire model, or using a static cyclist model, impact the accuracy of the results. Furthermore, CFD results are sensitive to domain size, initial conditions, mesh resolution, turbulence model, and numerical schemes to name a few, which makes experimental validation of the results essential.

2.3.3. TRACK AND ROAD TESTS

Track testing where cyclists' performance is measured on-site using various techniques such as towing tests (Capelli et al., 1993), coast-down tests (Kyle, 1979; Kyle and Burke, 1984), oxygen consumption (Pugh, 1974) and more recently using power meters (Bassett et al., 1999; Broker et al., 1999; Edwards and Byrnes, 2007; Fitton et al., 2018), offers a possible alternative. The towing method determines the aerodynamic drag of the cyclist by towing the athlete with a strain gauge equipped cable on a flat track at constant speed. A linear regression is applied between force and square of velocity to find the drag force (Capelli et al., 1993; di Prampero et al., 1979). Candau et al. (1999) underlined that the results of this method are highly dependent on the atmospheric conditions as well as on the distance of the cyclist from the back of the vehicle. The coasting-down method is based on Newton's second law ($F = m \cdot a$), where F is the sum of the resistive forces, m is the combined mass of rider and bike, and a is the acceleration. The test can be conducted in descent or on flat terrain and measures, respectively, the cyclist's acceleration or deceleration in free-wheel condition. The cyclist accelerates up to a pre-defined speed, stops pedalling and application of Newton's second law allows to estimate drag area and rolling resistance coefficient through velocity and time measurement. The accuracy of the drag calculation strongly depends on the accuracy of the time and velocity measurements. In recent years, the steady state torque test became the most practiced method in cycling. Power meter measurements are carried out to determine the power output of the cyclist, from which the cyclist's aerodynamic drag is retrieved based on the balance of power Grappe et al. (1997). These tests usually are conducted under very

specific conditions: no wind, constant cycling speed, and flat terrain (Lukes et al., 2012), which generally do not match the real conditions. In the case wind cannot be neglected, a Pitot tube can be mounted upstream of the bike's handlebars Fitzgerald et al. (2019); Kordi et al. (2021). This allows to measure the relative velocity between cyclist and surrounding air and, instead of using the measured ground speed and assuming stagnant air conditions, the actual air speed can be used in the mathematical model, thus avoiding one source of error. One of the latest developments in track testing comes from a company called *SwissSide*. They developed a pressure wake rake that is directly mounted to the bike (Figure 2.7) with the purpose of measuring the losses in the airflow behind the bike and rider.



Figure 2.7: Patrick Lange track test with the *SwissSide* pressure rake at the Salzburgring race track (Dirksen, 2019).

When comparing these on-site techniques with respect to the wind tunnel, the advantages of a better reproducibility of real-life conditions and lower cost is counterbalanced by a large variability of the results, affected by many sources of uncertainty. The latter arise from assumptions in constant drag area or rolling coefficient with velocity, atmospheric variables, chain efficiency, and power measurements inaccuracy due to variations in pace (Crouch et al., 2017). Furthermore, track tests typically do not deliver flow field data to aid interpretation of the results. Nevertheless, for many cyclists track and road testing is the standard method they use for aerodynamic testing due to their simplicity.

2.4. SINGLE-RIDER AERODYNAMICS

2.4.1. CYCLIST POSITION AND GEOMETRY

Recent studies indicate that approximately 80 % of the total aerodynamic drag acting on the bicycle–rider system is caused by the rider (Griffith et al., 2014). Therefore, minimising the aerodynamic drag through rider position is one of the most efficient approaches to improve performance. This was already identified in an early wind tunnel study conducted by Kyle and Burke (1984) who emphasized the importance of the rider posture by a hierarchical approach in evaluating factors contributing to the drag. They found that

rider position is most important, followed by the bike geometry and finally the rolling resistance. One of the first studies on cycling aerodynamics was performed by Nonweiler (1956). He investigated the aerodynamic drag of a cyclist in a racing position, i.e. holding the dropped handlebars, in a closed test section wind tunnel through a sophisticated suspended wiring system allowing for force balance measurements. Later Nonweiler (1958) underlined the dependency of drag to the square of the velocity, highlighting a missing drag crisis Reynolds number range typical of simpler bluff bodies. Furthermore, given the variation in frontal area of the cyclist with changing legs position, the author proposed to focus on the drag area for improving aerodynamic performance. Since then, multiple studies have attempted to summarise the differences among the cyclist postures and their aerodynamic effects. Many of the earlier studies made an effort in reducing the cyclist frontal area in order to lower the drag. As a consequence, in the 70's cyclists started adopting drops position on flat terrain (posture b in Figure 2.8) and a hill descent position in the downhill (posture c in Figure 2.8).

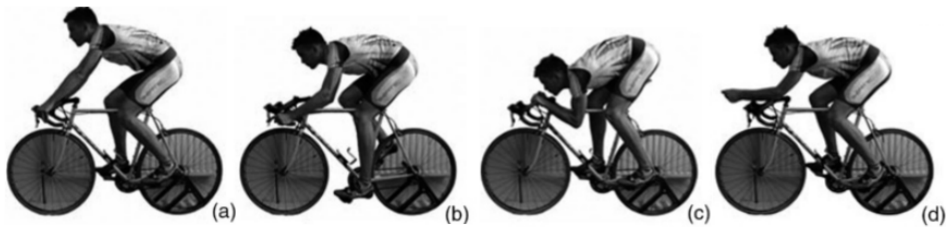


Figure 2.8: The main four positions: traditional upright (a), drops (b), hill-descent (c), time-trial (d), reproduced from Lukes et al. (2005)

In 1989 Greg LeMond won the Tour de France with a difference of only 8 seconds after using tri-bars in the final time-trial. The tri-bars allowed him to have his torso aligned with the ground and assume the time-trial position (posture d in Figure 2.8). Following the victory of Greg LeMond, Kyle (1989) investigated the adoption of tri-bars and found a 15% drag reduction compared to the drops position, which in its turn was reported to have 19% less drag compared to the traditional upright position Kyle and Burke (1984).

Later works confirmed the importance of the posture on the cyclist drag area. Grappe et al. (1997) evaluated the aerodynamic drag of twelve cyclists' in an open velodrome by a linear regression analysis based on steady-state torque tests with a power meter. The drag of the time-trial posture was found 12% lower than the brake hoods one, i.e. the traditional upright position. Another study, performed by Gibertini and Grassi (2008), also investigated the variations between the time trial position and the upright position. They performed force balance measurements in a wind tunnel with two cyclists and concluded that the drag in time-trial position was between 21% and 25% lower than the upright position. Furthermore, the authors also reported that that the upright position with the hands on the stem had 5% more drag than the traditional brake hoods one, despite the reduction in frontal area. Defraeye et al. (2010a) conducted a similar test and found the time-trial position to have 20% less drag area than the upright stem position. The authors attempted to separate the drag contribution of the cyclist from the bike by

subtracting the drag of the bike setup. The results showed that the drag of the cyclist accounts for 70% of the total drag. In comparison to the previously discussed studies, Barry et al. (2015a) performed wind tunnel balance measurements on a pedalling cyclist. The authors tested nine different positions and distinguished the contribution of the frontal area from the drag coefficient on the drag area. They underlined that small changes in posture, such as lowering the head or closing the elbows in time-trial position, can have a significant effect on the aerodynamic drag. In addition, they found that the major contribution in drag area for the upright brake hoods position was attributed to the cyclist frontal area, as the drag coefficient was lower than the time-trial one. Furthermore, wake surveys with dynamic pressure probes brought to the surface that the maximum variations in drag coefficient of around 7% among the nine postures is connected to the spatial distribution of streamwise velocity deficit in the cyclist wake as well as different velocity levels. The results of a small selection of studies investigating cycling position are summarized in table 2.1.

2.4.2. CYCLIST FLOW TOPOLOGY

Even though there has been an extensive amount of research into cycling aerodynamics, little work has investigated the flow field around a cyclist. Recently Crouch et al. (2012) conducted an in-depth study to characterise the flow structures around a cyclist and relate them to the aerodynamic forces. The authors conducted force measurements in a wind tunnel on an anthropomorphic cycling mannequin with the legs at different positions around the crank cycle. This revealed that the drag of a cyclist varies cyclic over half of the crank period. A minimum was measured when the cranks were close to horizontal (the upper legs were level) and a maximum was measured for the case of one leg at its highest point and the other extended (see Figure 2.9b). The crank angle (φ) was defined as the angle between the crank and the horizontal in anti-clockwise direction with the left crank rearward as the zero point (see Figure 2.9a).

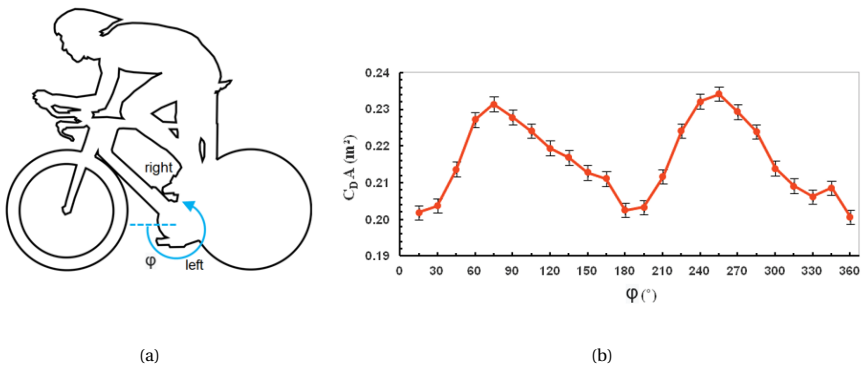


Figure 2.9: (a) Illustration of the definition of the crank angle (b) Variation of drag area with crank angle (φ) (Crouch et al., 2012)

Simultaneously acquired projected frontal area measurements brought to light that

Table 2.1.: Summary of some references' drag coefficients and drag areas for time-trial, dropped, and upright postures

Study	Time-trial posture		Dropped posture		Upright posture		Crank condition	Measurement system
	C_d	$C_d A [m^2]$	C_d	$C_d A [m^2]$	C_d	$C_d A [m^2]$		
Kawamura (1953)	-	-	-	-	1.03	-	Static	Wind tunnel - Force balance
Nonweiler (1956)	-	-	0.93	-	-	-	Static	Wind tunnel - Force balance
Davies (1980)	-	-	-	0.280	-	-	Dynamic	Wind tunnel - Oxygen consumption
Kyle and Burke (1984)	-	-	-	0.260	-	0.320	Static	Wind tunnel - Force balance
Capelli et al. (1993)	0.652	0.256	-	-	-	-	Dynamic	On-site - Towing method
Zdravkovich (1996)	0.545	-	0.605	-	0.675	-	Static	Wind tunnel - Force balance
Grappe et al. (1997)	-	0.262	-	-	-	0.299	Dynamic	On-site - Power meter linear regression
Martin et al. (1998)	-	0.269	-	-	-	-	Dynamic	Wind tunnel - Force balance
Candau et al. (1999)	-	0.262	-	-	-	-	Dynamic	On-site - deceleration method
Padilla et al. (2000)	-	-	-	-	0.650	0.244	Static	Wind tunnel - Force balance
Jeukendrup and Martin (2001)	-	0.240	-	0.307	-	0.358	Static	Wind tunnel - Force balance
Gilbertini and Grassi (2008)	0.792	0.235	0.814	0.282	0.760	0.304	Dynamic	Wind tunnel - Force balance
García-López et al. (2008)	0.975	0.317	-	-	1.33	0.475	Dynamic	Wind tunnel - Force balance
García-López et al. (2008)	-	0.260	-	-	-	-	Static	Wind tunnel - Force balance
Defraeye et al. (2010a)	-	0.211	-	0.243	-	0.270	Static	Wind tunnel - Force balance
Defraeye et al. (2010a)	-	0.150	-	0.179	-	0.219	Static	Computational Fluid Dynamics
Underwood et al. (2011)	0.825	0.261	-	-	-	-	-	Wind tunnel - Force balance
Chowdhury and Alam (2012)	0.860	0.327	-	-	1.04	0.427	Static	Wind tunnel - Force balance
Crouch et al. (2014)	0.520	0.216	-	-	-	-	Static	Wind tunnel - Force balance
Barry et al. (2015a)	0.734	0.283	0.703	0.332	0.739	0.343	Dynamic	Wind tunnel - Force balance
Terra et al. (2016)	-	0.243	-	-	-	-	Static	Wind tunnel - Force balance
Terra et al. (2016)	-	0.244	-	-	-	-	Static	Wind tunnel - control volume (Tomo-PIV)
Crouch et al. (2017)	-	0.240	-	-	-	-	Static	Wind tunnel - Force balance
Crouch et al. (2017)	-	0.242	-	-	-	-	Dynamic	Wind tunnel - Force balance
Crouch et al. (2017)	-	0.236	-	-	-	-	Dynamic	Wind tunnel - control volume (p_{rot} probes)

the variation in the drag area is primarily attributed to the variation in drag coefficient. In addition to wind tunnel balance measurements, smoke visualisations revealed the existence of a symmetric separation from the hips for $\varphi = 15^\circ$, while an asymmetric separation occurred at $\varphi = 75^\circ$, with the flow strongly curving downwards in correspondence of the hip of the bent leg.

Subsequently, Crouch et al. (2014) conducted wake surveys downstream of a full-scale static cyclist mannequin at a range of leg positions around the crank cycle to investigate the effect of leg geometry on the flow around the cyclist. The measurements were performed by a four-hole dynamic pressure probe in a plane of $0.75 \text{ m} \times 1 \text{ m}$ located 0.7 m above the ground. In addition, pressure taps on the mannequin's back, and oil and paint flow visualization were used to gain further insight into the flow over the cyclist's torso.

Based on this work Crouch et al. (2014) proposed a detailed characterization of the flow field around a cyclist at the two key flow regimes. The first was the symmetric low-drag regime, which occurs at a crank angle of $\varphi = 15^\circ$. The flow separates identically from both hips and wraps around from under both legs forming an additional vortex pair of the same rotation to the upper hip vortex, as can be seen in Figure 2.10a. Notice that only the right part of the wake topology is shown in this figure, as the left part is the mirrored version. The second was the asymmetric high-drag regime, which was observed when at a crank angle of $\varphi = 75^\circ$. In this position one hip closes and blocks the flow from under the torso, which reduces the separation over that hip, making it impossible for the flow to wrap around onto the rear of the cyclist. On the other side instead, where the hip opens further, the flow separates earlier and higher. This asymmetric profile generates a strong vortex pair in the wake, in addition to smaller secondary structures. These two regimes are depicted in Figure 2.10.

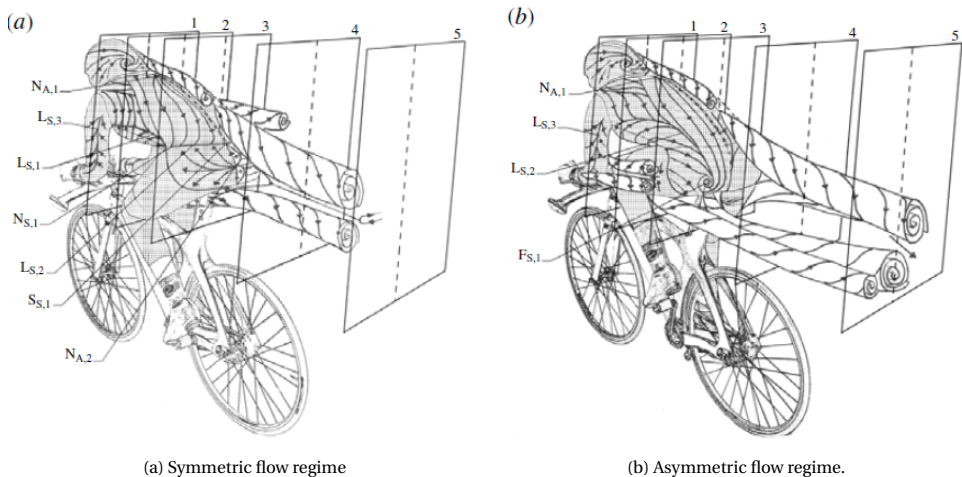


Figure 2.10: Cyclist wake flow topology, adapted from Crouch et al. (2014).

Griffith et al. (2014) carried out steady state and transient numerical simulations on the same case that was studied experimentally by Crouch et al. (2014). A simplified cy-

clist model was constructed to replicate the geometry of the used mannequin and the leg position was varied around the crank angle to assess the influence of leg geometry on the drag as well as on the flow structures. The authors reported a qualitative agreement with the results found by Crouch et al. (2014), confirming the variation of drag with crank angle. The CFD results under predicted the experimental results by 15%, which was attributed to simplification of the CFD geometry. The associated wake structures for the two primary flow regimes are shown in Figure 2.11, where they are compared with the experimental results of Crouch et al. (2014). The planes of the streamwise vorticity show that the time average transient solution is able to predict the flow structures observed around a cyclist. The steady state solution on the other hand produces reasonable agreement in the asymmetric regime at 75° , but at a crank angle of 15° the flow field does not exhibit the symmetric profile seen in the experimental results and the time averaged transient flow.

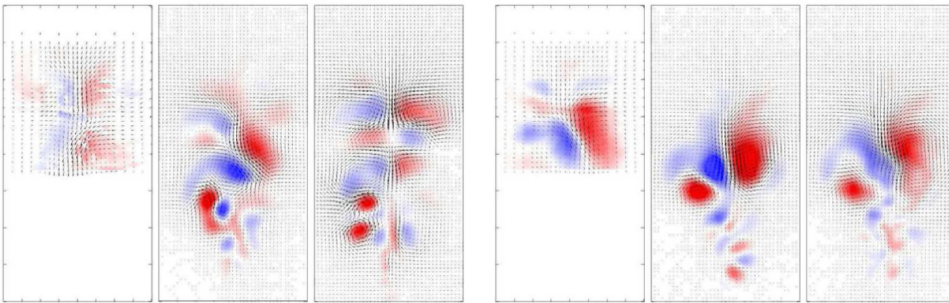


Figure 2.11: Contours of streamwise vorticity with vectors of cross stream velocity for a cyclist at (left series) 15° crank angle and (right series) 75° crank angle corresponding to the symmetric and asymmetric regimes in experimental results. In each set of three images results are shown for (left) experimental, (middle) numerical steady state solution, and (right) numerical transient average. Planes taken at 0.6 m downstream of the model. Contours vary across the range $-100s^{-1} \leq \omega_x \leq 100s^{-1}$, from blue (negative) to white (zero) to red (positive) (Griffith et al., 2014).

To continue the research of Crouch et al. (2014) and Griffith et al. (2014), Crouch et al. (2016) expanded the dimensions of the measurement plane in vertical direction to capture the entire wake field behind the cyclist and mapped the flow topology for a range of reduced pedalling frequencies¹. Wake flow fields for both static leg and pedalling cyclists were compared over the full 360° rotation of the crank using both time- and phase-averaging. From this study, the authors concluded that the differences in wake topology between a static pedal position and its phase-averaged dynamic pedalling counterpart are marginal, regardless of the pedalling frequency. This typical cyclist streamwise vortex topology was also observed by Terra et al. (2019), illustrating the robustness of this flow features. The authors applied large-scale tomographic PIV to capture the full wake of a static cyclist mannequin with asymmetric leg position. Furthermore, they used the PIV data to apply the integral momentum conservation in a control volume to obtain drag.

¹The reduced frequency is a dimensionless parameter expressing the weight of unsteady phenomena with respect to steady phenomena. For the cyclist, it is a ratio of the leg speed around the crank and the freestream flow $k = 2\pi r f / U_\infty$, with f the pedalling cadence, and r the crank length.

Planar measurements in the wake, however, might fail at capturing the full complexity of the structures characterising the cyclist flow topology. Jux et al. (2018) conducted robotic volumetric PIV measurements around a full-scale static cyclist mannequin. Their measurements contained a 2 m^3 domain and yielded quantitative flow visualisations in terms of velocity, streamlines and vorticity, advancing the understanding of the main sources of drag and the complex aerodynamic interactions from different segments of the body (Figure 2.12).

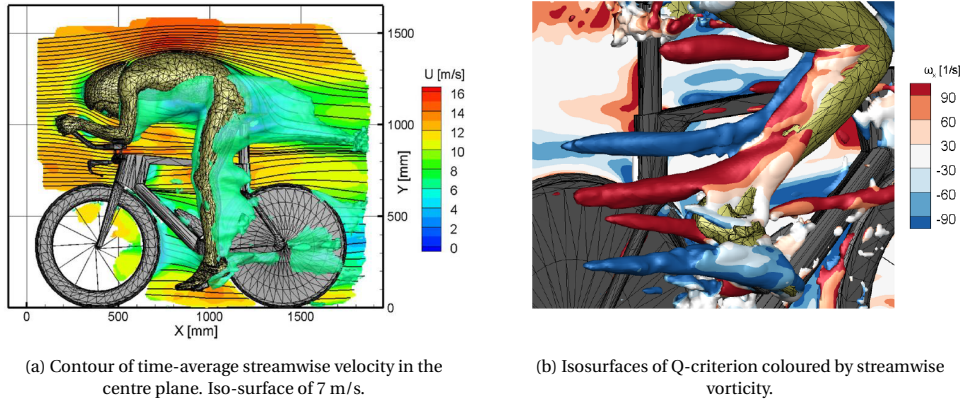


Figure 2.12: Robotic coaxial volumetric velocimetry results Jux et al. (2018).

Considering that a cyclist can be described as an aerodynamic bluff body (Gibertini and Grassi, 2008), the overall aerodynamic drag of the cyclist is dominated by the pressure drag. Therefore, the pressure distribution on and around the cyclist can provide valuable information about the distribution of the aerodynamic drag along the rider's body and the bike. Despite this, there are little studies in cycling aerodynamics that report the pressure distribution. The most convenient way to study the pressure distribution is to use CFD simulations, as was presented by Blocken et al. (2013) (Figure 2.13) and Beaumont et al. (2018), among others. Experimentally, the surface pressure was measured on a real cyclist and on a mannequin by Defraeye et al. (2010a) and Crouch et al. (2014), respectively, by conventional wall orifices. More recently, Jux et al. (2020), based on robotic volumetric PTV measurements followed by the integration of the pressure gradient, were able to obtain the surface pressure distribution around a full-scale cyclist mannequin (Figure 2.14). The distributions of the pressure coefficient across a rider in time-trial position, obtained by Blocken et al. (2013) and Jux et al. (2020), shown in Figures 2.13 and 2.14, highlight an area of high pressure, induced upstream of the rider, and large regions of low pressure over the back, to the left and right of the upper body and downstream of the legs.

2.5. MULTI-RIDER AERODYNAMICS AND DRAFTING

Aerodynamic research in cycling has, to date, primarily focussed on a single rider because it has been seen that time trial events are where the greatest gains can be achieved from aerodynamics. These events are conducted at maximum sustainable power, mean-

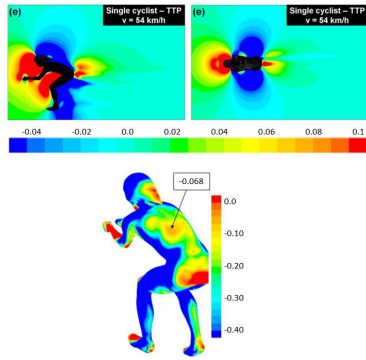


Figure 2.13: Pressure coefficient on the surface of a rider (top) and in the flow across it (bottom) Blocken et al. (2013)

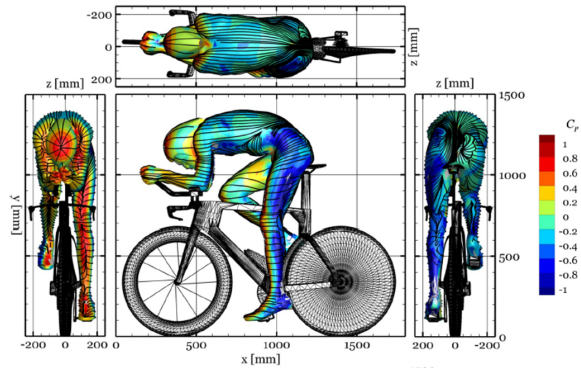


Figure 2.14: Surface pressure coefficient distribution on a full-scale cyclist model by robotic volumetric PTV Jux et al. (2020).

ing any reduction in drag directly translates to greater speed. However, for the majority of cycling events the cyclists' performance is strongly influenced by rider interactions or in other words drafting. In cycling jargon, drafting is a riding technique whereby a cyclist closely follows the preceding athlete, thereby substantially reducing the aerodynamic drag (Barry et al., 2015b; Blocken et al., 2018; Broker et al., 1999). The benefits of drafting have long been understood in cycling. However, the mechanism of this drag reduction as well as its dependence on distance was not very well established, with considerable variation in drag reduction between different studies. Recent developments in the fields of computing resources and experimental methods have helped gain new insight into its behaviour.

2.5.1. EFFECT OF DISTANCE

Kawamura (1953) and Kyle (1979) were among the first to study the effect of drafting distance on aerodynamic drag. While the former conducted wind tunnel measurements of two 1/4 scaled cyclist models in racing position to quantify the drag benefits associated with drafting, the latter performed a coast-down test in a 200 m long enclosed track. The campaign included measurements with 1-4 cyclists, estimating their aerodynamic drag by the rate of deceleration. The results of these early studies differ significantly; the wind tunnel experiments conducted by Kawamura (1953) resulted in a maximum drag reduction of 54% at minimum drafting distance, while Kyle (1979) reported a drag reduction of only 38% at the same drafting distance. These differences might be explained by differences in experimental set up and procedures. Scaling effects and wind tunnel boundary layer effects are cited as possible sources of error for the former, and the latter mentions the difficulty in maintaining constant longitudinal and lateral distance between the cyclists. In addition, the coast-down tests are also very depended on wind variation, which was not recorded by the author.

Later, Zdravkovich (1996) carried out wind tunnel tests with full-scale cyclists in upright posture. The tests covered 20 different drafting positions, not only changing the longitudinal distance between the cyclists but also the lateral. The results showed a max-

imum drag reduction of the trailing cyclist of 49%, at 0.1 m longitudinal separation and at non-staggered configuration. A linear decrease of the aerodynamic benefit is observed when the gap is increased. The maximum separation distance in this test was 0.9 m, where the drag reduction amounted to 15%, which is lower than those reported by other studies. Furthermore, it can be concluded that the drag reduction is rapidly lost by a lateral offset. For instance, a 20% drag increase with respect to the in-line configuration was observed already at an offset of 0.1 m. The gradient of drag reduction with increasing longitudinal distance in the study of Zdravkovich (1996) is significantly higher than found in other studies. Although wind tunnel tests are known for their high accuracy and precision, the experiments of Zdravkovich (1996) were conducted with a blockage ratio of 15%. It is not clear whether the authors applied any corrections to the results for these effects. In addition to the high blockage, the measurements were taken with two cyclists whose isolated drag values differed by 30%. As a result, the gradient of drag reduction with distance was changing depending on the leading cyclist, indicating the dependence on drag reduction on cyclist size as well as distance.

More recently, Barry et al. (2014) carried out wind tunnel experiments on an athlete and a full-scale mannequin in time-trial position at a test velocity of 65 km/h, simulating race conditions of a team pursuit in a velodrome. A maximum drag reduction of 49% for the trailing rider was reported, supporting the findings of Zdravkovich (1996). At a separation of 0.7 m, 40% less drag was measured. Compared to Zdravkovich (1996), the decay rate for this aerodynamic benefit was 3 times smaller, leading to a large discrepancy of approximately a factor 2 with respect to Zdravkovich (1996) results, suggesting that also at gaps larger than 1 m a drafting effect could be experienced. Whether such difference is to be ascribed to differences in posture or experimental artefacts remains not understood. Furthermore, Barry et al. (2014) confirmed that a lateral offset of the trailing cyclist goes rapidly to the detriment of the drag reduction (Figure 2.15). The authors of Barry et al. (2014) also report that the size of the leading and trailing cyclist was not the same, with the trailing cyclist being smaller in size compared to the leading. Thus, the drag reduction quoted in the study might not apply when the positions are reversed.

Blocken et al. (2013) were the first to conduct numerical simulations of the tandem interactions for different cyclist postures. The simulations considered longitudinal separations up to 1 m, and no lateral offset. At the closest position, the numerical calculations returned the largest drag reduction for the trailing rider when both cyclists are in the upright position (27% drag reduction with respect to the isolated configuration). Instead, a drag reduction of only 14% was obtained in the time-trial position. Similarly to previously discussed works, the drag benefits showed a linear decay with increasing drafting distances, for all riders' postures. The discrepancy in drag reduction with respect to the previous discussed experimental investigations may be ascribed to simplifications made in order to reduce the computational cost of the numerical simulations: the CFD model did not include the bicycles but only the riders. In particular, at 1 m separation, a drag benefit of only 12% in time trial position was reported, considerably lower than the value of 46% reported by Kawamura (1953). Later, Blocken et al. (2018) repeated the numerical simulations on a cyclist CFD model that included the bicycle. The reported results are closer to the ones found experimentally; however, they still under-predicted the drag reduction for all longitudinal distances with a maximum drag reduction of 36% at mini-

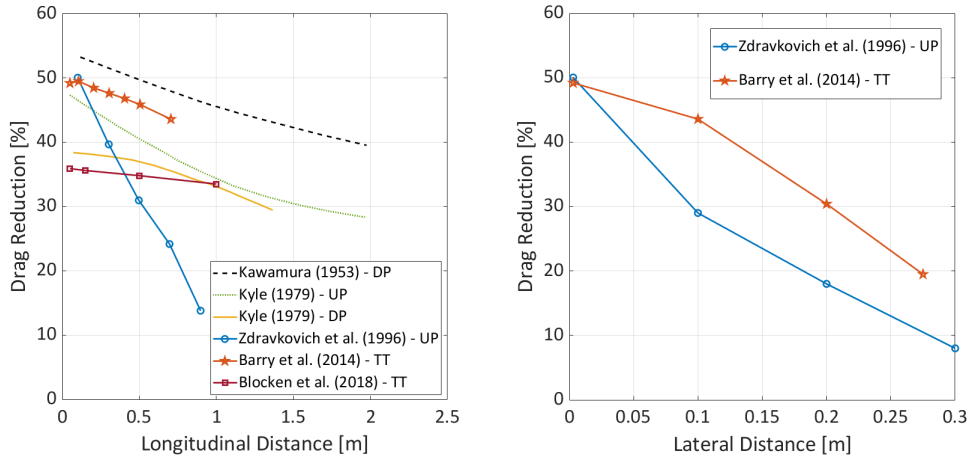


Figure 2.15: Overview of variations of trailing cyclist drag reduction by longitudinal and lateral offset. Data covers different cycling postures: Time trial (TT), upright (UP) and dropped (DP). (Note: Effect of longitudinal distance taken at zero lateral offset. Effect of lateral distance taken at 0.1 m longitudinal separation).

imum spacing. It can be seen in Figure 2.15 that the decay of drag reduction with distance is very low compared to other studies.

The salient aspects from a selection of the above studies are summarized in Figure 2.15, which indicates a drag reduction inversely proportional to both longitudinal separation and lateral offset. However, a striking dispersion of the drag values as well as its decay rate, especially with longitudinal separation, is remarked.

2.5.2. EFFECT OF CYCLIST SIZE, POSTURE AND POSITION

In the study of Barry et al. (2014) there was a size differential between the athlete and full-scale mannequin (see Figure 2.16a), which was reported to affect the drag reduction from drafting. A larger drag reduction was measured with the athlete, who was larger in size, in front. Vice versa, putting the mannequin in front resulted in slightly lower drag reductions. That the drag reduction is also dependent on the physical appearance of both cyclists besides the drafting distance was already hypothesized by Edwards and Byrnes (2007). The authors investigated this by studying the influence of aerodynamic and anthropometric characteristics of both leading and trailing cyclist on the drafting effect. The test subjects were asked to ride an outdoor 200 m flat segment from both directions at a constant velocity of 45 km/h and maintain the same posture. The investigated longitudinal inter-wheel distance was 0.5 m with no lateral offset. The power output of the athletes was measured by a hub-based power meter, which was utilized to extract the aerodynamic resistance from each test. Based on individual cyclist measurements, three cyclists were identified as maximum, median and minimum based on their respective drag areas (i.e. $C_d A$). These cyclists were chosen as leaders for various two cyclist drafting configurations.

The results indicated that the drag reduction for the trailing cyclist is directly correlated with the drag area of the leading cyclist, i.e. the larger the leading cyclist's drag

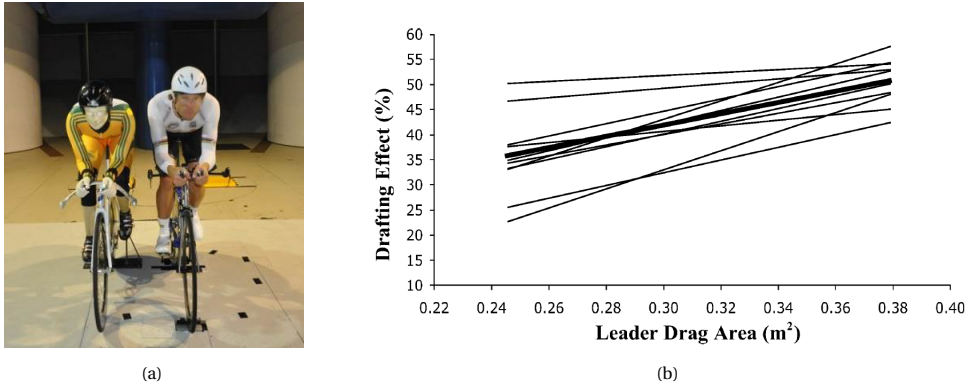


Figure 2.16: (a) Size difference between athlete and full-scale mannequin (Barry et al., 2014) (b) Variation of drag reduction with drag area of leading cyclist (Edwards and Byrnes, 2007).

area, the larger the drafting effect (Figure 2.16b). On average the trailing cyclist felt a drag reduction of 51%, 41% and 35% for the maximum, median and minimum leading cyclist respectively. However, for the same leading cyclist, there were large variations in drag reduction for the different trailing cyclists. From the inconsistencies between the regression slopes in Figure 2.16b it was concluded that although the leader drag area played an important role, it was not the only factor affecting drag reduction. During the experiment, ambient wind direction and speed were measured for each test, however, it is out of the question that the some of the variations in the results were affected by local wind behaviour. Additionally, it can be argued that the drafting distance of 0.5 m was not kept constant throughout the test and thus that some variations could also be ascribed to drafting skill, i.e. the ability of the cyclists to maintain a constant drafting distance and alignment with the leader.

Tandem interactions and the effect of the posture adopted by the cyclists on drag reduction were also modelled computationally by Blocken et al. (2013). The authors performed 3D steady RANS simulations of two cyclists drafting with 3D laser scanned models that were imported into the solver. The models represented the dropped, the upright, and the time trial posture and included only the cyclist body. The bicycle was not included in the model in order to reduce computational costs.

For the upright, dropped and time trial posture the study reported a maximum drag saving of 27%, 23% and 14%, respectively (Figure 2.17). It could thus be concluded that the amount of drag reduction not only depends on size of the cyclists, but also on their posture.

Subsequently, Defraeye et al. (2014) conducted a numerical study on the effect of cyclist size and posture on the drafting effect. The study involved four cyclists in a pace-line with the size and posture of each cyclist different from each other (Figure 2.18). In this context, posture refers to the variations in the way a cyclist adopts the time trial posture, i.e. head raised, head lowered, arms spacing, etc. Four drafting configurations were tested with the position of each cyclist in the pace line being rotated. In addition, the study also investigated the effect of geometry by evaluating athletes in each config-

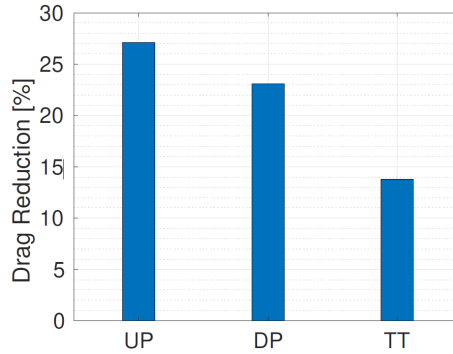


Figure 2.17: Dependence of drag reduction on cyclist position (Blocken et al., 2013).

uration with arm width set at two positions. Similar to Blocken et al. (2013), the bicycle was not included in the model in order to reduce complexity. The CFD simulation used a steady RANS approach, while the drafting gap was assumed to be quasi-zero and the velocity was set to 60 km/h.

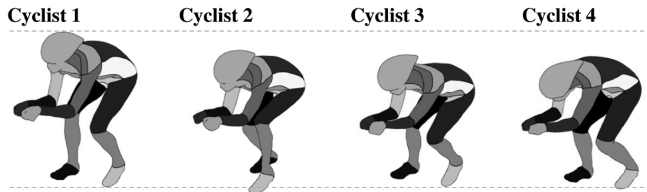


Figure 2.18: The four different CAD models of cyclists used by Defraeye et al. (2014).

The results indicated that the highest drag reduction was obtained in the configuration where the cyclists were ordered from large to small. In addition, in all configurations, a significant reduction in drag area is observed for the cyclist trailing the largest one. The sum of drag areas of all cyclists was found to vary by small margins for different sequences. The lowest overall drag corresponded to the sequence where the largest cyclist was leading the pace-line and vice versa, when the largest cyclist was positioned at the back of the pace-line, the highest overall drag was reported. Finally, the wider arm spacing led to an increased drag for all 4 sequences, although there were significant differences in the magnitude for each sequence.

A similar study was performed experimentally by Barry et al. (2015b). The authors measured aerodynamic drag on four in-line, pedalling athletes simultaneously to investigate the influence of rider posture and ordering throughout the pace-line on the aerodynamic drag. During the experiments, each rider cycled through positions 1–4 in the pace-line and took one of the four postures pictured in Figure 2.19, while the remaining athletes stayed in their baseline posture.

The study concluded that postures that reduce the resistance of a single cyclist have a higher degree of reduction in the team, while postures that increase the resistance of



Figure 2.19: Riding postures adopted by athletes: baseline, head raised, head lowered, elbows together (Barry et al., 2015b).

a single cyclist have a smaller reduction in resistance in the team. The study showed that changing the cyclist's posture in the pace-line does affect the resistance of other cyclists. However, the conclusions of previous studies were not completely confirmed. For example, increasing the drag area of the leading rider caused both increases as well as decreases in drag reduction of the trailing rider. The authors point out that these differences are caused by the subtle differences between the body and shape of each cyclist and the interaction between these differences.

In addition to the frontal area and posture, Fitton et al. (2018) also evaluated the correlation between cyclists' mass and their drag savings when riding at different positions in a team pursuit. To this end, a mathematical model was created, which uses power meter data and the geometry of the velodrome as input data. Four professional female athletes rode once individually and once in close proximity to each other, at a speed of 50 km/h. The results assigned the largest drag benefits to the athletes in position 3 and 4. It was concluded that the drag reduction experienced by a trailing cyclist is highly correlated with the difference in mass between the leading and trailing cyclist. However, this correlation was only strong for the second cyclist in the pace-line and less so for the other cyclists.

From the above discussion, it is clear that a number of studies have shown the dependence of drag reduction on the size of the cyclists involved, positions adopted by the cyclists and the variations in posture. Factors like bigger cyclist size, wide arm spacing, raised head, etc. that increased the drag area of the leading cyclist resulted in higher drag reductions for the trailing cyclist. Conversely, factors that increased the drag of the trailing cyclist resulted in lower drag reductions. Although this hypothesis was not observed universally, it can be argued that imperfect alignment, cyclist drafting skill and the presence of more than two cyclists could have influenced these measurements.

2.5.3. DRAG REDUCTION OF LEADING CYCLIST

It has been suggested by Olds (1998) that riding close behind a leading cyclist will also benefit the leading rider in that the low-pressure area behind the cyclist will be 'filled up' by the trailing rider. Nevertheless, nor Kyle (1979), nor Zdravkovich (1996) were able to find any quantifiable effect on the aerodynamic drag of the lead cyclist. More recent wind tunnel experiments by Barry et al. (2014) did find a maximum drag reduction for the leading cyclist of 5 % at minimum spacing between the cyclists. Similar findings are reported by other studies by Defraeye et al. (2014), Barry et al. (2015b), Belloli et al. (2016), Fitton et al. (2018) and Blocken et al. (2018). Numerical studies by Íñiguez De-

La Torre and Íñiguez (2009), Blocken et al. (2011), and Blocken et al. (2013) also confirmed that there is indeed a benefit for the leading cyclist using CFD simulations. The drag reduction on average was found to be $\leq 5\%$, which is very low compared to the drag reduction for the trailing cyclist.

2.5.4. FLOW TOPOLOGY

One of the first studies investigating the flow field around drafting cyclists was performed by Blocken et al. (2013). The study provided a detailed analysis of the pressure fields around two cyclists in tandem configuration obtained from CFD simulations. The pressure fields, shown in Figures 2.20a and 2.20b, indicate that the low pressure region in the wake of the leading cyclist while drafting was smaller compared to the individual case, which was caused by the upstream propagation of the high pressure region in front of the trailing cyclist. Furthermore, the high pressure in front of the trailing cyclist was reduced and the low pressure region in the wake of the trailing cyclist was alleviated. This effectively reduced the deficit in pressure across the trailing cyclist which was essential for drag reduction.

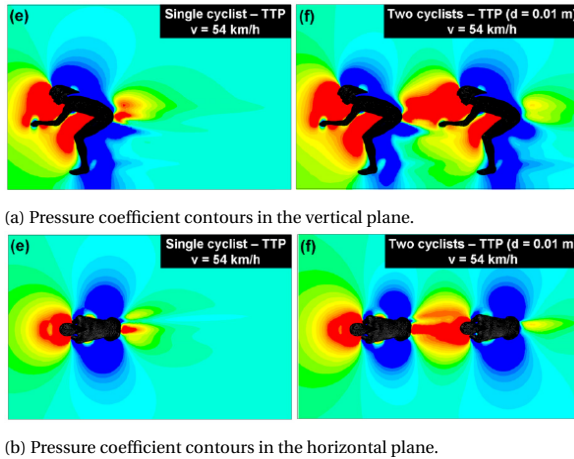


Figure 2.20: Comparison of pressure coefficient contours between individual and drafting cases by Blocken et al. (2013). Colour contours ranging from -0.05 to 0.10.

Barry et al. (2016a) studied the flow field around a trailing cyclist for scaled static cyclist models in a water tunnel for a Reynolds number one order of magnitude lower than full-scale (Figure 2.21). The flow field around the cyclist was captured with a planar PIV setup to acquire time-averaged data. The selected measurement planes are depicted in Figure 2.22.

The measurements were performed at two separation distances, a minimum separation and a higher separation, more precisely $1/11$ of a bike length and one full bike length separation. The vorticity fields in the wake of the individual cyclist and in the wake of the trailing cyclist at both separation distances are presented in Figure 2.23, showing the leading and trailing cyclist both in asymmetric leg position.

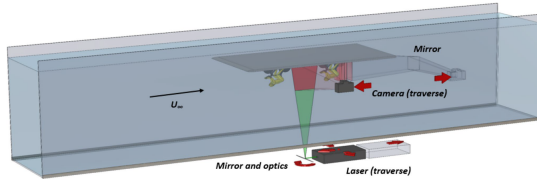


Figure 2.21: Water tunnel setup by Barry et al. (2016a) using a single PIV measurement plane.

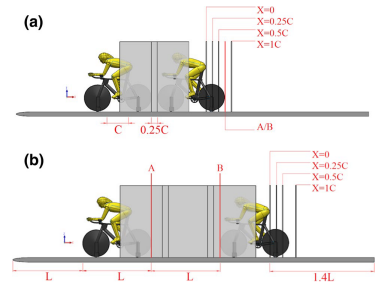


Figure 2.22: Profile view of set-up at the two tandem positions: Spacing 1 (top) and Spacing 2 (bottom). (Barry et al., 2016a)

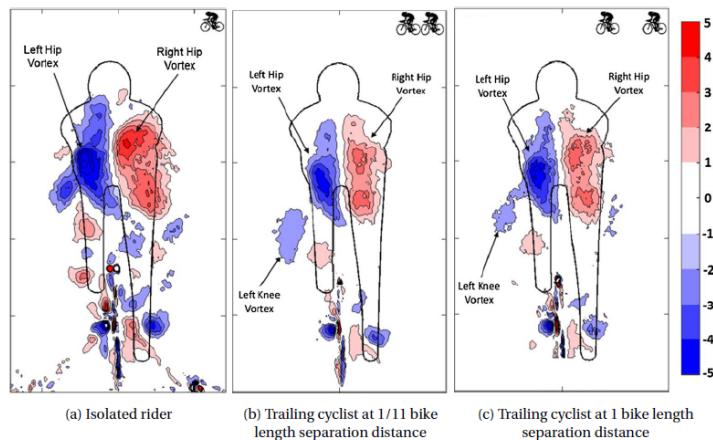


Figure 2.23: Streamwise vorticity behind rider in asymmetric position (Barry et al., 2016a).

The authors observed that the dominant wake structures originating from the trailing cyclist are practically identical to those from an isolated rider, notwithstanding the significant upstream disturbance. For the minimum drafting distance, the vortices were displaced downward and away from the centre due to changes in local in-plane velocity components. At higher separation between the cyclists, the wake more closely resembled the wake of an individual cyclist as two pair of counter-rotating vortices near the hips and lower back were observed at approximately the same locations. It should also be added that the strength of the upper hip vortex structures is marginally weakened, clarified by the authors due to the reduced energy in the flow faced by the trailing rider. Additionally, this study confirmed the findings of Blocken et al. (2013) that the majority of the drag benefit for the trailing cyclist originates from decreased stagnation pressure due to the presence of the leading cyclist. Barry et al. (2016a) compared the streamwise velocity contours just upstream of the trailing cyclist. A clear difference in velocity deficit was identified between the small separation distance and the large one, as depicted in

Figure 2.24.

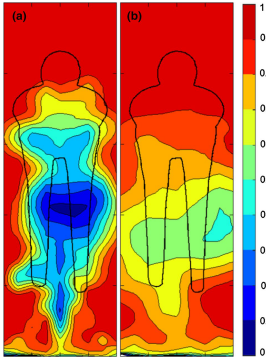


Figure 2.24: Streamwise velocity upstream of trailing cyclist at gap of $1/11$ (left) and 1 (right) bike length (Barry et al., 2016a).

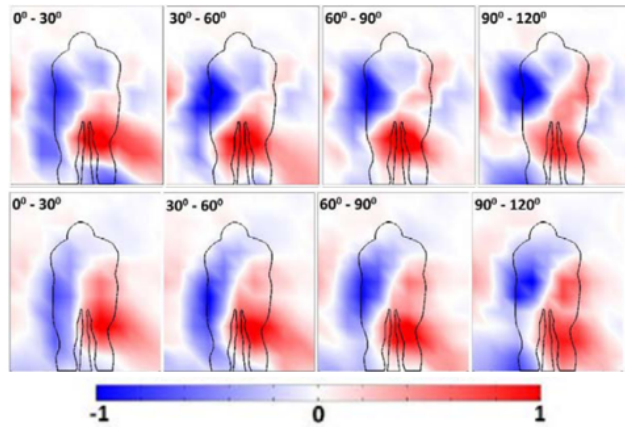


Figure 2.25: Phase-averaged streamwise vorticity plots by Barry et al. (2016b). Upper row isolated rider, lower row trailing cyclist.

In a follow-up study, Barry et al. (2016b) conducted a full-scale wind tunnel experiment with the objective to compare the wake topologies between isolated and trailing cyclist. The measurements were performed with pressure probes in the wake of a mannequin and athlete in a dynamic pedalling configuration covering a field of view of $0.8 \text{ m} \times 1 \text{ m}$. Similar to Barry et al. (2016a), the main vortical structures, in particular, the hip vortices are consistent between the isolated and trailing case, although the streamwise vorticity is weakened in magnitude.

The phase-averaged streamwise vorticity plots, shown in Figure 2.25, compare the wake structures of an isolated rider to those of a trailing cyclist in tandem configuration with a separation distance of approximately 0.2 m . The authors concluded that the drag savings of the trailing cyclist are not caused by a change in the wake flow structures. Finally, the authors also looked at the normalized streamwise velocity plots just downstream of the isolated and trailing cyclist, which are given in Figure 2.26a and 2.26b, respectively.

Similar to the primary flow structures, the velocity deficit contour in the near wake region behind a trailing cyclist resembles the individual rider case, albeit the peak velocity deficit and width of the lower wake are slightly more pronounced in the drafting case.

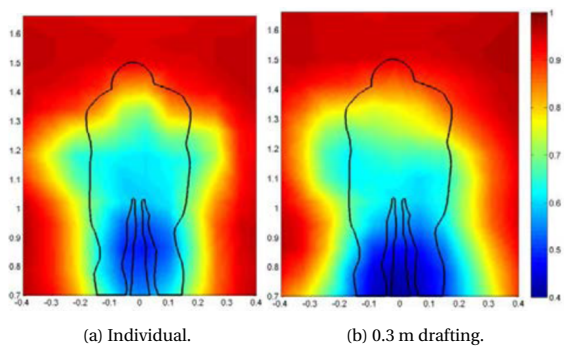


Figure 2.26: Time-averaged normalized streamwise velocity behind cyclist Barry et al. (2016b).

3

PARTICLE IMAGE VELOCIMETRY

The Ring of Fire enables flow visualization and the aerodynamic drag estimation of cyclists by relying upon the use of Particle Image Velocimetry (PIV). This chapter introduces the working principles of PIV (Section 3.1), a non-intrusive flow measurement technique that allows measuring complex flows. Considering the size of the PIV measurement domain has to match the size of the cyclist wake and that the drag force is obtained by applying momentum conservation through the streamwise direction, this chapter puts particular emphasis on the large-scale (Section 3.3), stereoscopic-PIV technique (Section 3.2). Afterwards, Section 3.4 addresses loads determination from PIV and Section 3.5 focusses on application of PIV in cycling. Finally, the concept of the Ring of Fire measurement system is introduced in Section 3.6.

3.1. WORKING PRINCIPLE

Particle image velocimetry is a non-intrusive method for the measurement of the velocity vector field in a plane or in 3D. The technique relies on capturing the motion of tracer particles, entrained by the fluid flow (Adrian and Westerweel, 2011; Raffel et al., 2018). For purpose of introduction, in this section the working principles of a planar PIV system is presented. Figure 3.1 illustrates a typical PIV setup and process.

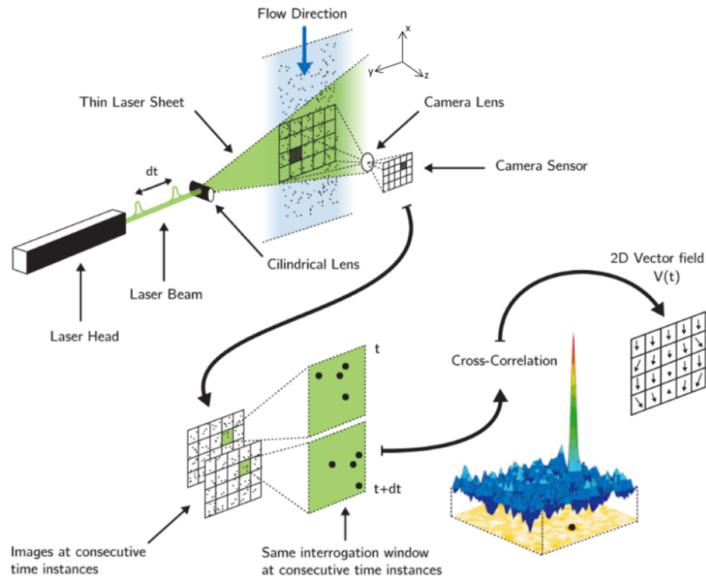


Figure 3.1: Process flow schematic of a planar PIV system, adapted from Dantec Dynamics (2021) and Lavision GmbH (2018).

Tracer particles are inserted into the fluid flow and a pulse of laser light illuminates the tracers twice with a time separation Δt . The laser light is shaped into a thin region and the light scattered by the particles within the field-of-view (FOV) is collected with a digital camera. The captured images are partitioned into multiple smaller areas, so called "interrogation windows" (IW), in which the digital cross-correlation of pixel intensity is evaluated that returns the particles motion between the two consecutive recordings.

Two main modes exist with respect to the timing of the measurement: dual-frame and single-frame (see Figure 3.2). The dual-frame configuration represents the most used recording arrangement in PIV experiments. In dual-frame mode image pairs are collected with a small time separation between the frames (Δt). As a rule of thumb, Δt is chosen such to obtain a displacement of about 10 pixels for a reference region of the flow field. The time between the pairs (ΔT) is dictated by the recording rate (typically 10 - 30 Hz for CCD). In single-frame mode, also known as time-resolved mode, a continuous series of images is recorded, typically at high frame-rate (1-10 kHz).

While a brief explanation of the general setup and theoretical principles is provided

in this chapter, the reader is referred to the book of Raffel et al. (2018) for a more comprehensive discussion of the technique.

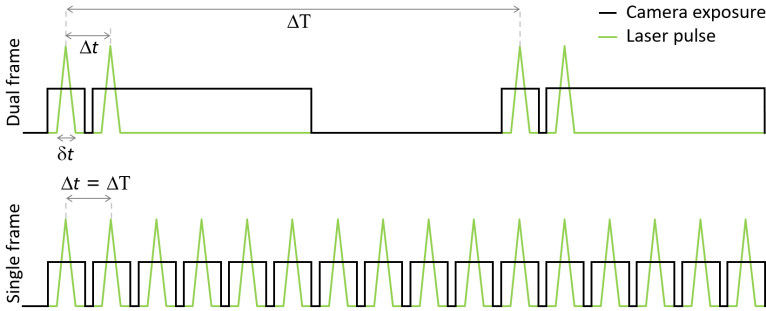


Figure 3.2: Dual frame and single frame (time-resolved) recording modes for PIV.

3.2. STEREOSCOPIC PIV

The intended applications for the Ring of Fire all have highly three-dimensional flow fields and therefore planar PIV is not suited. In order to measure the out-of-plane velocity component, stereoscopic-PIV (Stereo-PIV) can be employed (Prasad, 2000). The method relies on the stereoscopy principle, whereby two cameras observe the tracers' motion from a different viewing angle. Figure 3.3 illustrates the principle for one in-plane component and the out-of-plane one. The relation between the tracers velocity "perceived" by the cameras and that in physical space follows below Raffel et al. (2018):

$$u = \frac{u_1 \tan\theta_2 + u_2 \tan\theta_1}{\tan\theta_1 + \tan\theta_2} \quad (3.1) \quad v = \frac{v_1 + v_2}{2} \quad (3.2) \quad w = \frac{u_1 - u_2}{\tan\theta_1 + \tan\theta_2} \quad (3.3)$$

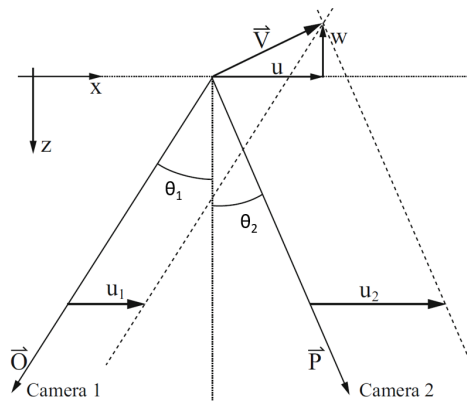


Figure 3.3: Reconstruction of the physical velocity from its stereoscopic projection (Raffel et al., 2018).

3.3. LARGE-SCALE PIV

The typical measurement domains for PIV experiments in airflows using micrometric particles (e.g. fog droplets) as flow tracers, are $30 \times 30 \text{ cm}^2$ and 50 cm^3 for planar PIV and 3D PIV, respectively (Raffel et al., 2018). The relatively small extent of conventional PIV measurement domains mainly stems from the limitations of the light source intensity in combinations with the small size of tracers, resulting in little scattered light intensity. With the introduction of helium-filled soap bubbles (HFSB; Bosbach et al. (2009)) as tracer particles for PIV, a significant jump in measurement domain was achieved. Despite them being patented already in 1938 (Caridi, 2018), HFSB have only been utilized for qualitative visualisations; their use for quantitative measurements was difficult due to the low production rate and the uncertainty of their tracing fidelity. In the last 20 years, the HFSB technology advanced with the design of sub-millimeter bubble generators by DLR (German Aerospace Agency, Figure 3.4a). This type of nozzle was named orifice type nozzle and used by Okuno et al. (1993) first, but only after the enhancements of DLR (Bosbach et al., 2009), the bubble generator was able to produce sub-millimetre bubbles (approximately 0.2-0.3 mm) at a production rate higher than 50,000 bubbles per second. These improvements opened the possibility to use the HFSB for quantitative flow visualisation such as large-scale PIV (Bosbach et al., 2009; Kühn et al., 2011). The term "large-scale PIV" is referred to the possibility of performing PIV with a FOV of the order of a square meter.

3.3.1. HELIUM-FILLED SOAP BUBBLES TRACERS

The choice of the appropriate tracer particle for PIV is important, as it must faithfully follow the fluid flow. To quantify the tracing fidelity, the particle's Stokes number, S , is considered, which is defined as the ratio of the particle response time, τ_p , over the flow characteristic time, τ_f . For instantaneous tracing characteristics, the Stokes number should be below 0.1 (Tropea et al., 2016). The response time of a small tracer in the Stokes regime is the time taken to follow a step-like change of velocity and reads as (Adrian and Westerweel, 2011):

$$\tau_p = d_p^2 \frac{(\rho_p - \rho)}{18\mu} \quad (3.4)$$

where μ and ρ are the fluid viscosity and density, and d_p and ρ_p are the particle diameter and density, respectively. To reduce the particle response time and thus the Stokes number, the particle size should be minimized or the tracer should be neutrally buoyant ($\rho \approx \rho_p$). For incompressible flows, Samimy and Lele (1991) conclude that the measurement error introduced by the slip velocity is linearly increasing with the Stokes number ($S = 0.2$ corresponds to an error of 2%).

HFSB are produced using a combination of air, helium and a bubble fluid solution (BFS; Figure 3.4a). The flow rates of these fluids are controlled by a fluid supply unit (FSU) to produce neutrally buoyant, lighter-than-air or heavier-than-air bubbles (Caridi, 2018). A response times of approximately $30 \mu\text{s}$ is reported by Faleiros et al. (2018) for HFSB that are close to neutrally buoyant ($\rho_p 1.1 \pm 0.05 \text{ kg/m}^3$). Apart from the response

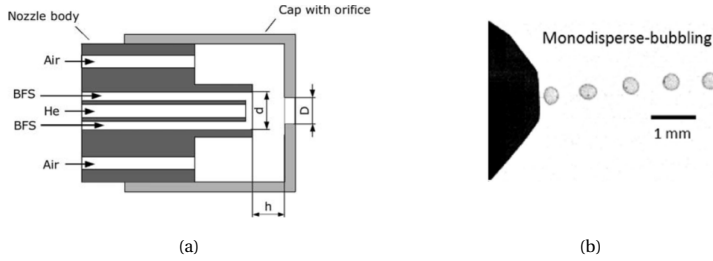


Figure 3.4: (a) Sketch of the DLR HFSB nozzle (Bosbach et al., 2009); (b) HFSB bubbling regime (adapted from Faleiros et al., 2019).

time, the fluid flow rates also affect the HFSB size, production rates and regimes (Faleiros et al., 2019). The latter authors provide guidelines to achieve the shortest response times and the preferred monodisperse-bubbling regime (see Figure 3.4b).

The reason why the HFSB are so attractive for large-scale measurements are their light scattering properties. The large particle diameter (compared to fog particles) results in a scattered intensity exceeding that of typically used micron-size tracers by a factor $10^4 - 10^5$. As a result a rapid increase of the number of investigations conducted with large-scale PIV is observed (e.g. Bosbach et al., 2009; Huhn et al., 2017; Jux et al., 2018; Martínez Gallar et al., 2019; Schneiders et al., 2016).

3.3.2. STATE-OF-THE-ART HFSB SEEDING SYSTEMS

A single HFSB generator is able to generate a seeded stream-tube of 3 cm width with no noticeable variation for a range of free-stream velocity between 1 and 30 m/s (Scarano et al., 2015) and hence is deemed unsuited for conducting large-scale PIV experiments. To increase both the rate of tracers injected in the flow as well as the size of the seeded stream-tube Caridi et al. (2016) introduced a dedicated seeding system consisting of a single bubble generator, a reservoir to accumulate the HFSB and a distribution rake to inject the seeding into the wind tunnel test section (Figure 3.5). The seeding density and seeded stream-tube were approximately 1 particle/cm³ and 30×36 cm², respectively.

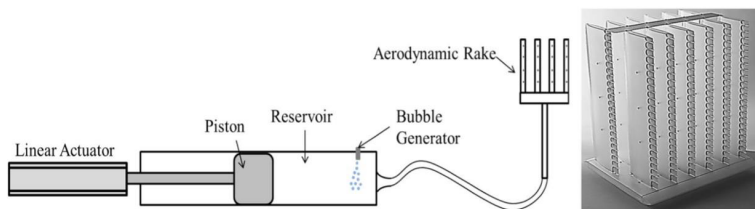


Figure 3.5: Sketch (left) and photo (right) of the HFSB seeding system used by Scarano et al. (2015) and Caridi et al. (2016). Figures reproduced from Caridi et al. (2016).

The design of the HFSB generators has advanced such that current generators (e.g. HFSB-GEN-V11 developed at TU Delft; Faleiros et al., 2018) are able to generate robust HFSB seeding in the monodisperse-bubbling regime. Furthermore, new seeding systems have been developed to achieve higher HFSB production rates and a larger seeded streamtube in the wind tunnel by increasing the amount of HFSB generators integrated in the seeder rakes (e.g. Gibeau et al., 2020; Mertens et al., 2021; Terra et al., 2020).

3

3.4. LOADS DETERMINATION FROM PIV

The whole-field measurement capability and non-intrusive nature of PIV makes it an ideal tool for aerodynamic load determination. The loads can be determined by invoking the conservation of momentum in a control volume surrounding the object. This approach returns the mean and instantaneous aerodynamic loads and has been applied in a variety of investigations on stationary models in wind tunnels, as demonstrated by van Oudheusden et al. (2007) and De Kat and Bleischwitz (2016). This section describes the theoretical framework to obtain both the pressure field and drag force from the velocity distribution.

3.4.1. MOMENTUM INTEGRAL CONTOUR-APPROACH

The forces acting on a body immersed in a fluid can be derived from the reaction of the flow to the presence of the object. The flow exerts its force through the surface pressure and the shear stress distributions. By application of the momentum conservation concept on a volume containing the object, the body force can be calculated. The application of the control volume principle relies on defining the control volume as a portion of a streamtube (Anderson, 2011), as visualized in Figure 3.6. In the particular case of an object moving on the ground, one of the streamsurfaces of the streamtube corresponds to the ground itself (see Figure 3.7).

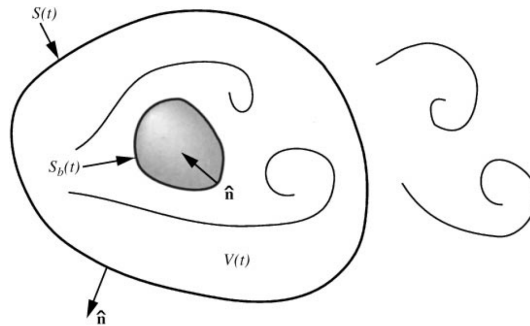


Figure 3.6: Basic working principle of the control-volume approach (adapted from van Oudheusden et al. (2007)).

It is common to study the aerodynamic loads in a fixed reference frame integral with the tested model in a wind tunnel ($R = \{X', Y', Z'\}$), as represented in Figure 3.7. It replicates the real life condition in which the model is moving at a constant velocity. In the

wind tunnel, the air is blown with a constant freestream velocity U_∞ corresponding to the model velocity in the real world. The instantaneous aerodynamic drag force $D(t)$ of the object can then be determined by the integral form of the momentum equation, which holds for incompressible flows (Mohebbian and Rival, 2012):

$$\underbrace{D(t)}_{\text{Force term}} = -\rho \underbrace{\iiint_V \frac{\partial \mathbf{u}}{\partial t} dV}_{\text{Unsteady term}} - \rho \underbrace{\iint_S \mathbf{u}(\mathbf{u} \cdot \mathbf{n}) dS}_{\text{Momentum term}} - \underbrace{\iint_S (p - p_\infty) \mathbf{n} dS}_{\text{Pressure term}} + \underbrace{\iint_S (\bar{\bar{\tau}} \cdot \mathbf{n}) dS}_{\text{Viscous term}} \tag{3.5}$$

where \mathbf{n} is the normal vector to the control surface S bounding control volume V , and ρ , \mathbf{u} , $p - p_\infty$ and $\bar{\bar{\tau}}$ represent density, velocity, relative pressure with respect to the ambient pressure, and viscous stress in the fluid, respectively. The evaluation of the volume integral on the right hand side of equation 3.5 by means of PIV measurements is not straightforward, but in the case of a two-dimensional flow, the full velocity field around the model can be accessed by using transparent models or complex optical techniques, as was done by van Oudheusden et al. (2007) and Unal et al. (1997). These studies include the analysis of steady forces (van Oudheusden et al., 2007), where the control-volume method was applied to a static airfoil at incompressible and compressible conditions, and the force estimation of an oscillating cylinder in an incompressible inviscid flow (Unal et al., 1997).

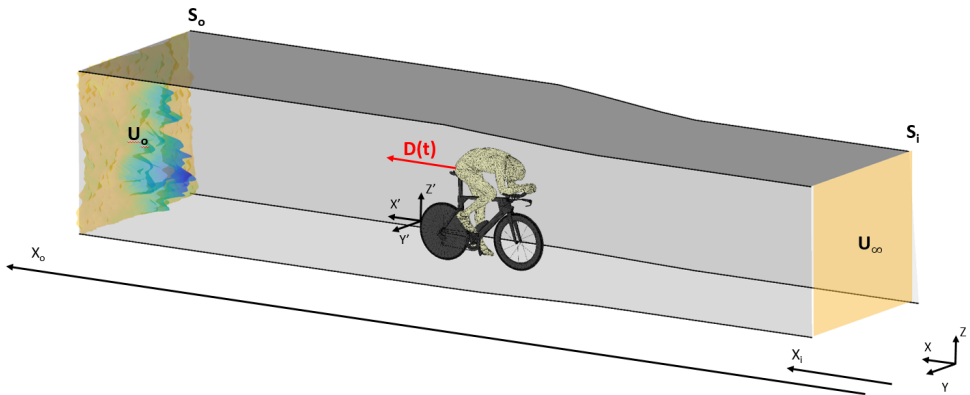


Figure 3.7: Control volume approach in the wind tunnel reference frame.

In order to simplify equation 3.5 some assumptions can be made. Firstly, the unsteady contribution to the drag force can be ascribed to the pedalling motion of the cyclist. The typical time-trial reduced pedalling frequency k^1 is approximately 0.1 (Crouch

¹The reduced frequency is a dimensionless parameter expressing the weight of unsteady phenomena with respect to steady phenomena. For the cyclist, it is a ratio of the leg speed around the crank and the freestream

et al., 2016) and thus the unsteady contribution to equation 3.5 is considered to be small and is subsequently neglected. Next, the change in momentum within the control volume is defined by the product of the mass flow through all control surfaces and the velocity. As stated above the side and top boundaries of the control volume are streamlines, so by definition, no mass crosses these surfaces ($\mathbf{u} \cdot \mathbf{n} = 0$). Furthermore, no mass can enter or leave through the ground plane. The net momentum flow across the control surfaces can thus be obtained by the surface integral over the inlet and outlet plane alone. Finally, the viscous effect on the drag force, measured at the control surfaces, is negligible, according to Kurtulus et al. (2007) and Mohebbian and Rival (2012). Based on this, equation 3.5 can be simplified to:

$$D(t) = \rho \iint_{S_i} u_\infty^2 dS + \iint_{S_i} (p_\infty - p_i) dS - \rho \iint_{S_o} u_o^2 dS - \iint_{S_o} (p_\infty - p_o) dS \quad (3.6)$$

with the index i referring to the inlet plane and o to the outlet one, with flow velocity u_∞ and u_o , respectively. In Figure 3.7, u_∞ is represented by a constant contour level, while the velocity deficit u_o is shown at the outlet plane. Application of conservation of mass in incompressible flows ($\rho \iint_{S_o} u_o dS = \rho \iint_{S_i} u_\infty dS$) yields:

$$D(t) = \rho \iint_{S_o} (u_\infty - u_o) u_o dS + \iint_{S_o} (p_o - p_i) dS \quad (3.7)$$

Equation 3.7 requires to only measure the streamwise velocity component at the outlet plane (u_o) and to integrate the freestream velocity (u_∞) on the same area. By repeated measurements of the instantaneous drag force, statistical information can be obtained. In the remainder of this work the uncertainty on the average drag force will be indicated by the 95% confidence interval (CI), which is defined as (ref):

$$CI_{95\%} = \bar{D} \pm z \frac{\sigma}{\sqrt{N}} \quad (3.8)$$

where \bar{D} is the sample mean drag, z is the confidence level value, σ is the sample standard deviation, and N is the sample size.

3.4.2. PRESSURE EVALUATION FROM PIV

The static pressure is required for the evaluation of the aerodynamic drag using equation 3.7. For incompressible flows, the momentum equation can be used to express the gradient of the pressure field, ∇p , in terms of the velocity field:

$$\nabla p = -\rho \frac{D\mathbf{u}}{Dt} + \mu \nabla^2 \mathbf{u} \quad (3.9)$$

where $D\mathbf{u}/Dt$ is the material acceleration, the acceleration of a fluid's particle in a Lagrangian perspective, and μ the fluid's dynamic viscosity. From an Eulerian perspective, the material acceleration can be expressed in terms of local and convective time derivatives:

flow $k = 2\pi r f / U_\infty$ that can be written as a sole function of the bike geometry $k = r / (GR)$, with f the pedalling cadence, r the crank length, R the wheel radius, G the gear ratio.

$$\frac{D\mathbf{u}}{Dt} = \frac{\partial\mathbf{u}}{\partial t} + \mathbf{u} \cdot \nabla\mathbf{u} \quad (3.10)$$

After substitution of equation 3.10 into equation 3.9, the pressure gradient reads as:

$$\nabla p = -\rho \left(\frac{\partial\mathbf{u}}{\partial t} + \mathbf{u} \cdot \nabla\mathbf{u} \right) + \mu \nabla^2 \mathbf{u} \quad (3.11)$$

The above pressure equation can be used to obtain the pressure at the control surface through the spatial integration of the pressure gradient. The pressure boundary conditions are usually described in the undisturbed flow region. However, as a consequence of spatial integration, this method is subject to error propagation (e.g. van Oudheusden, 2013). Alternatively, the Poisson equation of pressure can be solved, which is obtained after taking the divergence of equation 3.11:

$$\nabla^2 p = -\rho \nabla(\mathbf{u} \cdot \nabla)\mathbf{u} \quad (3.12)$$

The simplified PPE (equation 3.12) is valid for incompressible thus divergence free ($\nabla \cdot \mathbf{u} = 0$) velocity fields. It is noted here that for a complete evaluation of the above equation, all three velocity components and their spatial derivatives are needed. Although all three components of the velocity field can be obtained from stereo-PIV, spatial gradients can only be obtained for the in-plane velocity components. The gradients of the out-of-plane velocity components can be estimated by invoking Taylor's frozen turbulence hypothesis (Zaman and Hussain, 1981). However, it is known that the convection velocity of the wake of the cyclists varies both in-plane and out-of-plane (with distance in the wake) (Crouch et al., 2014). Further, the accuracy of this gradient is dependent on the temporal resolution of the velocity field. Therefore, the estimation of this out-of-plane gradient would introduce more error than when neglected. Hence, the in-plane velocity components can be used to obtain planar pressure fields, where the PPE simplifies to:

$$-\frac{1}{\rho} \left(\frac{\partial^2 p}{\partial y^2} + \frac{\partial^2 p}{\partial z^2} \right) = \left(\frac{\partial v}{\partial y} \right)^2 + 2 \frac{\partial v}{\partial z} \frac{\partial w}{\partial y} + \left(\frac{\partial w}{\partial z} \right)^2 \quad (3.13)$$

3.5. PIV IN CYCLING AERODYNAMIC RESEARCH

To date many of the studies where PIV has been used for flow visualization in cycling aerodynamics often were limited to the local flow features. Celis and Ubbens (2016) for example investigated the local flow features around the seatpost of a bicycle. The authors wanted to show that PIV can be used to investigate the effect of small geometrical changes on the flow field, such as adding a groove in the seatpost of a bicycle in order to decrease the wake behind it. Another study by Chabroux et al. (2010) performed stereo-PIV measurements behind the helmet of a model cyclist. The authors acquired multiple planes with a 50 mm streamwise spacing in the wake of the helmet, showing the ambition of the community to acquire data in a three dimensional volume. This setup, which is shown in Figure 3.8, already shows similarities to how the Ring-of-Fire PIV setup is imagined. The results contributed to determine the characteristics of the wake flow development behind a helmet.

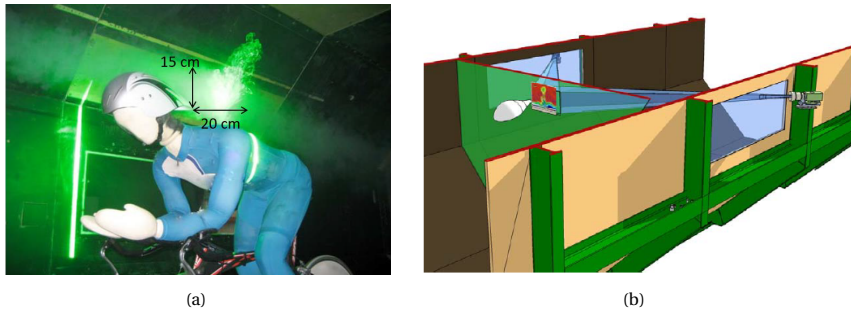


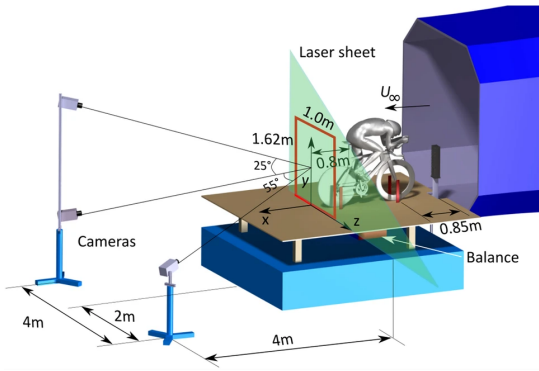
Figure 3.8: Measurement setup used by Chabroux et al. (2010).

Both studies of Celis and Ubbens (2016) and Chabroux et al. (2010) involve full-scale test objects, however, they only investigate local flow features with a measurement area in the order of $200 \times 200 \text{ mm}^2$, is small in relation to the size of an actual athlete. More recently, and with a similar size of the measurement domain, PIV was conducted in a water channel to characterize the wake of 1:7 scaled cyclist models (Barry et al., 2016a). This setup resulted in a Reynolds number one order of magnitude smaller than in reality.

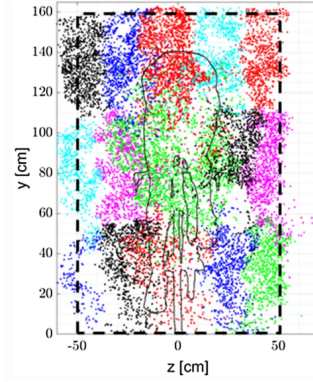
The use of helium-filled soap bubble (HFSB) as tracers (Section 3.3) made it possible to perform PIV measurements at the scale of several square meters (Bosbach et al., 2009; Kühn et al., 2011). The research group at the Technical University of Delft made use of this to investigate the flow field around a static, full-scale model of Tom Dumoulin in time trial position. Two different experiments were conducted at different wind velocities, the first conducted tomographic PTV measurements in the wake of the model (Terra et al., 2019), the second experiment acquired tomographic PTV data all around the model with a robotic coaxial PIV system (Jux et al., 2018). In the former study Lagrangian particle tracking was used to obtain the velocity and static pressure statistics in a thin volume in the wake of a cyclist mannequin at freestream velocities between 12.5 and 15 m/s. The authors were able to scan an area of $1 \times 1.7 \text{ m}^2$, which, compared to the previously discussed works, was a significant increase in the measurement volume. This was made possible by moving around the HFSB seeder and combining the data sets later on. The spatial distributions of the time-average streamwise velocity and pressure coefficient in this work matched well with the results presented in the work reported by Crouch et al. (2014). A schematic representation of the experimental setup and the Lagrangian particle tracks in the wake of the model can be seen in Figures 3.9a and 3.9b, respectively.

Jux et al. (2018) used a novel robotic Coaxial Volumetric Velocimetry (CVV) system to capture the flow field around a full-scale static cyclist mannequin. Time averaged flow field on a 2 m^3 domain was obtained for a freestream velocity of 14 m/s. The flow topology agreed well with that established in literature and provided new insights in surface friction, stagnation points, separation and reattachment (Figure 3.10).

Despite the big leap in size of the measurement domains in the previous two studies, there are still a few shortcomings. The test setup shown in Figure 3.9a, for example, is very complex to build up and calibrate. The coaxial robotic PTV system used by Jux

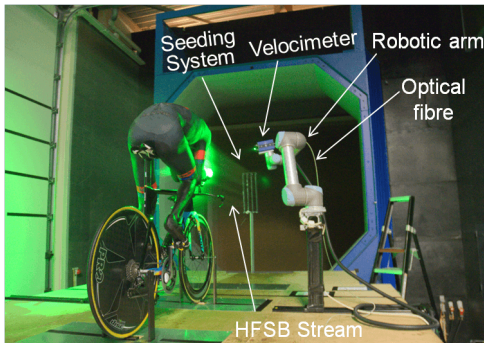


(a) Schematic representation of the experimental setup.

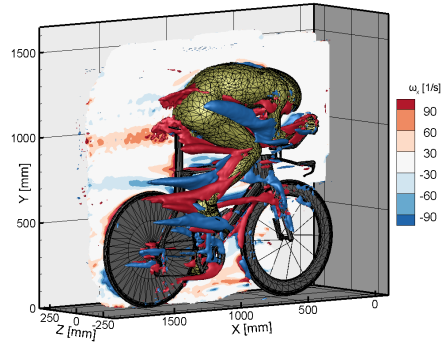


(b) Lagrangian particle tracks in the wake of the model. Colours indicate different seeder locations.

Figure 3.9: Illustration of measurement setup and Lagrangian particle tracks presented by Terra et al. (2019).



(a) Picture of the experimental setup.



(b) Isosurfaces of Q-criterion coloured by streamwise vorticity

Figure 3.10: Robotic coaxial volumetric velocimetry setup and corresponding iso-surfaces of streamwise vorticity found by Jux et al. (2018).

et al. (2018) does not have this problem, however, obtaining the 450 runs to cover the whole measurement domain was very time consuming. Furthermore, both experiments were performed on a static model and were still composed of multiple individual PIV acquisitions. The full measurement domain could not be seeded with sufficient HFSB concentration at the same time, resulting in the fact that only the time-averaged flow could be measured.

3.6. THE RING OF FIRE

The Ring of Fire concept, as introduced in Chapter 1, performs on-site, large-scale PIV measurements on a moving cyclist. The experimental setup of this type of measurement is not straightforward and therefore, this section will provide the reader with a general

description of the different components of the system.

Figure 3.11 shows a schematic of the Ring of Fire, indicating the main components. The largest component of the system is the tunnel, whose function is to contain the HFSB in the measurement region. Illumination of the bubbles is provided from the side of the tunnel by a laser, illuminating a thin plane perpendicular to the direction of motion of the cyclist. Before each measurement, the HFSB are injected into the tunnel, creating a cloud of uniform seeding inside the tunnel. Once the athlete passes, images are acquired by digital cameras in stereoscopic configuration, allowing to measure both the in-plane and out-of-plane velocity components. Finally, in front of the entrance of the tunnel a triggering system is installed, which allows for synchronisation between the cyclist passage and the image acquisition.

3

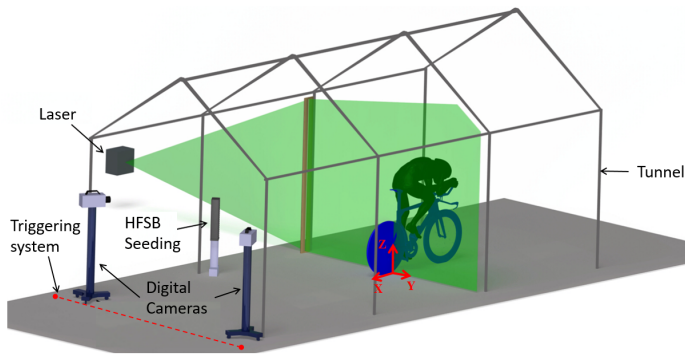


Figure 3.11: Schematic representation of the Ring of Fire.

II

DEVELOPMENT AND ASSESSMENT OF THE RING OF FIRE SYSTEM



4

FEASIBILITY AND FULL SCALE ASSESSMENT

This chapter describes the practical implementation of the Ring of Fire (RoF) on a full scale. Two full-scale experiments are conducted, indoor and outdoor, in which attention is placed on the effects of the environmental conditions and the confinement of the measurement region. Stereo-PIV measurements feature a plane of approximately $2 \times 2 \text{ m}^2$, using HFSB as flow tracers. The experimental setup and procedures of both experiments are discussed in Section 4.3. The results, discussed in Section 4.4, show that the flow topology in the wake of the cyclist compares satisfactorily between both experiments and with wind tunnel experiments reported in literature. The current measurements clearly separate drag values from upright and time trial athlete's postures, indicating the suitability of this principle for aerodynamic analysis and optimization studies.

This chapter has been published as: **Spoelstra A.**, de Martino Norante L., Terra W., Sciacchitano A. and Scarano F. (2019) On-site cycling drag analysis with the Ring of Fire. *Experiments in Fluids*, 60(6):90.

4.1. INTRODUCTION

The works of Terra et al. (2017, 2018) with tomographic PIV in combination with HFSB to determine the drag of a towed sphere can be seen as preliminary to this research. Terra et al. (2017) showed that, similar to the formulation used for wind tunnel PIV wake rakes, the aerodynamic drag of a transiting sphere can be evaluated via a control volume approach. However, in addition to the wake flow, the velocity prior to model passage also needs to be measured because the environmental flow conditions prior to model passage are unknown. Furthermore, it was observed that the aerodynamic drag coefficient is practically unaffected by the distance into the wake where the momentum integral is evaluated and that the pressure term becomes negligible after 5 characteristic length scales. In a second experiment Terra et al. (2018) repeated the measurements at five different model velocities in a narrow Reynolds number range, in which the drag coefficient is assumed constant. It was concluded that, when the environmental conditions are accounted for, the PIV wake rake for transiting bluff bodies returns the average drag force and coefficient from multiple model passages with a drag resolution of the order of 20 drag counts ($\Delta C_D = 0.02$). The use of HFSB offers the potential to upscale the measurement region in such experiments up to several square meters as demonstrated by Bosbach et al. (2009) and discussed in Section 3.3.

The current chapter describes the realisation of the first RoF for full-scale sport aerodynamics and discusses the experimental procedures, measurement accuracy and sources of uncertainty for indoor and outdoor experiments, mimicking respectively track and road cycling. The experimental procedure to achieve drag measurements follows the same principles discussed by Terra et al. (2017). The measurements are performed by large-scale stereoscopic-PIV over a field of view of about 4 m^2 and the drag is obtained by invoking the conservation of momentum in a control volume. The aerodynamic drag estimation from cyclists during sport action is compared to literature data from wind tunnel experiments and computational fluid dynamics (CFD) simulations, but also to other techniques currently practiced for on-site measurements (coast down, Petrushov (1998); torque power output, Grappe et al. (1997)). In addition, the correlation between the drag forces and the flow field in the wake is supported. Furthermore, the experiments cover different postures of the cyclist (time trial and upright) with the aim to directly measure the effect of posture on aerodynamic drag and its detectability with the RoF.

4.2. METHODOLOGY

In contrast to typical wind tunnel conditions with a cyclist at rest, in the Ring of Fire the cyclist is in motion, transiting through a fixed measurement plane (i.e. the laboratory frame of reference, $R = \{X', Y', Z'\}$ in Figure 4.1); consequently, the control volume is considered to move with the cyclist ($R = \{X, Y, Z\}$ in Figure 4.1) at constant cycling velocity u_C with respect to the laboratory frame of reference. The example of a cyclist is considered here, although the conclusions can be extended to other problems such as ground vehicles and speed sports in general.

Unlike in the wind tunnel, where the freestream velocity is uniformly distributed, the air motions prior to the passage of the cyclist feature a chaotic velocity u_{env} , result-

ing from the environmental effects, as depicted in Figure 4.1-top. Assuming uniform and quiescent conditions prior to the passage would largely simplify the problem formulation. However, even in scaled experiments, the disturbances in the air motion induced by the environment and the seeding generation are reported not to be negligible (Terra et al., 2018). Therefore, in the RoF it is necessary to obtain the velocity field in the planes before and after the transit of the cyclist. After the passage of the cyclist, the flow velocity features a coherent wake with a velocity profile, u_{wake} , that follows the moving cyclist. A schematic of this situation is shown in 4.1.

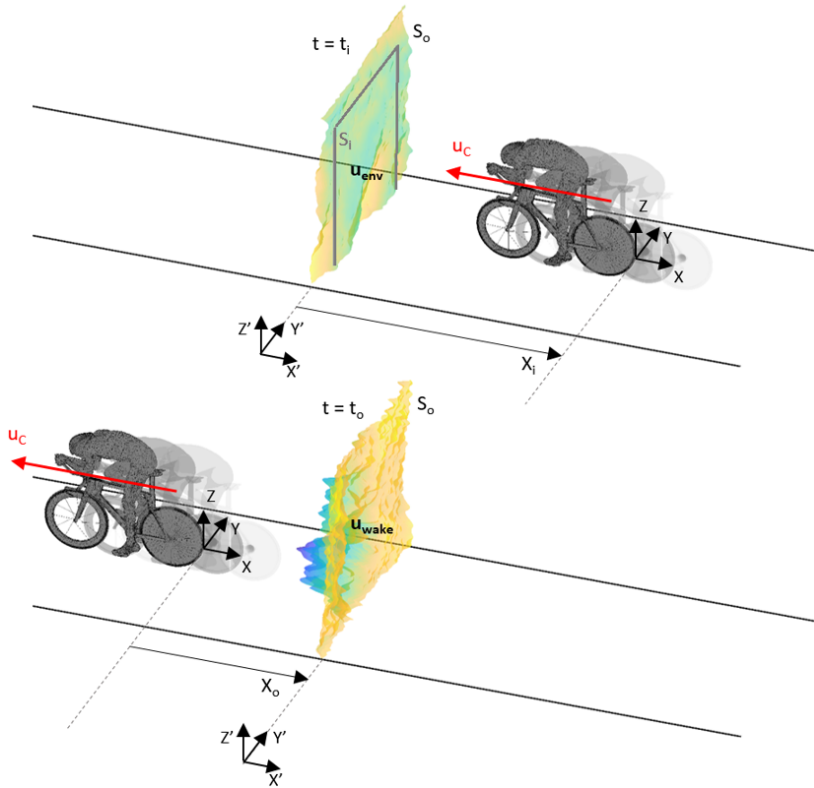


Figure 4.1: Control volume approach in the Ring of Fire: upstream flow (u_{env}) measured at t_i , downstream flow (u_{wake}) at t_o (adapted from de Martino Norante (2018)).

Making use of a Galilean transformation, the representation of velocity and momentum changes from the laboratory to the cyclist frame of reference moving at speed u_C . As a result, the air flow velocity upstream of the cyclist can be written as $u_\infty = u_{env} - u_C$, while downstream as $u_o = u_{wake} - u_C$. Substituting u_∞ and u_o in equation 3.6 yields:

$$\begin{aligned}
D(t) = & \rho \iint_{S_i} (u_{env} - u_C)^2 dS + \iint_{S_i} (p_\infty - p_i) dS \\
& - \rho \iint_{S_o} (u_{wake} - u_C)^2 dS - \iint_{S_o} (p_\infty - p_o) dS
\end{aligned} \tag{4.1}$$

This expression is valid at the condition that the mass flow is conserved across S_i and S_o . This is ensured by shrinking the inlet plane (S_i) from the outer edges, starting from the equal size as that of the outlet plane (S_o). In the far wake ($X > 5$ characteristic length scales) the pressure term can be neglected (Terra et al., 2017) and the drag can be written as:

4

$$D(t) = \rho \iint_{S_i} (u_{env} - u_C)^2 dS - \rho \iint_{S_o} (u_{wake} - u_C)^2 dS \tag{4.2}$$

Equations 4.1 and 4.2 yield the instantaneous aerodynamic drag from the surface integral over a fixed plane before and after passage of the cyclist. Ensemble averaging (equation 4.3) of the drag among multiple passages is performed to achieve a higher degree of statistical convergence.

$$\overline{D}(t) = \frac{1}{N} \sum_{j=1}^N D_j(t) \tag{4.3}$$

where N is the number of model passages. The aerodynamic drag exhibits temporal fluctuations associated with the unsteady nature of the flow around the cyclist. However, these unsteady fluctuations are little relevant to the evaluation of the cyclist's drag, given their short time scale. Time averaging is therefore performed within the ensemble average (equation 4.4) with the objective of reducing the effect of the unsteady fluctuations.

$$\overline{\overline{D}} = \frac{1}{T} \sum_{i=1}^T \overline{D}(t_i) \tag{4.4}$$

Where T is the total time and $\overline{D}(t_i)$ is the ensemble average drag at each time step in the wake.

4.3. EXPERIMENTAL SETUP AND PROCEDURES

Experiments were conducted with a cyclist riding a time trial bike. For the indoor case the cyclist was male, 1.89 m tall, with a mass of 68 kg. He wore a short-sleeve time trial suit from Team Sunweb and giant rivet TT helmet. The athlete that participated in the outdoor setup was 1.84 m tall and weighed 83 kg at the moment of testing. He was equipped with a long sleeved time trial suit from Team Blanco and a Lazer Wasp TT helmet. Moreover, for safety reasons, both cyclists wore a pair of laser goggles. The shoulder width was chosen as characteristic length scale, c . For both athletes this was approximately 600 mm. In the indoor experiment a Giant Trinity TT Advanced Pro bike with 2×11 gears was used, while a Ridley Cheetah TT bike with 2×9 gears was used for the outdoor experiment.

4.3.1. EXPERIMENTAL FACILITIES AND CYCLING CONDITIONS

The experimental facilities and test conditions are presented in Table 4.1. The top-view of the sport hall and of the outdoor site is shown in Figure 4.2. The flow tracers were generated and confined within a tunnel of $4\text{m} \times 3\text{m}$ and $3\text{m} \times 2\text{m}$ [width \times height] for the indoor and outdoor experiments respectively. Curtains were used to maintain a high concentration of tracers within the duct. The entrance and the exit in the outdoor experiment were closed during accumulation and opened prior to the transit of the cyclist. For the indoor experiment a curtain at the exit was sufficient. The measurement plane was near the half of the duct. Considering the small blockage ratios of 3.5 and 7 % for the indoor and outdoor experiments, respectively, a non-confined environment was assumed for the control volume approach. The floor was covered with a thin carpet (Polypropylene, 3 mm) to avoid ground slipperiness due to the PIV seeding. A photograph of the setup of both experiments is shown in Figure 4.3 and Figure 4.4. During the indoor experiment the cameras were positioned 6 m upstream of the duct entrance.

Table 4.1: Overview of experimental parameters and conditions.

Experimental parameter	Indoor	Outdoor
Duct dimensions [m^3]	$10 \times 4 \times 3$ [x,y,z]	$6 \times 3 \times 2$ [x,y,z]
Solid blockage [%]	3.5	7
Cyclist velocity (u_C) [m/s]	5.3 ± 0.1	8.3 ± 0.2
Reduced pedalling frequency (k)	0.12	0.23
Crank length [mm]	175	172.5
Acceleration length [m]	25	30
Deceleration length [m]	10	40
Torso length based Reynolds number	2.1×10^5	3.2×10^5

Although the two experiments have similar acceleration length before the measurement plane (Figure 4.2), the limited available braking length in the indoor experiments requires conducting the tests at lower velocity (5.3 m/s). The crank angle φ is defined as the angular position of the right foot (forward) with respect to horizontal crank position (Figure 4.5a).

In both the cases, measurements are conducted with the cyclist in upright and time trial position (see Figure 4.5). Following Crouch et al. (2014), the pedalling frequency (cadence) is normalized with the advancing speed, $k = \frac{2r\pi f}{u_C}$, where r is the bike crank length, f the cadence and u_C the cyclist velocity, as reported in Table 4.1. The reduced frequency is $k = 0.12$ indoor and $k = 0.23$ outdoor, respectively.

4.3.2. PIV INSTRUMENTATION, IMAGING AND DATA ACQUISITION

Velocity measurements are performed with a large-scale stereoscopic-PIV system. The experimental parameters are presented in Table 4.2. Neutrally buoyant helium-filled

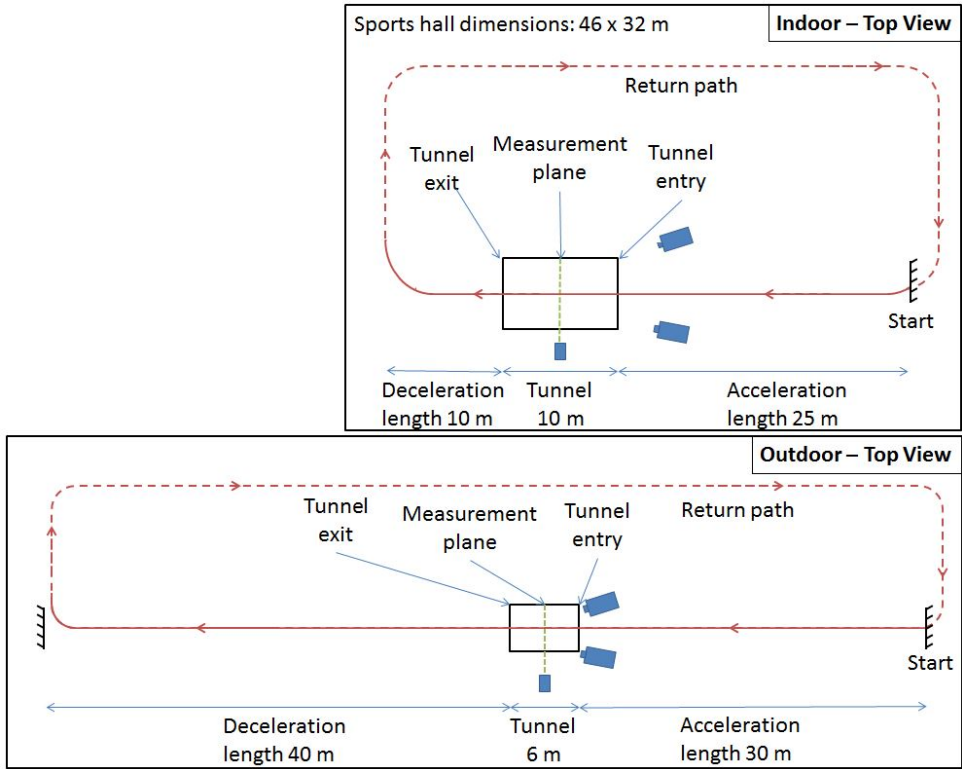
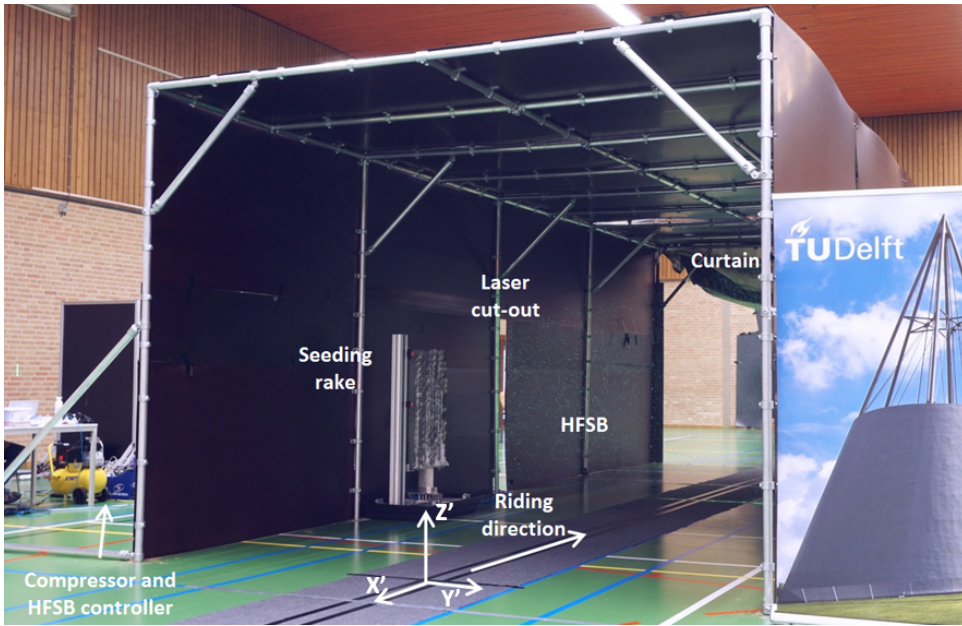


Figure 4.2: Top-view schematics of the indoor (top) and outdoor (bottom) field facility for the feasibility study.

soap bubbles (HFSB) are used with an average diameter between 0.3 and 0.4 mm, providing sufficient light scattering to visualize a field of view (FOV) of the order of 4 m^2 . The tracers are introduced in the measurement region by a 200 and 80 nozzles rakes in the indoor and the outdoor experiment, respectively. A LaVision HFSB fluid supply unit (FSU) controls soap, air and helium rates towards the seeding rake. The tracers concentration achieved during experiments is of 5 bubbles/cm^2 and 3 bubbles/cm^2 for indoor and outdoor, respectively. Based on previous studies (Faleiros et al., 2019; Scarano et al., 2015), in the above conditions a tracers response time in the order of 10 to $100 \mu\text{s}$ is expected. The tracers Stokes number based on cyclist velocity (u_C) and shoulder width (c) is in the order of 10^{-3} .

In the indoor experiment, a low repetition-rate PIV system is used, whereas the outdoor experiment features high-speed PIV (see Table 4.2 for specifications). The results are not affected by the selection of the hardware, which is different only due to the availability at the time of the experiment. The low-speed system benefits from the higher pulse energy and sensor resolution with well resolved particle images (diffraction disk covered with approximately 2 pixels). On the other hand, the high-speed system offers three orders of magnitude higher temporal resolution, enabling more advanced data processing, at the cost however of a lower imaging resolution (diffraction disk imaged



4

Figure 4.3: Experimental setup in indoor conditions.

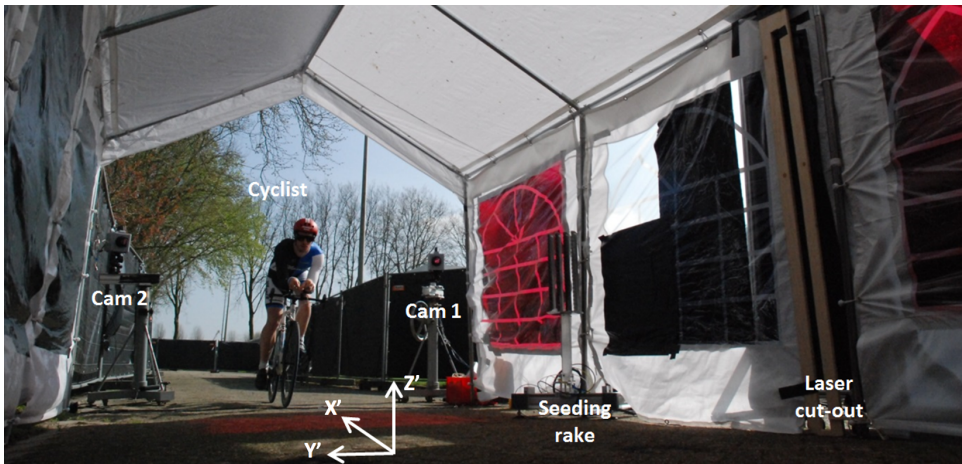


Figure 4.4: Experimental setup in outdoor conditions.

over 0.5 pixels). The pulse separation with the low-speed system is chosen considering the out-of-plane loss-of-correlation factor (Keane and Adrian, 1992). A cross-correlation analysis with multi-grid image deformation (Scarano and Riethmuller, 2000) is employed. A typical recording of particle images is shown in Figure 4.6 for both experiments. The more controlled environment conditions in the indoor experiment result in a more uni-

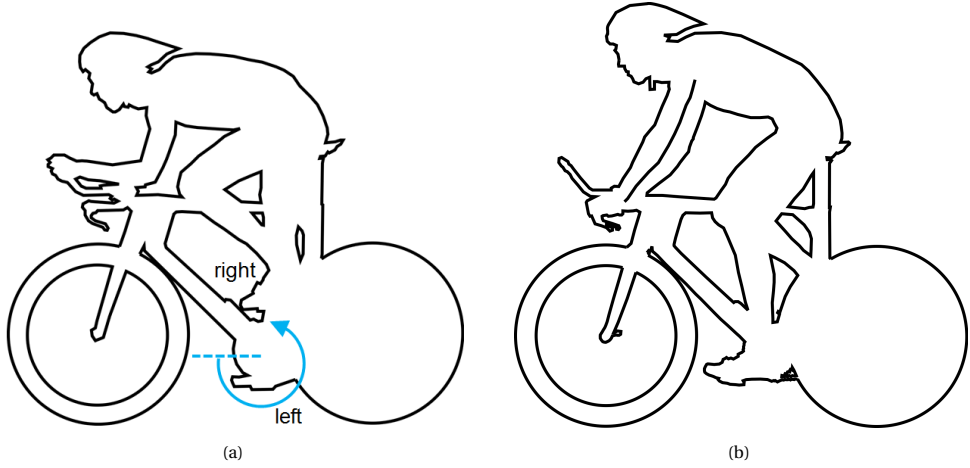


Figure 4.5: Cyclist posture during the experiments: (a) time trial and (b) upright

Table 4.2: Equipment and setup parameters.

		Equipment	
Purpose	Instrument	Indoor (Low-speed PIV)	Outdoor (High-speed PIV)
Imaging	Cameras	LaVision Imager LX 2MP interline CCD (1628×1236 pixels, pixel pitch 4.4 μm, 14 bits)	Photron FastCAM SA1 cameras (CMOS, 1024×1024 pixels, pixel pitch 20 μm, 12 bits)
	Objectives	2×AF Nikkor f=35 mm	2×AF Nikkor f=50 mm
	Others	Bandpass filter (532 nm)	Bandpass filter (532 nm)
Illumination	Laser	Quantel Evergreen 200 Nd:YAG (2×200 mJ at 15 Hz)	Quantronix Darwin Duo Nd:YLF (2×25 mJ at 1 kHz)
Seeding	Tracer particles	Helium-filled soap bubbles	Helium-filled soap bubbles
	Seeding system	200 nozzles	80 nozzles
Imaging and acquisition parameters			
Purpose	Instrument	Indoor (Low-speed PIV)	Outdoor (High-speed PIV)
Field of view	X (Thickness) [cm]	4	3
	Y (Width) [m]	1.8	1.8
	Z (Height) [m]	2.4	1.8
Imaging	$f_{\#}$	5.6	5.6
	Magnification	0.00297	0.0111
	Object distance [m]	11.5	4
	Digital image resolution [mm/px]	1.5	1.8
	Stereoscopic angle, β [°]	28	31
Measurement rate	f_{acq} [Hz]	8	2000
Pulse separation	Δt [ms]	3	0.5
Seeding concentration	Particle imaging density	0.11	0.09

form dispersion of the tracers and PIV images with homogeneous concentration. Achieving uniform seeding distribution in the outdoor experiment is hampered by the effect of wind gusts. From the raw PIV images, the cyclist's crank angle at the moment of the passage through the laser sheet is determined with an accuracy of ± 10 degrees.

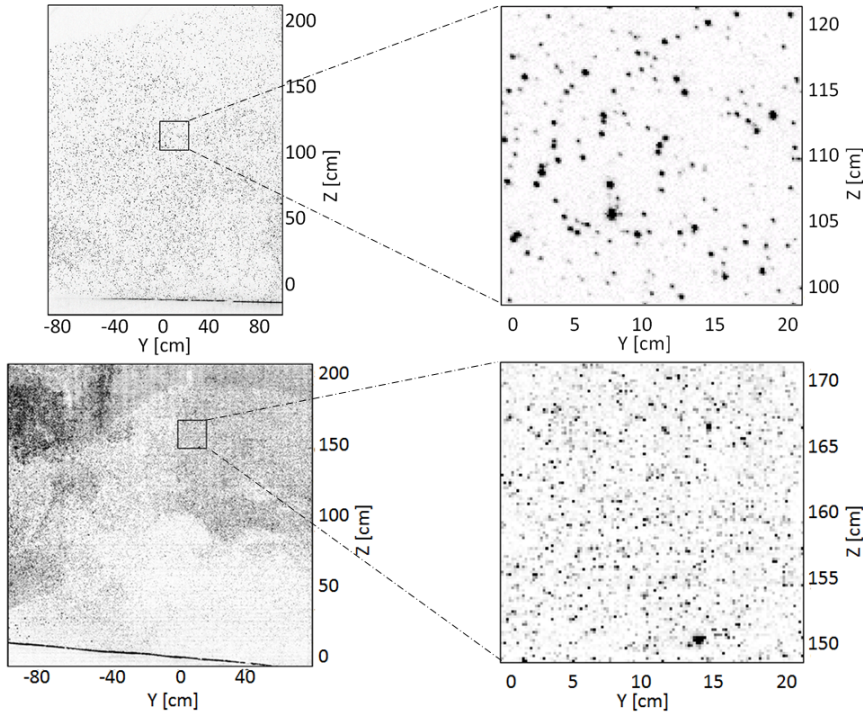


Figure 4.6: Digital recordings of particle images (left) and detail of particle images (right). Indoor (top) and outdoor (bottom) experiment. Intensity grey-scale inverted for clarity.

4.3.3. DATA PROCESSING

The recorded images are analysed with the LaVision DaVis 8 software. The pre-processing removes background light by subtracting the minimum intensity over time at each pixel. The recordings from the indoor experiment are analysed with dual-frame cross-correlation. The time separation between frames is set to 3 ms. A sliding sum-of-correlation algorithm (Sciacchitano et al., 2012) is employed for the outdoor experiment. For the latter, the analysis performs an average of the correlation maps from seven pairs of frames sliding a time interval of 3.5 ms. The time separation between frames is set to 2 ms. To quantify the range of resolvable velocity scales, the dynamic velocity range (DVR) is determined as the ratio between the maximum velocity in the near wake of the cyclist and the standard deviation of the velocity distribution in the quiescent flow prior to the cyclist's passage. Details of the image processing parameters and estimates of the measurement dynamic range are summarized in Table 4.3.

Table 4.3: Image processing parameters and expected dynamic range of measurements.

Parameter	Indoor	Outdoor
Correlation algorithm	Dual-frame cross-correlation	Sliding sum-of-correlation (Kernel size 7)
Interrogation windows	64 × 64 px (95 × 95 mm ²)	64 × 64 px (116 × 116 mm ²)
Overlap factor	75%	75%
Vector pitch	24 mm	29 mm
Dynamic spatial range (DSR)	25	15
Dynamic velocity range (DVR)	250	100

The drag force evaluation after one passage of the cyclist is obtained via Equation 4.2. The velocity field prior to the passage of the cyclist is significantly weaker than in his wake. Averaging the measurements before passage over a short time interval (1.25 seconds and 0.1 seconds for the indoor and outdoor experiment, respectively) reduces the effect of measurement noise in the determination of u_{env} . To further reduce the measurement noise in the drag estimate, a wake contouring approach is applied which isolates the cyclist's wake from the outer flow region. The wake is defined as the flow region whose velocity is below a certain fixed percentage (5% in the present case) of the minimum velocity in the flow field. Such region is then dilated by 2 adjacent vectors to include also the shear layers, thus obtaining the outlet surface S_o of Equation 4.1. The inlet surface S_i is obtained by shrinking S_i in all directions up to the point that the conservation of mass is satisfied. The cyclist's speed is monitored measuring the bicycle transit time across the light sheet. In the indoor experiment a magnetic sensor provides the cyclist speed in real time, additionally.

The wake past the cyclist exhibits unsteady behaviour. Consequently, also the evaluation of the drag force yields temporal variations. A statistically significant estimate of the cyclist's average drag is produced by ensemble and time averaging (Equations 4.3 and 4.4) the velocity field obtained from 10 and 28 repeated measurements for the outdoor and indoor conditions, respectively.

Two main repeatability issues are identified that require a specific treatment of the instantaneous data to retrieve ensemble average flow fields: 1) since the cyclist crosses the measurement plane at a different Y coordinate for every passage, the measured velocity field is relocated in the Y direction to compensate for such shift; 2) the relative distance between cyclist and measured wake planes is not exactly the same among different passages; the exact streamwise relocation is obtained examining the position of the cyclist when he crosses the measurement plane. For the latter problem, the high-speed PIV system resolves the motion of the cyclist within few millimetres in the streamwise direction, therefore any error associated with variations of the relative distance between cyclist and wake planes can be neglected.

Two right-handed coordinate systems are introduced; the system of reference that moves with the athlete, which is denoted with (X,Y,Z) and has its origin at the rearmost

point of the back of the athlete. A stationary system of coordinate (X',Y',Z') , with the origin at the laser sheet, is used to represent the positions with respect to the measurement location. In both coordinate systems the Z-axis is the vertical axis, positive upwards (see Figure 4.1). The streamwise velocity and vorticity in the wake of the athlete in the (X,Y,Z) frame of reference are made dimensionless with the velocity of the athlete u_C and its characteristic length scale c and reads as:

$$\text{Dimensionless streamwise velocity } u_x^* : \quad u_x^* = \frac{u_{wake} - u_C}{|u_C|} \quad (4.5a)$$

$$\text{Dimensionless streamwise vorticity } \omega_x^* : \quad \omega_x^* = \frac{\omega_x \cdot c}{|u_C|} \quad (4.5b)$$

The dimensionless streamwise velocity u_x^* is rewritten into the frame of reference of the cyclist, meaning that when $u_x^* = 0$, the velocity deficit equals the cyclist's velocity and when $u_x^* = 1$, there is no velocity deficit (equivalent to freestream condition). Unless differently specified, u_x^* refers to the ensemble-average wake velocity. These coordinate systems and dimensionless variables are used in the remainder of this work. Additionally, a dimensionless time is defined in order to make the comparison between results from different experiments possible:

$$\text{Dimensionless time } t^* : \quad t^* = \frac{t \cdot |u_C|}{c} \quad (4.6)$$

with $t = 0$ defined as when the rearmost point of the saddle crosses the laser sheet.

The uncertainty of the estimated time ensemble average $\overline{C_d A}$ values (from equation 4.4) is analysed a-posteriori, based on the standard deviation of the instantaneous drag area estimates, and the number of independent samples (considering both the number of passages of the cyclist, and the number of independent flow measurements in the wake of a cyclist during one passage). A detailed analysis of the measurement uncertainty and drag resolution of the Ring of Fire system for small-scale applications is reported in the recent work of Terra et al. (2018), where the effect of simplifications in the conservation of momentum equation is considered. The next chapter will address the uncertainty and drag resolution for a full-scale application.

4.3.4. MEASUREMENT PROCEDURE

Before the passage of the athlete, the duct curtains are closed and the HFSB accumulate for approximately two minutes. Atmospheric wind conditions require continuous operation of the seeding generator for the outdoor experiment. Instead, in the indoor experiment the bubbles production is paused prior to the passage of the cyclist and the momentum disturbance introduced by the seeding rake micro jets decays.

The cyclist starts from the same predefined distance and crank angle for each passage, to have well matching athlete posture (leg position) in the measured area between passages. In the indoor experiment, the image acquisition is triggered by a photoelectric sensor, while the user manually triggers the image acquisition in the outdoor experiment. Transferring the acquired images to mass storage requires 5 minutes with the

high-speed PIV system, whereas typically 40 image pairs are recorded with the low-speed PIV system permitting to repeat the experiment within one minute.

4.4. RESULTS AND DISCUSSION

4.4.1. QUANTITATIVE FLOW VISUALIZATION

AIR FLOW CONDITIONS BEFORE CYCLIST TRANSIT

The conditions before the passage of the cyclist rarely exhibit fully quiescent air. The environmental flow motions feature a velocity u_{env} , which is in general non-zero, non-uniform and non-stationary, mostly due to external conditions and the seeding injection. An instantaneous flow field before the cyclist's passage is illustrated in Figure 4.7 for both the indoor (left) and outdoor (right) experiments. In order to reduce the noise in the data, the velocity is averaged in time during 1.25 s (indoor) and 0.1 s (outdoor) before the passage of the athlete.

The indoor experiment was performed in a closed, thus quieter environment, whereas during the outdoor experiment, the presence of moderate wind (0.5 – 1 m/s) could only be partly attenuated by the walls of the tunnel. This is clearly visible in Figure 4.7, where the environment velocity is of the order of a 5 cm/s in the indoor experiment and attains 30 cm/s outdoor.

The velocity distribution prior to the passage is taken into account for the drag computation via Equation 4.1 as it contributes to the overall momentum budget, as also discussed by Terra et al. (2018). Furthermore, unsteady effects may influence the interaction of the wake with the initial velocity field, resulting in variations of the measured drag. The latter effects, however, are neglected and cannot be directly observed with the current experimental apparatus.

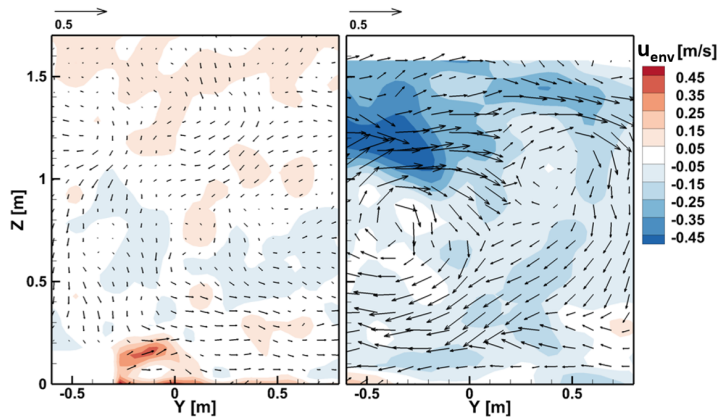


Figure 4.7: In-plane velocity vector field from an instantaneous run, averaged over a short time sequence (1.25 seconds and 0.1 seconds for the indoor and outdoor experiment, respectively) and colour contours of streamwise velocity component. Indoor conditions: 3.5 m (0.7 sec) in front of the cyclist (left); outdoor conditions: 2 m (0.25 sec) in front of the cyclist (right).

VELOCITY FIELD IN THE CYCLIST WAKE

The flow fields in the wake of the cyclist are discussed for the indoor upright and time-trial configuration as well as for the outdoor time-trial configuration. Figure 4.8 shows a comparison of the instantaneous streamwise velocity u_x^* at $t^* = 3$. Note that the cyclist contours in Figure 4.8 are meant to indicate the general cross section of the athlete and do not reproduce the exact position of the legs. The development of both an indoor as well as an outdoor instantaneous wake over time is available online in Spoelstra et al. (2019) as supplementary material.

First a comparison between upright (Figure 4.8a) and time-trial posture (Figure 4.8b) for the indoor experiment is given. The magnitude and location of the peak momentum deficit is similar in both cases. The out-of-plane velocity contour of the wake ($u_x^* = 0.95$), however, is clearly wider for the upright case. Interestingly, it has the same height for the time-trial position as it has for the upright position, despite a higher height of the cyclist in upright position.

Next, the time-trial position is compared between the indoor (Figure 4.8b) and outdoor experiments (Figure 4.8c). The wake observed in the outdoor experiment is wider and shows a slightly higher peak momentum deficit. Despite the heights of both cyclists in time trial position were very similar, in the indoor experiment, the $u_x^* = 0.95$ contour is consistently higher (see also Figure 4.9). A reason for this can be the different inclination angle of the torso of both cyclists, generating a different amount of downwash over the back.

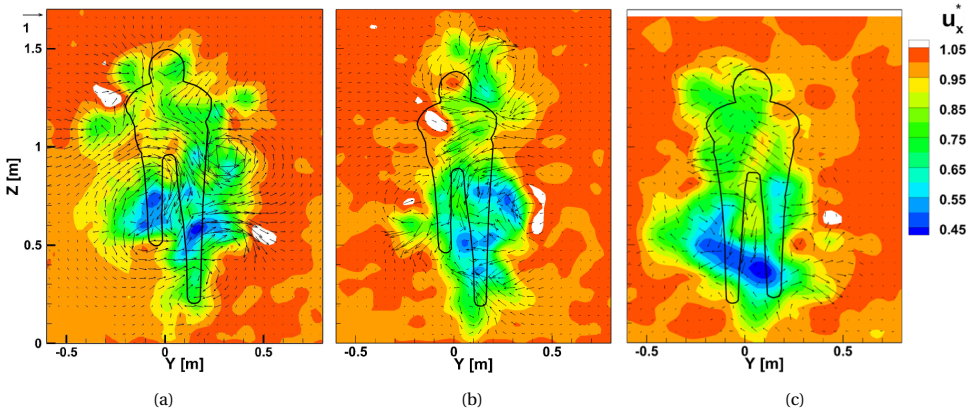


Figure 4.8: Dimensionless instantaneous streamwise velocity u_x^* at $t^* = 3$. (a) Indoor experiment upright position ($\varphi=65^\circ$); (b) Indoor experiment time trial position ($\varphi=65^\circ$); (c) Outdoor experiment time trial position ($\varphi=320^\circ$). Instantaneous wake development over time available online in Spoelstra et al. (2019).

The temporal development of the ensemble average streamwise velocity field ($\overline{u_x^*}$) past the cyclist are shown in Figure 4.9. The ensemble average is obtained from 28 and 10 individual runs from respectively the indoor and outdoor experiment. The maximum deficit in the wake ($\approx 45\%$) is observed at the shortest time delay after the passage. The deficit is not uniformly distributed and attains its maximum behind the legs. The turbulent diffusion causes a rapid redevelopment of the flow in the wake, as it is seen for the

individual runs as well. Considering its boundary by the contour where the streamwise velocity attains 95% of the undisturbed value, one observes that the flow entrainment smoothens the fine details of the streamwise velocity distribution and internally to the wake the peak velocity deficit reduces. The diffusion process causes the wake to exceed the measurement region, with consequences on the uncertainty of the drag estimate. This occurs earlier for the outdoor experiment ($t^* \sim 9$) than for the indoor experiment ($t^* \sim 13$), which is ascribed to the higher intensity of velocity fluctuations in the surrounding environment. The higher acquisition frequency of the outdoor experiment provides a more detailed look into the temporal development of the wake, however, at the cost of a lower accuracy and higher amount of erroneous vectors.

4

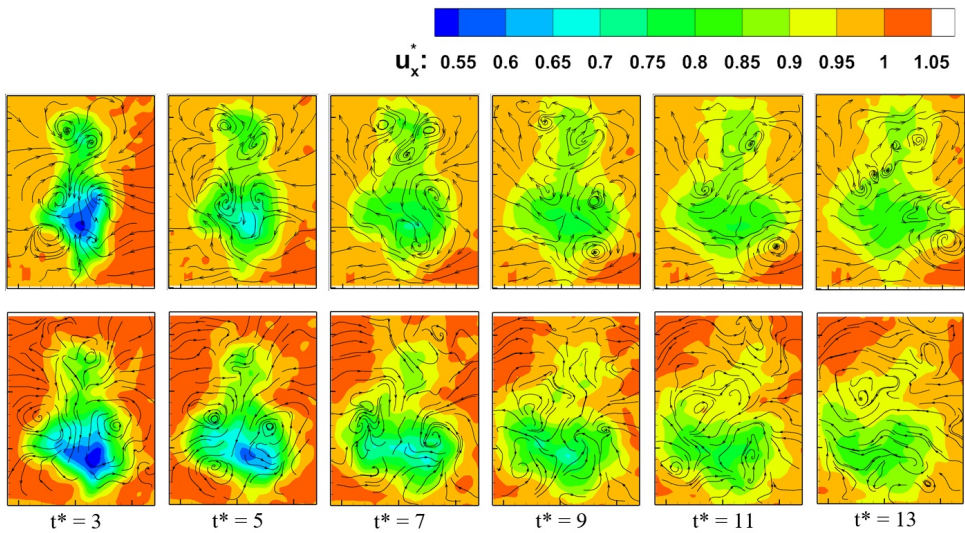


Figure 4.9: Development of the dimensionless ensemble average streamwise velocity over time. Indoor experiment (top) and outdoor experiment (bottom).

Next to the out-of-plane velocity, the similarity between the flow fields is also assessed by looking at the in-plane streamlines. It is apparent that the primary features are consistent throughout Figure 4.9, in that, close to the cyclist, a strong downwash exists near the vertical centreline. It can be reasoned that this characteristic is responsible for the downward movement over time of the wake structure. Furthermore, a strong inwash between 0.8 m and 1.2 m from the floor is induced by the main hip vortices in both experiments, which is further increased by the head vortices as seen in Figure 4.10. Over time, the hip/thigh vortex structure seems to outlast the smaller vortex structures, which in turn means that the former will dominate the wake behaviour in the far wake. There, the induced inwash causes a narrowing of the upper wake, while the broadening of the lower wake structure can be assigned to the induced outwash by the vortex pair, as well as the present ground, which constrains the downwash.

The analysis of the wake in terms of vorticity elucidates some of the characteristic aspects of the flow developing around and past the cyclist. Figure 4.10 illustrates and

compares the distribution of streamwise vortices as measured indoor (upright and time trial) and outdoor (time trial). Positive vorticity relates to counter-clockwise rotating vortices, while negative vorticity to clockwise ones.

The flow structures characterising the upright and time trial wakes from the indoor experiment are compared in Figure 4.10a and Figure 4.10b. There is substantial equivalence in the vortex structure strength and position, with the exception of the hip-thighs and the head vortices. In the former, the upright position shows higher vorticity on both sides. In the latter, the upright helmet vortices are negligible structures. Moreover, the upright posture shows new large scale structures, namely the shoulder vortex and the arm vortex couple. It is hypothesised that for each shoulder one outer vortex is shed. Its generation mechanism is proper of what has been called as a 3D separation. In fact, on both sides they are co-rotating with the hip vortices. This structure arises as a consequence of the very low pressure in the upper back of the cyclist. The arm vortex couple consists of an outer counter-rotating vortex with respect to the shoulder one and an inner co-rotating one. They are assumed to originate from the forward extended arms towards the brake hoods.

The vorticity field of the indoor and outdoor time trial position exhibits an overall agreement, although some details are not exactly reproduced. This may be ascribed to the torso angle, not fully repeated during indoor and outdoor experiments. The vorticity structure presented in Figure 4.10 also shows a good similarity with that reported in the studies of Crouch et al. (2014, 2016).

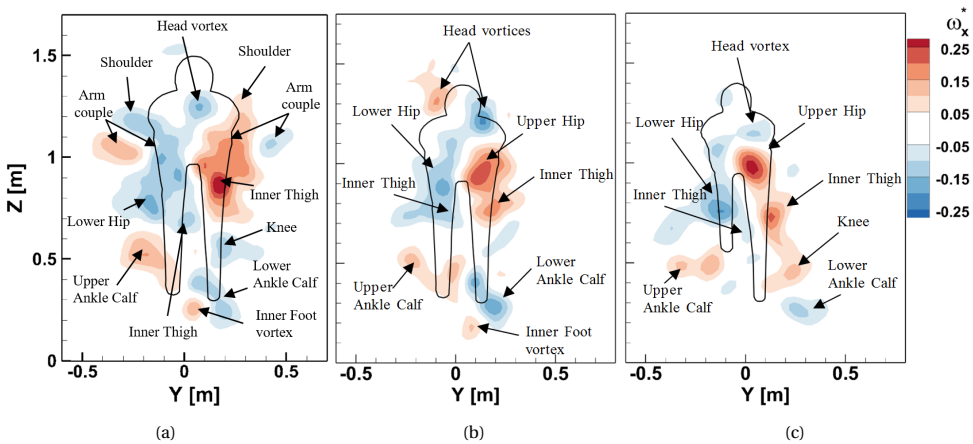


Figure 4.10: Streamwise, ensemble averaged vorticity ω_x^* at $t^*=1.5$. (a) Indoor experiment upright position ($\varphi=30^\circ$); (b) Indoor experiment time trial position ($\varphi=30^\circ$); (c) Outdoor experiment time trial position ($\varphi=290^\circ$).

4.4.2. AERODYNAMIC DRAG ANALYSIS

ENSEMBLE AVERAGE DRAG AREA

Following the authoritative review article from Crouch et al. (2017), the drag results are presented as drag area ($C_d A$). In fact, the overall aerodynamic efficiency of the cyclist is governed by both frontal area of the cyclists and the bike and the drag coefficient (shape of the cyclist and bike). Based on Equation 4.2 and on the procedures described in section 4.2, the instantaneous drag area is computed for each passage as a function of the dimensionless time. In Figure 4.11 the drag area evaluation is given for five passages with the cyclist in upright posture. In the outdoor experiment half a crank cycle is spanned along $\Delta t^* \approx 4$, while along $\Delta t^* \approx 7.5$ for the indoor experiment.

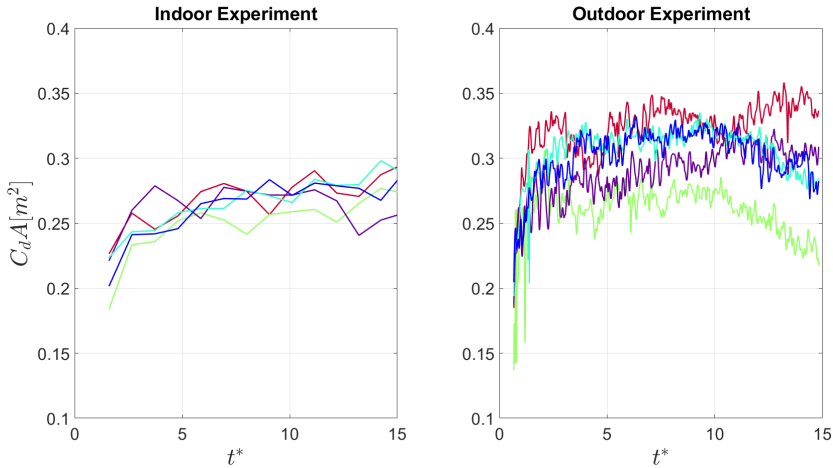


Figure 4.11: Instantaneous drag area measurements with the cyclist in upright posture.

For $t^* \leq 5$, the drag area computed via Equation 4.2 is underestimated as the contribution of the static pressure in the measurement plane is neglected. In case of the outdoor experiment, a $C_d A$ plateau persists until approximately $t^* \leq 10$, when a sudden drop in the drag area occurs. This can be related to part of the wake moving out of the measurement domain in several runs. In the outdoor experiment the external atmospheric conditions and a narrower field of view cause the problem. Moreover, the outdoor experiment generally exhibits larger fluctuations, especially in the near wake, which indicate a poorer control and repeatability of experimental conditions.

The comparison between the two ensemble-average drag areas of the two distinct postures of the athlete is shown in Figure 4.12 to illustrate the overall sensitivity of the Ring of Fire system to macroscopic variations of the drag area. Together with the ensemble-average $\overline{C_d A}$ (Equation 4.3), a shaded band wide $2\sigma_{\overline{C_d A}}$ represents the experimental uncertainty at 95% confidence level. Interestingly, although both the experiments were designed to obtain phase-locked average data, no clear cyclic trend depending on the crank angle is visible. This result differs from the findings of Crouch et al. (2014), who highlighted a 20% drag area variation with the crank angle, for a fixed t^* . This outcome shows that the wake diffusion and turbulent mixing is the main phenomenon affecting

the streamwise wake trend.

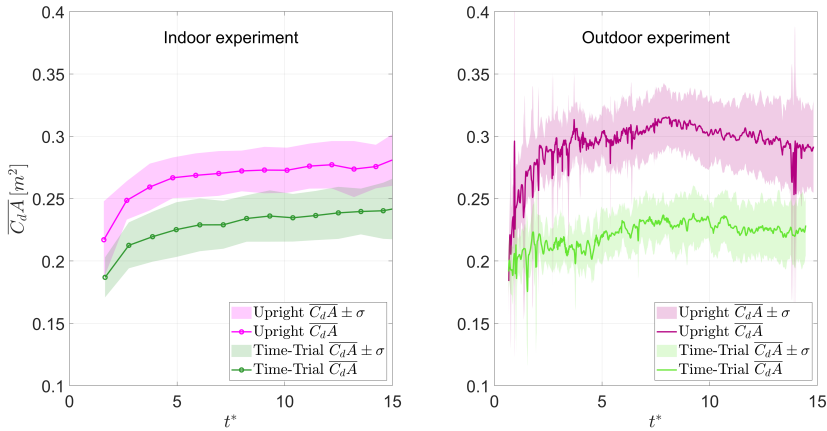


Figure 4.12: Ensemble average drag area measurements for time trial and upright postures.

TIME ENSEMBLE AVERAGE DRAG AREA

The time ensemble average drag areas (from Equation 4.4) for several configurations are summarized in Figure 4.13. The interval $6 \leq t^* \leq 9$ is considered, where systematic errors due to the pressure term and wake exit from the measurement region can be neglected.

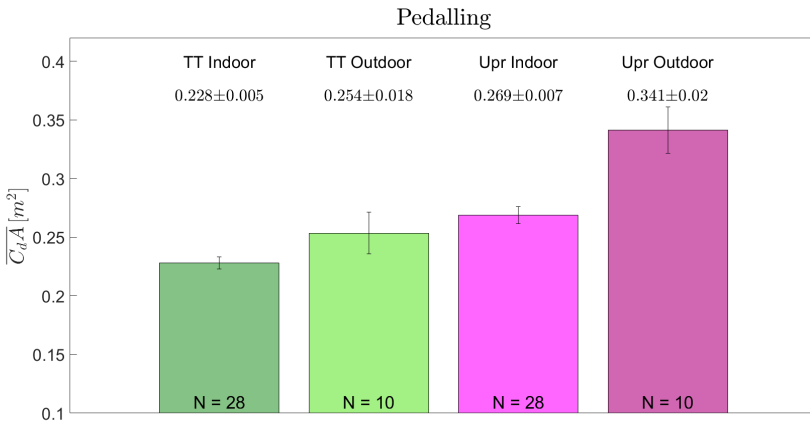


Figure 4.13: Time ensemble average drag area; uncertainty bars for 95% confidence interval. N indicates the number of cyclist's passages per case.

The drag area of the cyclist in the outdoor experiment is higher for both time-trial and upright postures. These results are in agreement with the wake contours in Figures 4.8 and 4.9, where a wider contour with higher peak momentum deficit is observed for

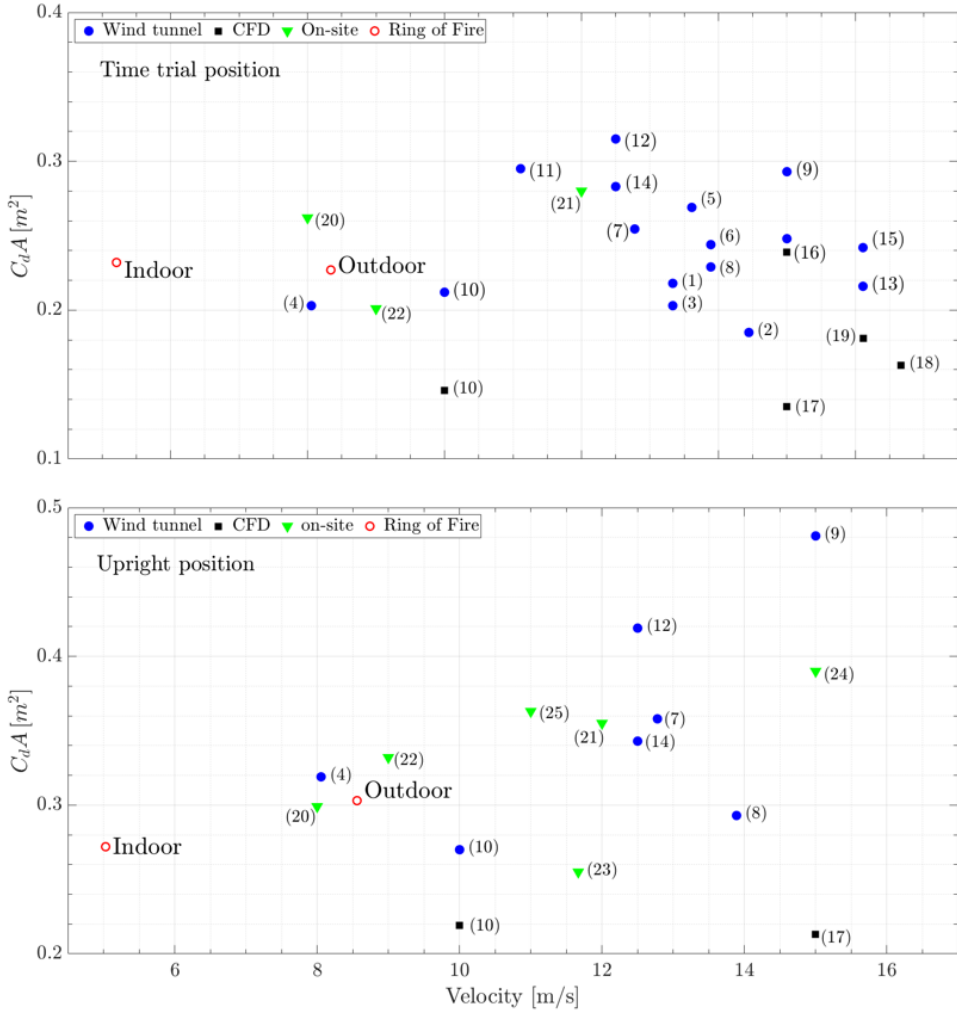


Figure 4.14: Comparison of drag area of a cyclist in time trial position (top) and in upright position (bottom) measured with different measurement techniques at different velocities. 1 Kyle (1991); 2 Hill (1993); 3 Broker and Kyle (1995); 4 Zdravkovich (1996); 5 Martin et al. (1998); 6 Padilla et al. (2000); 7 Jeukendrup and Martin (2001); 8 Gibertini and Grassi (2008); 9 García-López et al. (2008); 10 Defraeye et al. (2010a); 11 Underwood et al. (2011); 12 Chowdhury and Alam (2012); 13 Crouch et al. (2014); 14 Barry et al. (2015b); 15 Crouch et al. (2016); 16 Blocken et al. (2016); 17 Blocken et al. (2013); 18 Defraeye et al. (2014); 19 Griffith et al. (2014); 20 Grappe et al. (1997); 21 Candau et al. (1999); 22 Martin et al. (2006); 23 Capelli et al. (1993); 24 de Groot et al. (1995); 25 Lim et al. (2011).

the outdoor cyclist. A relative difference between 20 and 35% is measured between time-trial and upright postures, which is in agreement with literature. The bigger difference between the two experiments is observed when comparing the mean drag area in upright position, with the outdoor experiment returning a higher $\overline{C_dA}$ value. It is hypoth-

esized that this is due to a bigger difference in frontal area between the upright postures compared to the difference between the time-trial postures.

Finally, the current results are compared to the data collected from literature. The results of aerodynamic research in cycling exhibit a large scatter due to differences in riders, bicycle models, postures and garment and general experimental conditions. Figure 4.14 (top) and (bottom) compares drag areas versus velocity, measured in time-trial position and upright position, respectively, for different experiments and some computer simulations. Most measurements and simulations are conducted at racing velocity between 12 and 16 m/s. In our experiments, the limited space for accelerating and braking led to a lower velocity for the tests (5–8 m/s). Conversely, Grappe (2009) showed that in the range of 5–20 m/s, the drag area of a cyclist remains approximately constant. The results from the current experiments fall within this large cloud of data and correlate favourably with wind tunnel and on-site experiments. In contrast, results from CFD simulations yield systematically lower values of drag area.

4.5. CONCLUSIONS

Large-scale stereo-PIV measurements are conducted to determine the aerodynamic drag of a moving cyclist in indoor and outdoor on-site conditions using the control volume approach. The flow is measured in the wake of a cyclist moving at 5 m/s and 8 m/s for, respectively the indoor and outdoor experiments. Instantaneous as well as ensemble average streamwise velocity fields have been obtained. Despite the differences between the two experiments in the cyclist geometry, bike model and the cycling speed, the flow fields in the near wake of the riders compare well between both experiments and literature. The instantaneous and ensemble average aerodynamic drag is evaluated via a control volume approach along the wake behind the cyclist, taking into account the non-uniform flow conditions prior to the cyclist's passage. A clear distinction in upright vs. time-trial time ensemble average drag area ($\overline{C_d A}$) is found for both experiments, with the upright posture yielding higher drag area by about 20–35% with respect to the time-trial posture.



5

ASSESSMENT OF RING OF FIRE DRAG RESOLUTION

This chapter describes an experiment conducted in a spacious indoor facility, where aerodynamic drag estimates from the RoF are compared to a torque power meter installed on the bicycle. A sensitivity analysis assesses how the estimated drag is affected by the choice of PIV image-processing parameters or by the size of the cross-section considered in the control volume formulation.

This chapter has been published as: **Spoelstra A.**, Hirsch M., Sciacchitano A. and Scarano F. (2021) Uncertainty assessment of the Ring of Fire concept for on-site aerodynamic drag evaluation. *Measurement Science and Technology*, 32(4):044004.

5.1. INTRODUCTION

The Ring of Fire method, introduced in the previous chapter, showed great potential for applications in, e.g., the automotive industry and a wide range of speed sports. In future applications the RoF might be used to detect the effect of small modifications of posture or surface roughness on the aerodynamic drag (e.g. Brownlie et al., 2016); hence, knowledge of the drag resolution, or minimum detectable drag variation, is relevant. Terra et al. (2018) studied the drag resolution of a small-scale RoF system analysing the drag of a towed sphere in a narrow range of velocities, under the assumption of constant drag coefficient. The previous chapter already attempted drag estimates from a large-scale RoF; however, the comparison with literature data could not yield a conclusive assessment, given the large dispersion (approx. 50%) of the data due to many varying parameters, like rider posture, bikes geometries and testing conditions.

Although the RoF experiments discussed in Chapter 4 have returned wake measurements that agree satisfactorily with wind tunnel data, the uncertainty of the measured drag and its dependency upon experimental conditions and the image processing parameters have not yet been addressed. In particular, the errors arising from the set-up of the PIV measurement, the image recording and analysis, as well as the application of the control volume approach require a detailed scrutiny to support best practice of experiments.

In this chapter, linear error propagation is applied to determine how the uncertainty of the measured velocity field affects the drag calculation. Furthermore, the effect of the above-mentioned PIV parameters is investigated. The drag resolution of the RoF is studied here during large-scale indoor experiments by comparison with simultaneous power meter measurements, which is the most practiced method for aerodynamic drag measurements in cycling. Absolute and relative drag variations are introduced by different cyclist postures, as well as varying garments.

5.2. POWER METER DRAG EVALUATION TECHNIQUE

As was introduced in Section 2.2, a cyclist travelling on a flat, horizontal road imparts a propulsive force, $F_{cyclist}$, to sustain the motion contrasted by resistive forces, namely the aerodynamic drag, D_{aero} , external ($D_{rolling}$) and internal frictional forces ($D_{friction}$ for the drive-train and $D_{bearing}$ for the wheels). Any unbalance between these forces results in acceleration or deceleration of the cyclist (ma) (notice that here "a" indicates the acceleration in the direction of motion of the cyclist).

$$ma = F_{cyclist} - D_{rolling} - D_{friction} - D_{bearing} - D_{aero} \quad (5.1)$$

To extract the aerodynamic drag from the total drag value, the other terms are usually modelled by use of semi-empirical expressions. Following the methods described in

Martin et al. (1998) and Lukes et al. (2012), the aerodynamic drag can be obtained by:

$$D_{aero} = \underbrace{\eta_{Drivetrain}}_{\text{Drivetrain efficiency}} \cdot \underbrace{\frac{P_{cyclist}}{u_C}}_{\text{Total resistance}} - \underbrace{ma}_{\text{Inertia}} - \underbrace{C_{rr} \left(m \frac{u_C^2}{r_m} \cos \alpha + mg \sin \alpha \right)}_{\text{Rolling resistance}} - \underbrace{(91 + 8.7u_C) \cdot 10^{-3}}_{\text{Wheel bearing resistance}} \quad (5.2)$$

Where $\eta_{Drivetrain}$ is the drivetrain efficiency, $P_{cyclist}$ is the mechanical power generated by the cyclist, u_C is the cyclist velocity in quiescent air, C_{rr} is the rolling friction coefficient, m is the combined mass of rider and bike, g is the gravitational acceleration, r_m is the radius of curvature for the centre of mass trajectory and α is the cyclist's lateral lean angle relative to the horizon. The term $m \frac{u_C^2}{r_m} \cos \alpha$ accounts for the case where the cyclist moves along a curvilinear path of the radius of curvature r_m . When the cyclist rides along a straight path, the expression of the aerodynamic drag simplifies to:

$$D_{aero} = \underbrace{\eta_{Drivetrain}}_{\text{Drivetrain efficiency}} \cdot \underbrace{\frac{P_{cyclist}}{u_C}}_{\text{Total resistance}} - \underbrace{ma}_{\text{Inertia}} - \underbrace{C_{rr} mg}_{\text{Rolling resistance}} - \underbrace{(91 + 8.7u_C) \cdot 10^{-3}}_{\text{Wheel bearing resistance}} \quad (5.3)$$

The drivetrain efficiency varies between 96% and 98% for power outputs in the range 50–200 W (Kyle, 2001; Spicer et al., 2001). The rolling resistance coefficient is dependent on the tyre-pressure, -loading, -diameter and -temperature, as well as the surface properties of the ground and the steering conditions Burke (2003). Grappe et al. (1997) and Baldissera and Delprete (2016) regard the effect of speed on the rolling coefficient in cycling as negligible and therefore use a speed-invariant C_{rr} value.

5.3. EXPERIMENTAL SETUP AND PROCEDURES

5.3.1. TEST FACILITY AND SUBJECT

Experiments were conducted in a spacious indoor facility (Figure 5.1), 39 m wide and 77 m long, with a flat concrete surface. The cyclist rode loops of 190 m length in clockwise direction. The lap can be described as two semi-circles with a radius of 17.8 m, connected by two 39 m long straights. The start point of each lap is located at $x_l = 0$ m.

The rider was a professional athlete; his body mass and height were 79 kg and 187 cm, respectively, and his shoulder width was equal to 50 cm. He wore a short leg and short arm time trial skin suit from Team Sunweb (predecessor of Team DSM). Two helmet types were tested as shown in Figure 5.2. The rider wore over-shoes extending to half of their calves, as well as laser protection goggles.

A Team Sunweb time trial bike, model Trinity Advanced SL 2018 from Giant, was used during experiments. The bike was 1.7 m long and weighted 8.8 kg. The rear wheel was a

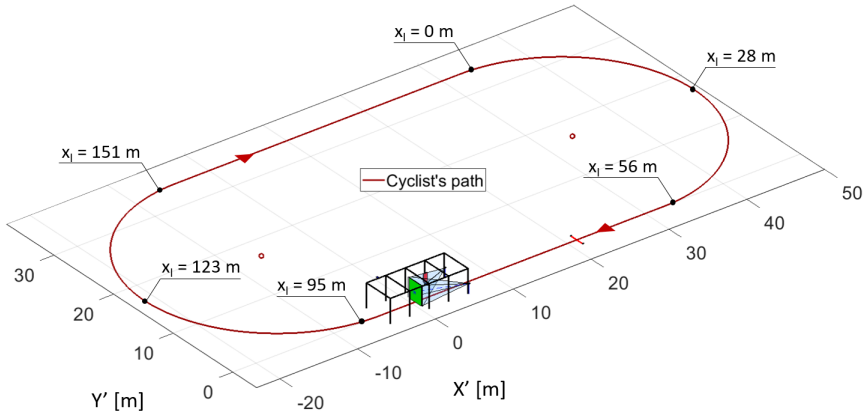


Figure 5.1: Isometric view of the testing facility and measurement apparatus layout.

5

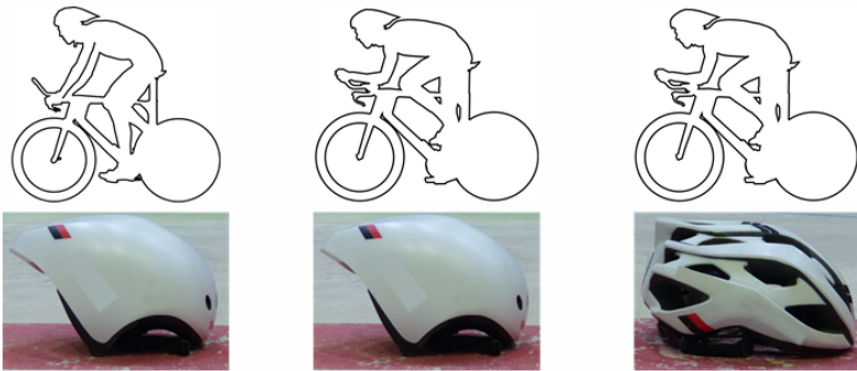


Figure 5.2: Riding configurations and helmets used. Upright position with aerodynamic helmet (left). Time trial position with aerodynamic helmet (middle). Time trial position with conventional road helmet (right).

PRO Tubular disc. The wheels mounted a Tubular Vittoria Corsa G 23 mm tyre set at 5 bar pressure. The estimated rolling resistance coefficient for this tire and conditions is $C_{rr} = 0.0045$ (Bierman, 2016). The cyclist's velocity was monitored with a magnetic sensor. A magnet was placed on the rear wheel of the bike and scanned by a magnetic sensor to retrieve information about displacement and velocity. The bike GPS device stored these data with a frequency of 1 Hz.

The cyclist maintained a constant speed of 8.3 m/s, with a normalised pedalling frequency (Crouch et al., 2014) of $k = \frac{2\pi r f}{u_C} = 0.15$, where r is the bike crank length, f the pedalling cadence and u_C the cyclist velocity. Three different configurations were examined (see Figure 5.2): 1) the cyclist in upright position with an aerodynamic helmet; 2) the cyclist in time trial position with the same helmet and 3) the cyclist in time trial position with a road helmet. For each configuration, measurements were collected during 40 loops to build an ensemble average estimate of the aerodynamic drag from the RoF and gather data from the power meter installed on the bicycle.

5.3.2. POWER METER MEASUREMENT SYSTEM

The bike was equipped with an SRM *Road Pro* crank-spider-based power meter, widely regarded as the benchmark for power meter devices (Duc et al., 2007; Passfield et al., 2017). The device recorded concurrent measurements of the athlete's mechanical power output, ground velocity and cadence in time. Before commencing trials, all units used during testing were calibrated against a zero torque reference, while pedals were stationary and unloaded as indicated by the manufacturer. For the calculation of ground velocity, the measured wheel circumference value of 2096 mm was used. Using an external torque dynamometer, the 95% confidence level uncertainty of the SRM power meter was estimated as 2% of the measured value over a range of 0 – 4096 W (Bertucci et al., 2005). After each complete crank revolution, power and cadence measurements were obtained. Data was recorded by the head unit at a rate of 1 Hz after being linearly interpolated in time (Underwood, 2012).

5.3.3. RING OF FIRE MEASUREMENT SYSTEM

Velocity measurements upstream and downstream of the cyclist were performed with a large-scale stereoscopic-PIV system with neutrally buoyant helium-filled soap bubbles (HFSB) of 0.3 mm diameter (Bosbach et al., 2009). The tracers were produced by a 200 nozzles rake installed inside the tunnel. A LaVision HFSB fluid supply unit (FSU) controlled soap, air and helium flow rates supplied to the seeding rake. A 10 m long tunnel structure of $4 \times 3 \text{ m}^2$ cross-section was built that confines the tracers around the measurement plane. The tunnel was built out of wooden panels integrated in an aluminium frame. Experiments were performed at a tracer concentration of approximately 13 bubbles/cm^3 . To quantify the tracing fidelity, the tracer's Stokes number, S_t , is considered, which is defined as the ratio of the tracer response time, τ_p , over the flow characteristic time, τ_f . Samimy and Lele (1991) showed that a particle is a faithful flow tracer when the condition $S_t < 0.1$ is satisfied. Based on previous studies from our group (Faleiros et al., 2019; Scarano et al., 2015), the helium-filled soap bubbles feature a tracer response time in the order of 10 to 100 μs , yielding a tracer's Stokes number in the order of 10^{-3} based on cyclist shoulder width and velocity. The light source was a Quantel Nd:YAG *Evergreen* 200 laser (2x200 mJ at 15Hz). A laser sheet thickness of 5 cm was selected to guarantee a sufficient number of tracer particles in each interrogation window, as well as to comply with the one-quarter rule (Raffel et al., 2018) when images were recorded with $\Delta t = 2 \text{ ms}$ pulse separation. Based on the study of Terra et al. (2019) and on the findings in the previous chapter, a maximum out-of-plane velocity of 5 m/s was expected in the cyclist's wake, thus requiring a laser sheet thickness of at least 4 cm to comply with the one-quarter rule. It should be noted that the selected laser sheet thickness is about $1/40^{\text{th}}$ of the in-plane dimensions of the measurement domain, which is consistent with many PIV experiments conducted at smaller scale (Raffel et al., 2018). Two LaVision Imager sCMOS cameras (2560×2160 pixels at 50 fps, 16 bit, pixel pitch 6.5 μm) were equipped with AF Nikkor 35mm objectives and daylight optical filters. A lens-tilt mechanism allowed complying with the Scheimpflug condition for in-focus imaging in stereoscopic conditions. The lens aperture was set to $f_{\#} = 8$ ensuring that particles in the illuminated region were imaged in focus. The cameras were placed 5.2 m upstream of the measurement plane at a relative angle of 35 degrees. The field of view captured

by both cameras was $2.4 \times 1.9 \text{ m}^2$, yielding a magnification factor $M = 0.0065$ and a digital imaging resolution of 1.01 px/mm . The measurements were synchronised with the transit of the athlete using a photo-detector (PHD) placed 20.5 m upstream of the measurement plane, which triggers the PIV system through a LaVision programmable time unit (PTU). Image pairs were acquired at a rate of 15 Hz with a pulse separation time of $\Delta t = 2 \text{ ms}$. A detailed sketch of the RoF setup is shown in Figure 5.3.

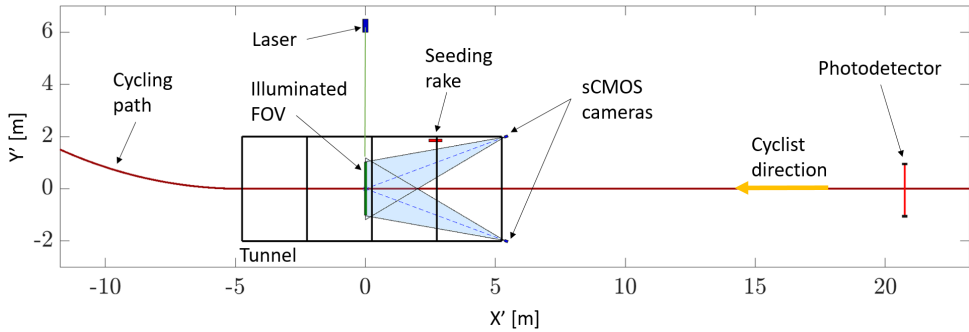


Figure 5.3: Schematic representation of the experimental layout of the RoF for the assessment of the drag resolution.

5.3.4. MEASUREMENT PROTOCOL

The PIV system and SRM power meter were calibrated at the beginning of each measurement day. Bubbles production was initiated about two minutes before the start of each run to achieve a uniform tracer distribution with sufficient concentration in the measurement domain. The cyclist started riding from the opposite side of the hall with respect to the measurement region, accelerating to the desired speed of 8 m/s . At each lap the image acquisition was triggered by the PHD, after which 40 image pairs are recorded and saved to a mass storage device before the next lap (typically 20 seconds). For all tests, all the doors of the hall were closed to minimise externally generated airflows. However, as the cyclist circled the hall, the induced air entrainment resulted in some systematic tailwind. The latter effect is unwanted, first as it tends to transport the seeding particles out of the RoF-tunnel, and secondly because it introduces larger fluctuations in the air motions prior to the passage of the cyclist. This effect was mitigated by carrying a blanket through the tunnel in the opposite direction after every passage. A movie recorded during the experimental campaign is available online (Spoelstra et al., 2021, electronic supplementary material).

5.4. DATA REDUCTION AND ANALYSIS TECHNIQUES

5.4.1. POWER METER

The power output and measured bike velocity of all runs are post-processed to obtain instantaneous drag area values. The power meter data are synchronised with the data recorded from the PIV measurements, including the time stamp of the laser illumination at the cyclist passage. Traces of velocity and power around the track are shown in Figure

5.4 for the individual upright measurements. Besides the individual traces of each loop, the mean value of all loops is included.

The mean velocity and mean power during the lap vary by approximately 5% and 45%, respectively. The loop-to-loop variations are up to 10% for the velocity and 70% for the power. Olds (2001) and Lukes et al. (2012) have discussed the relation between these variations and the movement of the centre of gravity (CG) towards the centre of the track during corners. Due to this movement, the CG travels at lower speed than the tyre contact point. Therefore, the comparison to the RoF is based on the power and velocity data recorded within the straight segment that includes the RoF measurement station (dotted box in Figure 5.4). Within this portion, the relative variation of mean velocity and power stays within 1% and 8% respectively.

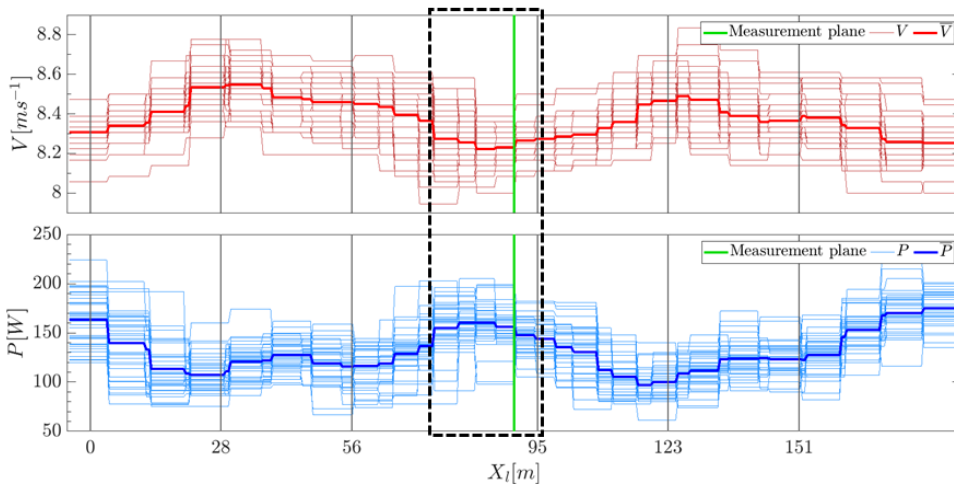


Figure 5.4: Instantaneous (thin lines) and phase-averaged (thick lines) velocity (top) and power (bottom) traces over the circuit. Data from the upright individual test. The RoF measurement plane location is indicated with a green vertical line.

An additional correction for the power meter is needed to account for the velocity of the air (u_{env}). The model as described by Equation 5.3 assumes surrounding air at rest to calculate drag from power and velocity. The relative velocity between cyclist and air is estimated by PIV measurements prior to the cyclist passage.

5.4.2. RING OF FIRE: PARTICLE IMAGE VELOCIMETRY

The recorded images are analysed with the LaVision *DaVis* 8 software. Background light is removed by subtracting an image taken in absence of seeding. Particle intensity is homogenised by a min/max-filter (Westerweel, 1993). The two-frame recordings are interrogated with iterative cross-correlation algorithm with window deformation (Scarano, 2001). The initial interrogation window (IW) size is at least equal to or larger than 1/4 of the particles image displacement (Adrian and Westerweel, 2011), whereas the final IW size is varied to study the effects of spatial resolution (section 5.5.3). Spurious vectors

identification is based on the universal outlier detection method proposed by Westerweel and Scarano (2005). To assess the out-of-plane velocity scales that the PIV system is able to resolve, the dynamic velocity range (DVR, Adrian, 1997) is determined as the ratio between the maximum velocity in the near wake of the cyclist (≈ 8 m/s) and the standard deviation of the velocity distribution in the quiescent flow prior to the cyclist's passage (≈ 0.03 m/s). This leads to a DVR of 266.

5.4.3. RING OF FIRE: CONTROL VOLUME APPROACH

WAKE IDENTIFICATION

The evaluation of the cyclist drag via the control volume approach requires the flow velocity measurements before and after the passage of the cyclist. In the ideal case when the cyclist is moving through quiescent air and the velocity measurements are noise-free, the drag estimate is not affected by the cross-sectional size of the control volume. However, in practice, environmental flow fluctuations and noise in the velocity measurements affect the estimated drag value and, based on Equation 4.1 and as discussed in more detail in section 5.5.1, their effect increases with increasing size of the cross-sectional areas S_i and S_o . Hence, a dedicated wake contouring approach was applied in the previous chapter, which isolates the cyclist's wake from the outer flow region. The wake was defined as $u_x^* \leq 0.95$ and then dilated by 2 vectors to include the shear layers. In this chapter an improved wake contouring approach is introduced. Several steps are performed to define the wake region behind the cyclist, which are presented in Figure 5.5. The wake is preliminary identified with the flow region where the velocity is below a certain fixed percentage, arbitrarily set to 30%, of the 5th percentile of the minimum velocity (maximum deficit) in the flow field. Instead of using the single minimum velocity value for this, using the percentile rather than the maximum velocity prevents the usage of outliers. Such region is then spatially dilated by a flat disk-shaped structuring element with a specified radius. The dilation length is chosen such that the entire wake and the shear layers are included in the region to be selected for the momentum analysis. The result is the control surface at the outlet S_o , recalling Equation 4.1. The procedure for wake contouring is summarised in Figure 5.5.

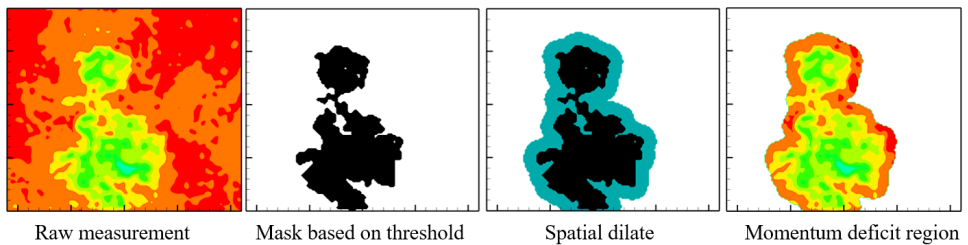


Figure 5.5: Flow schematic of wake contouring procedure. Explanatory movie available online (Spoelstra et al., 2021, electronic supplementary material).

MASS CONSERVATION

The control volume analysis is based on the hypothesis that the net mass flow is zero across the side and top boundaries of the domain (Anderson, 2011). Therefore, the shape

and size of the inlet plane S_i (Figure 4.1) must be adapted to ensure that the mass flow rate across S_i is equal to that across S_o . The wake contour at each measurement plane downstream (viz. after the passage) of the cyclist is adapted following the contouring approach discussed above. As initial contour upstream, the projected wake contour at the plane behind the cyclist is taken. The contour of the inlet plane is then narrowed or broadened one row of vectors at the time to reduce the mass flow difference from about 20% to below 0.1%. A graphical representation of this approach is presented in Figure 5.6.

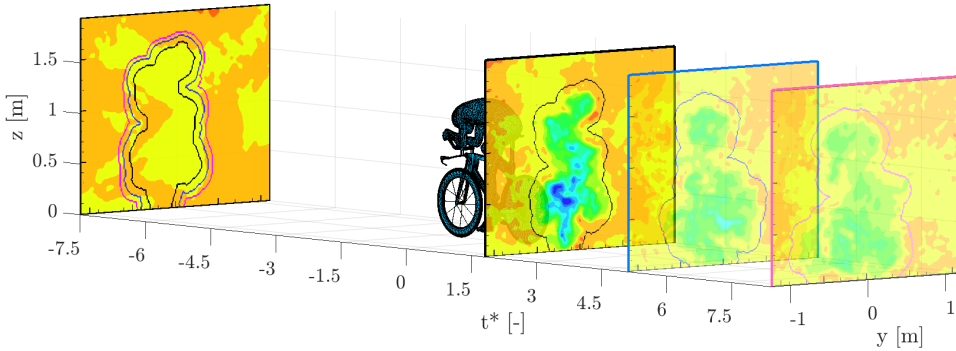


Figure 5.6: Contour adaptation based on the identification of the wake region (downstream plane) and compliance with the conservation of mass (upstream plane; contour colour corresponds to colour framing of the wake plane).

5.5. RESULTS AND DISCUSSION

5.5.1. *A priori* UNCERTAINTY ESTIMATION

Several error sources can affect the PIV measurements, from noise in the image recordings, to peak locking and through-plane particles motion (Sciacchitano, 2019). In this section, the uncertainty of the estimated drag is evaluated based on linear error propagation for the case where the velocity measurements are affected by random errors ϵ , whereas the systematic errors are negligible. The linear error propagation is performed in the wind tunnel frame of reference (frame of reference moving with the model). Furthermore, two simplifying assumptions are made: a) the upstream and downstream planes are sufficiently far from the object, so that the static pressure in both planes is undisturbed and equal to p_∞ ; b) there is a uniform inflow. Based on these assumptions, the aerodynamic drag of the cyclist simplifies to:

$$D = \rho \iint_A (u_\infty - u) \cdot u dA \quad (5.4)$$

Where u_∞ is the freestream velocity seen by the cyclist, and u is the streamwise velocity component behind the cyclist, in a cross-section of area A . Assuming that the latter velocity component is affected by a (spatially varying) random error ϵ :

$$u = u_{\text{true}} + \epsilon \quad (5.5)$$

being u_{true} the actual velocity in the wake of the cyclist, the expression of the drag becomes:

$$\begin{aligned} D &= \rho \iint_A (u_{\infty} - u_{\text{true}} - \epsilon) \cdot (u_{\text{true}} + \epsilon) dA \\ &= \rho \iint_A (u_{\infty} - u_{\text{true}}) \cdot u_{\text{true}} dA - \rho \iint_A \epsilon (u_{\text{true}} + \epsilon) dA \\ &= D_{\text{true}} - \rho \iint_A \epsilon (u_{\text{true}} + \epsilon) dA \end{aligned} \quad (5.6)$$

Where D_{true} is the true aerodynamic drag, in absence of measurement errors on the velocity. The expression of the time-averaged drag thus becomes:

$$\bar{D} = \bar{D}_{\text{true}} - \rho \iint_A \sigma_{\epsilon}^2 dA \quad (5.7)$$

Being $\sigma_{\epsilon}^2 = \overline{\epsilon^2}$ the variance of the velocity error, and having assumed that error and velocity are uncorrelated: $\overline{\epsilon \cdot u_{\text{true}}} = 0$. From Equation 5.7, it follows that a random error in the velocity field leads to an underestimation of the drag. The latter scales with the variance of the random error and with the area of integration. This result clarifies the importance of reducing the region of momentum analysis to the minimum, i.e. only encompassing the region of deficit. It is, however, of great importance that the domain captures the full wake for the entire duration of the measurement, otherwise an even larger underestimation of the drag may occur. For this reason, it is concluded that for the use of the Ring of Fire in an in-vivo environment, the best results in terms of accuracy of the drag evaluation are obtained after applying a dedicated wake contour as described in section 5.4.3.

In order to confirm the results from the *a-priori* uncertainty estimation, a Monte Carlo simulation is conducted on the flow field around a sphere with diameter $d = 10$ cm, obtained from a steady-state solver for incompressible, turbulent flow, using the SIMPLE algorithm with the standard k-Omega SST turbulence model (Wilcox, 2008). The simulation is performed in a volume of $20 \times 20 \times 25$ sphere diameters ($W \times H \times L$). The inlet velocity is set to 2 m/s, resulting in a Reynolds number of 1.4×10^4 . Errors with Gaussian distribution are imposed to the streamwise velocity component in the wake plane 7.5 diameters downstream of the sphere. The relative standard deviation of the random error in the streamwise velocity ($\frac{\sigma_{\epsilon}}{u_{\infty}}$) is varied in the range from 0 to 3.5 %. Consistently with Equation 5.7, Figure 5.7 confirms that the measured drag is underestimated in presence of measurement errors in the velocity, and that the measured drag decreases quadratically with increasing measurement errors in the velocity. Furthermore, the effect of the size of the cross-sectional area is investigated by cropping the original measurement region from all sides. Terra et al. (2018) already identified the issue of errors arising from

the size of the domain used for the momentum analysis; the authors showed that a reduction in cross-sectional area of the measurement domain could potentially lead to a reduction in the uncertainty of the measured drag by 10%. From the current analysis it is observed that, as expected, the systematic errors scale with the extent of the measurement domain considered for the drag estimation. If however, the domain is cropped so that part of the wake velocity deficit is cut off (area 4 in Figure 5.7), consequently, the drag value is underestimated. In the current case of the sphere, this led to an underestimation of 30% even in absence of any measurement errors in the velocity.

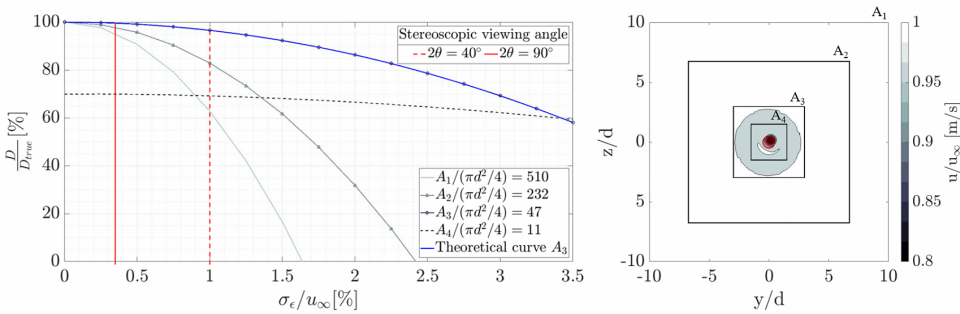


Figure 5.7: Uncertainty on drag area propagated from random error in the out-of-plane velocity for different wake plane sizes.

Assuming a typical uncertainty of the in-plane velocity components ($\sigma_{u_y}, \sigma_{u_z}$) measured by the Ring of Fire system equal to 0.1 pixel (Westerweel, 1993), the uncertainty of the out-of-plane velocity component can be estimated using Equation 5.8 (Prasad, 2000), and is equal to 1% and 0.4% of the cyclist's velocity for a stereoscopic angle θ of 20 and 45 degrees, respectively.

$$\sigma_{\epsilon} = \frac{\sigma_{u_{y,z}}}{\sqrt{2} \tan \theta} \quad (5.8)$$

Considering a ratio of measurement area over the frontal area of 47, then, based on the Monte Carlo simulation results, the measured drag is underestimated by 3.5% and 1% for stereoscopic angles of 20 and 45 degrees, respectively.

5.5.2. EFFECT OF MASS CONSERVATION

Due to the rider's circulation in the hall, an out-of-plane velocity of 2 m/s and a 0.4 m/s in-plane motion of the surrounding air were induced in the measurement plane. This led to a difference in the mass flow rate before and after passage of the cyclist of the order of 20%. The sensitivity of the drag estimate to the mass conservation is presented hereafter for the cyclist in time trial position with aerodynamic helmet. In the literature, the drag area of a cyclist in time trial position is reported to be between 0.2 – 0.3 m² (Crouch et al., 2017); the value measured via power meter measurements falls in that range, being 0.247 ± 0.008 m². Without imposing mass conservation, the drag obtained by the Ring of Fire is largely overestimated (0.447 ± 0.015 m²). Instead, when conservation of mass is imposed by applying the approach discussed in section 5.4.3, the estimated drag area

becomes equal to $0.211 \pm 0.008 \text{ m}^2$, showing much better agreement with the power meter measurement. This same trend is observed for the other two test cases, namely cyclist in time trial position with road helmet the cyclist in upright position: without mass conservation the value of the drag area is overestimated by approximately 100%, whereas when mass conservation is imposed, the estimated drag area agrees with the power meter measurements within 20%.

5.5.3. SENSITIVITY TO THE MEASUREMENT'S SPATIAL RESOLUTION

The spatial resolution of the PIV technique is an important parameter characterizing the overall measurement performance. The PIV cross-correlation analysis with a finite IW size is known to return a spatially filtered velocity field (Raffel et al., 2018); the amount of spatial filtering is expected to affect the accuracy of the drag estimate via the control volume approach. Although the simplest way to enhance the spatial resolution is to reduce the IW size, this is accomplished at the cost of increasing uncertainty (Sciacchitano et al., 2013). Hence, given the camera resolution, a compromise needs to be found between an image size large enough to capture the full wake and an interrogation window small enough to capture the small scale structures, while still providing an appropriate signal-to-noise ratio (SNR) to minimise the number of spurious velocity vectors as well as the uncertainty on the estimated drag. The effects of the IW size on the velocity fields and on the estimated drag are investigated for 30 runs of the baseline case (time trial posture + aerodynamic helmet). The size of the IW is varied from $8 \times 8 \text{ pixels}^2$ ($8 \times 8 \text{ mm}^2$) to $512 \times 512 \text{ pixels}^2$ ($512 \times 512 \text{ mm}^2$). The interrogation windows are weighted with a Gaussian function, and the overlap factor between adjacent windows is kept constant at 75% for all cases. The details of the spatial resolution analysis are summarized in table 5.1.

Table 5.1: Effect of the interrogation window size on the cross-correlation signal-to-noise ratio (SNR) and the estimated time ensemble average drag area ($\overline{C_d A}$).

IW size [mm ²]	Image density [particles/IW]	Vector pitch [mm]	Correlation \overline{SNR}	$\overline{C_d A}$ [m ²]	$\pm 95\%$ CI [m ²]
8×8	0.5 - 1	2	1.6	0.191	± 0.027
16×16	2 - 5	4	1.9	0.204	± 0.018
32×32	8 - 20	8	2.1	0.203	± 0.016
64×64	30 - 70	16	3.0	0.204	± 0.007
128×128	100 - 300	32	4.0	0.202	± 0.007
256×256	500 - 1200	64	6.0	0.198	± 0.008
512×512	2000 - 5000	128	8.0	0.183	± 0.016

The velocity fields reported in Figure 5.8 show that the use of a large interrogation window ($512 \times 512 \text{ mm}^2$) yields an underestimation of the peak entrainment velocity in the cyclist's wake. The latter is caused by spatial modulation whereby the cross-correlation estimation of the convex velocity distribution produces a less-than-average value; conversely, the use of a small interrogation window ($16 \times 16 \text{ mm}^2$) is not visibly affected by spatial modulation, but random errors occasionally appear due to the spurious occurrence of region with a low seeding concentration. The spatial modulation in the ve-

locity field has clear consequences on the drag area: over the first 5 m of the wake, the ensemble average drag area ($\overline{C_d A}$, red curve in Figure 5.8-right) for the $512 \times 512 \text{ mm}^2$ IW is lower than that computed with the 64×64 and $16 \times 16 \text{ mm}^2$ windows, especially in the near wake where the peak velocities are higher. The uncertainty on the measured drag area is approximately constant (0.016 m^2 , or 7% of the measured value) for interrogation window sizes between $16 \times 16 \text{ mm}^2$ and $128 \times 128 \text{ mm}^2$, which indicates the low sensitivity to the PIV spatial resolution in this range of interrogation window sizes. In contrast, higher uncertainty is retrieved for smaller interrogation windows ($8 \times 8 \text{ mm}^2$, uncertainty of 0.018 m^2 or $\approx 10\%$ of the measured value) due to the dramatic loss of the cross-correlation SNR which causes large measurement errors in the velocity fields, as well as for larger interrogation windows (exceeding $256 \times 256 \text{ mm}^2$) due to spatial modulation effects that cause a larger spread in drag area between the different runs. Hence, the size of the IW should be $0.05 c$ and $0.25 c$, where c is the characteristic length scale representative for the wake topology (shoulder width in this case). Choosing a larger IW leads to errors due to modulation; smaller IW size, on the other hand, leads to an increase in uncertainty due to random errors. This is, however, very dependent on experimental settings such as seeding density and pixel size of the camera. Based on the considerations above, the final interrogation window size value of $64 \times 64 \text{ mm}^2$ has been selected for the results presented in the remainder of this chapter as a compromise between high spatial resolution and low measurement errors in the velocity fields.

5.5.4. COMPARISON WITH POWER METER DRAG ESTIMATION

The time ensemble average drag ($\overline{\overline{C_d A}}$) of the three different test cases obtained from the Ring of Fire is compared to the average drag estimated from the power meter data. The measurements were acquired simultaneously, so the average results are obtained from the same set of samples for both the Ring of Fire and the power meter.

Firstly, the drag areas obtained from the RoF are considered. As was presented in section 4.2, in order to obtain the time ensemble average drag ($\overline{\overline{C_d A}}$) per test case, first the drag area of multiple passages needed to be ensemble-averaged to achieve a higher degree of statistical uncertainty. The wake is divided into two regions, namely the near and the far wake. In the near wake region, within five characteristic length scales from the cyclist, pressure effects cannot be disregarded according to Terra et al. (2017). Considering as characteristic length the shoulder width of the cyclist $c = 0.5 \text{ m}$, it follows that the static pressure in the flow affects the cyclist's drag estimate for the first 2.5 m downstream of the rider. Furthermore, the rider transited the laser sheet with no predefined crank-angle, meaning that the crank-angle at the laser sheet location varied from run to run. In the previous chapter we found that the information of the pedal position is maintained in the near wake, but not in the far wake due to turbulent mixing of the flow. Therefore, secondly, the ensemble average drag area is time averaged only over the measurements in the far wake. For the upright case, this led to a computed $\overline{\overline{C_d A}}$ of 0.257 m^2 , with a 95% confidence level uncertainty of 0.012 m^2 . For the time-trial position, the drag area reduces to 0.211 m^2 when the rider wears a time trial helmet, and to 0.226 m^2 when the road helmet is used. The uncertainties of these values are 0.008 m^2 and 0.010 m^2 , respectively, at 95% confidence level.

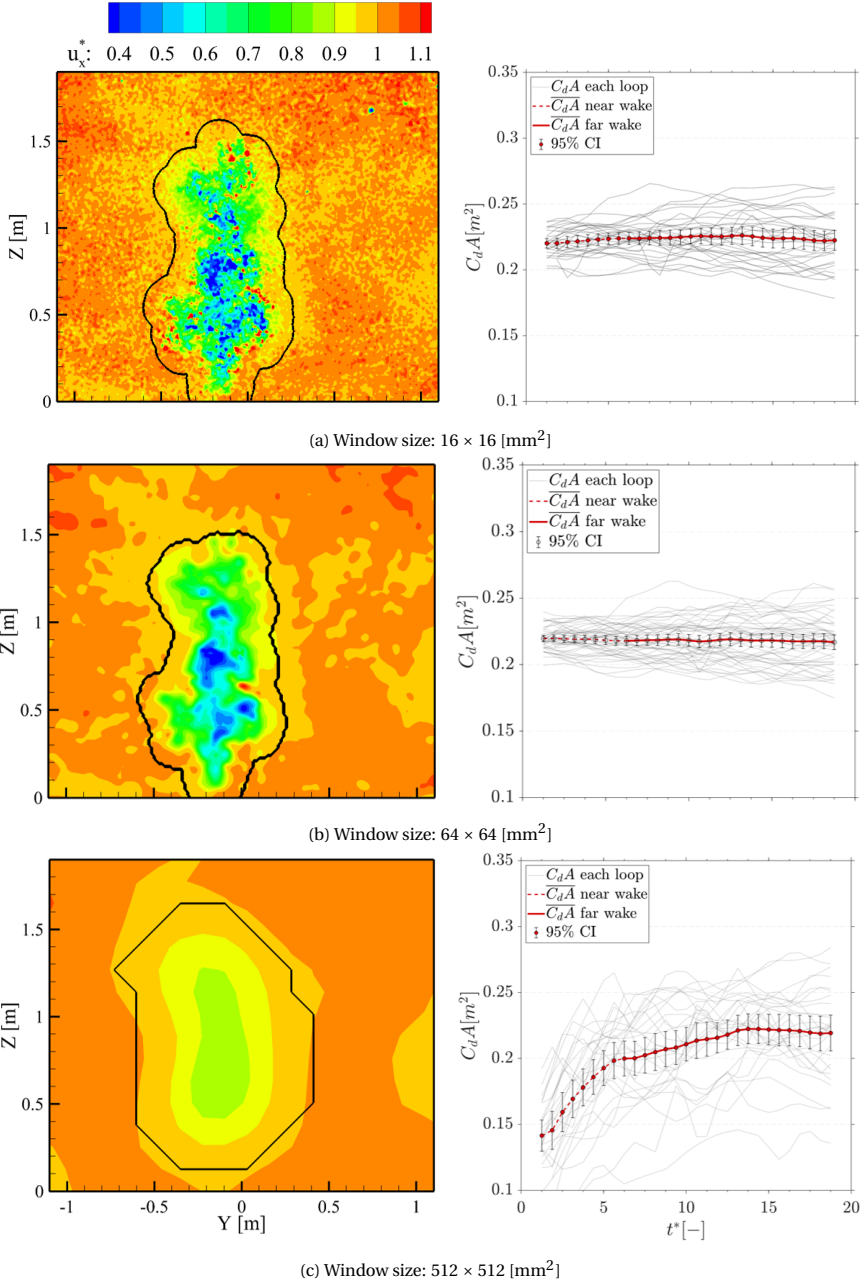


Figure 5.8: Dimensionless instantaneous streamwise velocity (u_x^*) at $t^* = 1$ (left) and streamwise $C_d A$ evolution in the wake (right). Data from the individual test in time trial position with aerodynamic helmet. The black lines represent the wake contours used for the drag analysis.

The average drag areas per test cases computed from the power meter data follow the methodology and processing steps explained in sections 5.2 and 5.4.1. The final values are presented in Figure 5.9 together with the above mentioned values from the RoF.

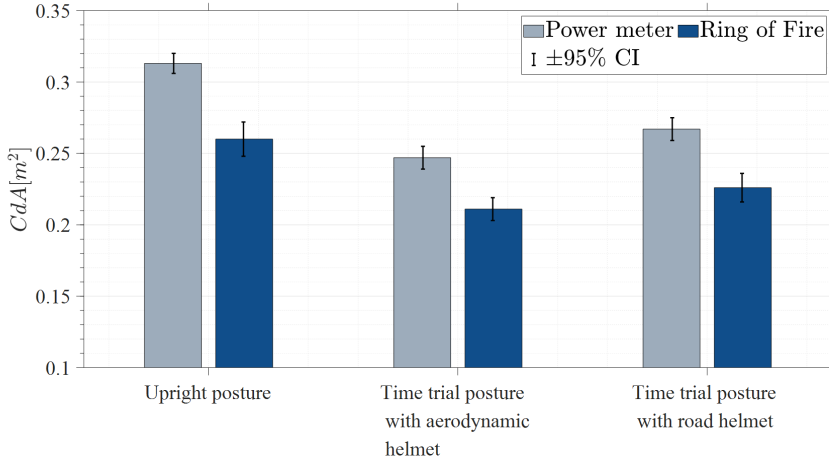


Figure 5.9: Comparison between the average drag area from the RoF and Power meter for the different configurations; uncertainty bars for 95% confidence interval.

The results in Figure 5.9 can be analysed in two different ways, namely by assessing the relative difference of the measurement techniques between each test condition, or by evaluating the absolute values of the predicted drag area. Regarding the absolute values, it is observed that the power meter approach on average overestimates the drag by 20% compared to the RoF. Additionally, the drag values obtained with the two techniques do not agree within the respective uncertainty bands. These disagreements can be ascribed to systematic errors in both the RoF approach, as described in section 5.5.1, and in the power meter measurements due to the simplified power meter model (e.g. flat road) and of the uncertainty in the model constants (e.g. rolling resistance coefficient), as discussed in section 5.2. While the latter error sources affect the absolute drag estimates obtained with the power meter, they cancel out when considering relative drag variations. Therefore, considering the relative performance, the trends of the power meter and the Ring of Fire measurements show good agreement, as a large-scale drag increase from time-trial to upright position is obtained. While the Ring of Fire predicts an increase in drag area of 0.049 m^2 (23%), the power meter results increase by 0.066 m^2 (27%). Between the two helmet types, a small-scale increase of 0.015 m^2 (7%) can be extracted from the Ring of Fire measurements, compared to a delta of 0.020 m^2 (8%) for the power meter approach.

5.6. CONCLUSIONS

In this chapter, large-scale stereo-PIV measurements are conducted to determine the aerodynamic drag of a moving cyclist using the control volume approach. The flow is

measured in the wake of a cyclist moving at 8.3 m/s. The single-passage and multi-passage average aerodynamic drag is evaluated via a control volume approach along the wake behind the cyclist, accounting for the non-uniform flow conditions prior to the cyclist's passage. A sensitivity analysis takes into account key parameters of the PIV technique, namely the interrogation window size and the control volume formulation, specifically determining the boundaries of the control volume. It is found that applying a dedicated wake contour and imposing the conservation of mass results in the most accurate drag measurements. Furthermore, the IW size should be within $0.05 c$ and $0.25 c$, where c is the characteristic length scale representative for the wake topology. Finally, the drag values obtained with the RoF are compared against the drag estimates from simultaneously acquired power meter data. To assess the agreement between the two approaches in different regimes, three individual tests are performed where small drag variations due to different helmets as well as large drag variations due to different cyclist postures are produced. Regardless of the underlying input parameters in the power meter model, both small- and large scale deltas are well captured by both the Ring of Fire technique and the power meter approach and agree with available literature values (Barry et al., 2015a; Blair et al., 2009; Spoelstra et al., 2019). The uncertainty on the average drag measurements from the RoF is within 5%. Although such value is considered rather coarse when compared with state-of-the-art force balance measurements conducted in a wind tunnel, it shows great potential for a range of other applications (drones, cars, trains, birds, ...) due to the possibility to determine the aerodynamic drag in-field rather than in the lab environment and simultaneously obtain flow visualization.

III

APPLICATIONS



6

DRAFTING IN CYCLING

Now the assessment of the RoF is made, the next step is to explore the use of it for real-life applications, which is done in the next chapters. In particular, this chapter describes an experiment that investigate the aerodynamic interactions between two cyclists in tandem configuration with changing lateral and longitudinal separations. The RoF is used to assess both the aerodynamic drag reduction of the trailing cyclist and the flow field interactions between the cyclists, at a few distinct separations between both. The gathered data is used to fit a mathematical model that predicts the drag of the trailing cyclist, depending on his or her position relative to the leading cyclist.

This chapter has been published as: **Spoelstra A.**, Sciacchitano A., Scarano F and Mahalingesh N. (2021) On-site drag analysis of drafting cyclists. *Journal of Wind Engineering and Industrial Aerodynamics* 219 104797.

6.1. INTRODUCTION

In cycling jargon, drafting is a riding technique whereby a cyclist closely follows the preceding athlete, thereby substantially reducing the aerodynamic drag (Barry et al., 2015b; Blocken et al., 2018; Broker et al., 1999). A detailed literature review on drafting in cycling was presented in Section 2.5. The salient aspects from a selection of the studies presented there are summarized in Figure 6.1, which indicates a drag reduction inversely proportional to both longitudinal separation and lateral offset. However, a striking dispersion of the drag values as well as its decay rate, especially with longitudinal separation, is remarked.

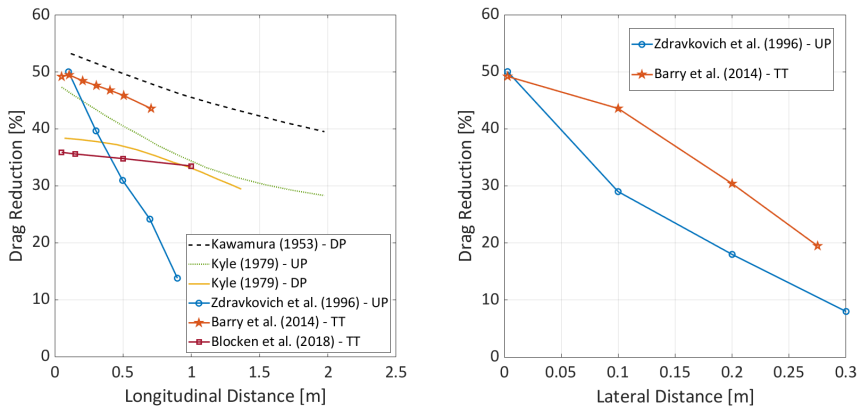


Figure 6.1: Overview of variations of trailing cyclist drag reduction by longitudinal and lateral offset. Data covers different cycling postures: Time trial (TT), upright (UP) and dropped (DP). (Note: Effect of longitudinal distance taken at zero lateral offset. Effect of lateral distance taken at 0.1 m longitudinal separation).

To the best of the authors' knowledge, all research up to now has dealt with discrete measurement points in the drafting region. Olds (1998) proposed a mathematical formula to take into account the drag reduction of a drafting cyclist riding in-line with the leading cyclist. However, there has not yet been an attempt to model the drafting phenomenon mathematically in order to get a map that predicts the drafting effect at any given location. Moreover, it is clear that all of the current state-of-the-art techniques for investigating cycling aerodynamics (wind tunnel, CFD and track measurements) have drawbacks when it comes to investigating the drafting effect in a realistic, but still controllable environment.

In the previous chapters the Ring of Fire was already shown to provide the aerodynamic drag of an individual cyclist during sport action and returned a quantitative visualization of the flow field in the wake. Thanks to the ability to measure the flow fields in the wake of both cyclists, as well as having a better monitoring of the posture and the relative distances between riders, the RoF is in principle suitable for the investigation of the aerodynamics of a group of riders.

The aim in this chapter is to apply the RoF for drafting aerodynamics in cycling and provide insights into the flow field interactions between both cyclists. Furthermore, based on the wake development of an individual cyclist, a mathematical model is intro-

duced to predict the drag of the trailing cyclist depending on his or her position relative to the leading cyclist.

6.2. ADAPTATION OF THE METHODOLOGY

The underlying principles for drag evaluation through the Ring of Fire have been laid down in Section 4.2. The instantaneous drag force $D(t)$ is evaluated by invoking the conservation of momentum expressed in a control volume around a transiting cyclist. The cyclist is assumed to move at constant speed u_C with respect to the laboratory frame of reference. In the case of an individual cyclist, the small and random air motions in the environment prior to the passage may be denoted as u_{env} . After the passage, the air is accelerated in the same direction as the cyclist, whose wake features a velocity field denoted as u_{wake} . In the case of two cyclists in tandem configuration, when the flow field in between the objects is also of interest, the environmental velocity field is denoted as u_1 , the velocity field in between as u_2 , and the velocity in the wake of the group as u_3 . The drag of a group of cyclists can be determined by including the whole group within the control volume (Figure 6.2). When expressing velocity and momentum in the cyclists' frame of reference, the following expression returns the instantaneous drag of the group:

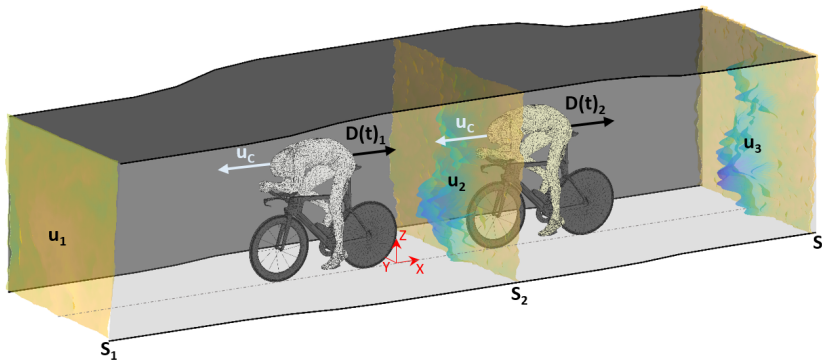


Figure 6.2: Schematic view of the domain of interest, with two cyclists. S_1 and S_3 are the upstream and downstream sides of the domain. A colour-coded surface illustrates the air velocity before, in between and after the passage of the group.

$$D(t) = \underbrace{\rho \iint_{S_1} (u_1 - u_C)^2 dS - \rho \iint_{S_3} (u_3 - u_C)^2 dS}_{\text{Momentum term}} + \underbrace{\iint_{S_1} p_1 dS - \iint_{S_3} p_3 dS}_{\text{Pressure term}} \quad (6.1)$$

where ρ is the air density. This expression is valid at the condition that the mass flow is conserved across surfaces S_1 and S_3 . Also the drag of each individual cyclist can be calculated in the same way, namely by conservation of momentum across surfaces S_1 and S_2 for the leading cyclist, and surfaces S_2 and S_3 for the drafting one. In comparison

to measurements for individual cyclists, where the trailing end of the control volume can be chosen far enough, such that the pressure term in equation 6.1 can be neglected, the pressure term needs to be considered between cyclists for an accurate drag evaluation Terra et al. (2017).

6.3. EXPERIMENTAL SETUP AND PROCEDURES

6.3.1. FACILITY AND EXPERIMENTAL CONDITIONS

Measurements are conducted at the Tom Dumoulin bike park of Sittard-Geleen in the Netherlands. The facility is built on a 6-hectare area and hosts a total of 3.2 km track with paths that vary by surface type, differences in altitude, and challenging turns. Experiments are conducted on the 1.1 km, flat, oval outer lap. Three male U23 cyclists were recruited. A summary of their anthropometric characteristics and individual drag area ($C_d A_0$) and its confidence interval (CI) is reported in Table 6.1. The cyclists are named from A to C. The projected frontal area was determined from photographs taken from 5 m in front of the cyclist, with a reference area standing next to him. The frontal area was then determined as the average from multiple photographs at 4 different leg positions. As reported by Crouch et al. (2014) there are differences in frontal area of 2% between different leg positions. Therefore, the uncertainty on the projected frontal area is assumed to be 2%.

6

Table 6.1: Subjects' anthropometric characteristics and individual drag area (m^2).

Subject	Height [m]	Mass [kg]	Projected frontal area [m^2]	Drag area ($C_d A_0$) \pm 95% CI [m^2]	Number of passages
A	1.75	61	0.360	0.205 ± 0.012	7
B	1.85	70	0.337	0.182 ± 0.004	10
C	1.92	69	0.316	0.204 ± 0.005	11

The cyclists were required to perform a series of individual tests as well as 4 different drafting tests, varying their order in the group. Figure 6.3 shows one such passage of a drafting group (data not included here) through the Ring of Fire. All tests were performed at a nominal riding speed of 45 km/h; when drafting, the riders were asked to maintain a wheel-to-wheel spacing of 0.3 m and to stay in-line with the lead rider. In practice, the longitudinal displacement of the drafters varied between 0.32 m and 0.85 m and the lateral displacement varied between ± 0.20 m among different runs. The subjects were required to wear the same clothing and to use the same equipment during all testing sessions. In addition to the skin suit and helmet, the riders wore laser safety goggles for protection against the PIV laser light. For each configuration, the experiment was repeated 10 times. For all trials, the subjects started pedalling 300 m before the measurement region, accelerated to the prescribed velocity of 45 km/h and maintained such velocity up to about 100 m after the measurement region, where they ceased pedalling. The riders were also required to maintain a constant racing posture (time-trial posture) within and across all trials.

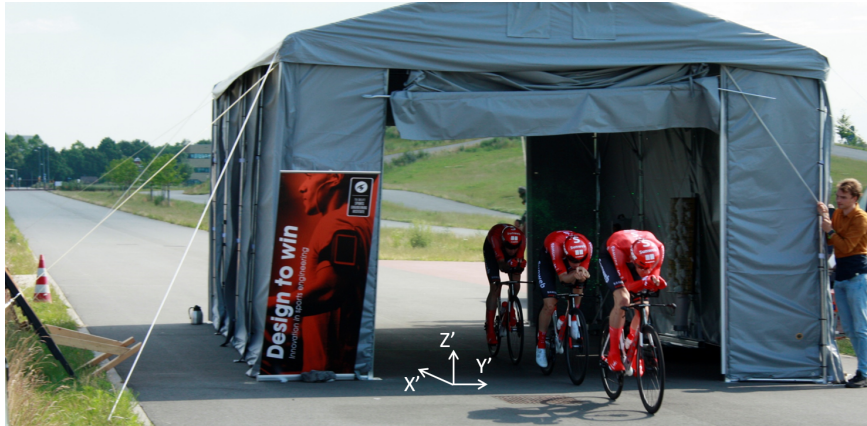


Figure 6.3: Photograph of a three-cyclists group transiting across the Ring of Fire.

6.3.2. PIV SYSTEM

The velocity distribution upstream and in the wake of the cyclists was obtained by large-scale stereoscopic-PIV. Neutrally buoyant helium-filled soap bubbles (HFSB) with an average diameter between 0.3 and 0.4 mm were used as flow tracers (Scarano et al., 2015), providing sufficient light scattering to visualize a field of view (FOV) of the order of 4 m². A tunnel of 8×5×3 m³ in X, Y, and Z direction (see Figure 6.3) was used to confine the bubbles within the measurement volume. The tunnel had an open in- and outlet to allow the rider to transit and was equipped with optical access on one side for illumination purposes. The tracers were introduced in the measurement region by a rake with 200 nozzles positioned 1 m upstream of the measurement plane and aside the cyclists track. A Quantronix Darwin Duo Nd:YAG laser provided pulsed illumination (pulse energy of 2×25 mJ at 1 kHz rate). The laser beam was shaped into a 50 mm thick sheet by means of laser optics and light stops. The field of view was imaged by two Photron Fast CAM SA1 cameras (CMOS, 1024×1024 pixels, 12 bits) equipped with 35 mm objectives at f/2.8. Images were acquired at 0.5 kHz and 1 kHz for the individual and drafting measurements, respectively. The cameras were placed 4 m upstream of the measurement plane with an angular separation of 95 degrees, imaging a field of view of 1.8×1.8 m². The resulting magnification factor was 0.011 and the digital image resolution 0.57 px/mm. The tracers particles were held in the measurement domain by closing entrance and exit gates of the tunnel before the passage of the cyclist, accumulating for about two minutes. The velocity and position of the cyclists were determined from the stereo-PIV recordings. The resulting uncertainties are 0.1 m/s and 2 cm, respectively. A detailed sketch of the top view of the experimental setup is given in Figure 6.4.

6.3.3. DATA REDUCTION

The recorded images were processed with the LaVision DaVis 8.4 software by means of cross-correlation analysis. The final interrogation window size is chosen to be 24×24 pixels and the overlap factor is set to 75%. The evaluation of the cyclist drag via the control

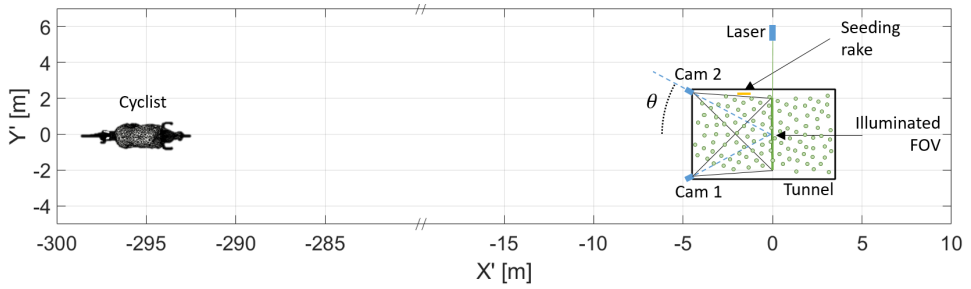


Figure 6.4: Schematic view of the experimental setup for the drafting experiment.

volume approach requires that mass conservation at the inflow and outflow of the domain is accurately satisfied, assuming there is no momentum transfer through the side faces of the domain. This assumption, however, is not possible in the current measurements as the velocity along the sides of the domain is not known. A way to mitigate the errors associated with approximate mass conservation is reducing the momentum analysis to the region where most deficit has occurred. This is done by means of a dedicated wake contouring approach that is discussed in Chapter 5. Furthermore, the pressure field is reconstructed by solving the pressure Poisson equation (PPE) (van Oudheusden, 2013). Neumann boundary conditions are applied at the boundaries and the resulting pressure distribution is scaled with the measured quiescent air pressure as reference.

The time ensemble average drag area ($\overline{C_d A}$) for the individual cyclists is computed with Equation 4.4 for each cyclist. The final number of passages used for ensemble-averaging after discarding the faulty ones is presented in Table 6.1. For every passage of the cyclists, only the first 2.5 meters in the wake are considered for drag calculation. On the basis of the evaluation of drag area from wake flow measurements at different distances from the cyclist, it is concluded that the windy conditions in the outdoor test facility cause the aerodynamic drag measurements beyond 2.5 m (0.2 s after the cyclist has passed) to become unreliable. Furthermore, the riders transited the laser sheet with no predefined crank-angle, meaning that the crank-angle at the laser sheet location varied from run to run.

The drafting separation is defined as the distance between the rear wheel of the leading cyclist and the front wheel of the drafting one. The drag reduction coefficient DR for the trailing cyclist is defined as:

$$DR = \frac{C_d A_0 - C_d A_{draft}}{C_d A_0} \times 100 \quad (6.2)$$

and expresses the drag area reduction experienced by the trailing cyclist compared to riding alone. Accordingly we introduce the drag area $C_d A_0$ of the rider alone and $C_d A_{draft}$ for the drafting cyclist.

6.4. RESULTS AND DISCUSSION

In order to analyze the drafting effect in the tandem configuration, first the three single-rider tests are analyzed before the drafting scenarios are considered. In addition to the individual drag area of each of the cyclists, also the development of the time-average wake of an individual cyclist is evaluated. Next, the drafting configurations are studied. Firstly, three distinct runs are chosen for the investigation of the flow fields, after which the measured drag reductions are reported.

6.4.1. EFFECT OF THE HUMAN FACTOR

On track measurements with real cyclists are affected by variations of the cyclists' speeds, positions and drafting distances, and environmental conditions, which all contribute to the measurement uncertainty. In wind tunnel measurements or CFD simulations these parameters are strictly controlled and any uncertainty arising from them is kept low. The drafting experiment with the Ring of Fire uses human subjects in a real world environment, which makes control of these parameters very hard. The impact of the human factor on the uncertainty of the measurement also gives a good indication on the uncertainty to be expected during racing performance.

An example of the effect of such a human factor is shown in Figure 6.5, where cyclist A is shown to use different head postures in different passages. It was found that adopting a “head down” posture exposed more of the helmet tail to the freestream, while the “head up” posture tucked the helmet tail behind the head, shielding it from the freestream. This difference in head posture resulted in a maximum difference of 0.0158 m^2 in drag area for the two runs shown in Figure 6.5, which translates to 7.7% of the mean drag area, thus explaining the higher statistical spread of $C_d A_0$ for cyclist A (Table 6.1).

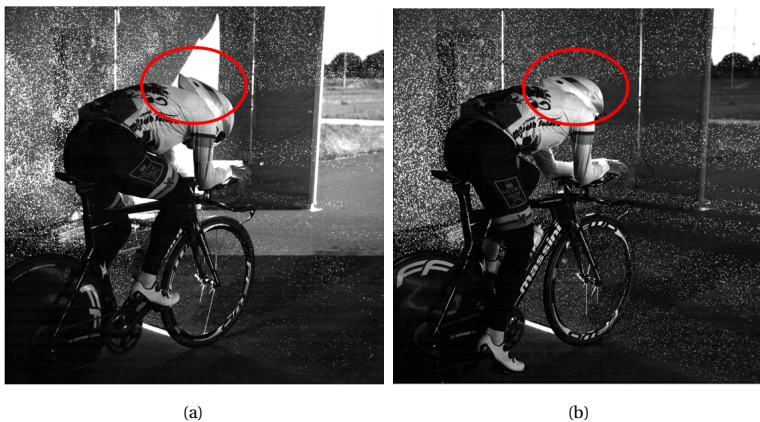


Figure 6.5: Variations of head posture between different cyclist passages. (a) Head down position vs. (b) head up position.

Another parameter affected by the human factor was the drafting location. Despite the instruction given to the riders to maintain an aligned configuration at 0.3 m longitudinal distance, the analysis of the recorded images showed that there is a large variation

in drafting distances between different runs from the same configuration as well as between different configurations. The average and standard deviation of drafting distances maintained by each cyclist while trailing another cyclist are obtained from 10 runs and are presented in Table 6.2.

Table 6.2: Mean longitudinal and lateral separations for each cyclist in trailing position and the corresponding standard deviation obtained from 10 runs.

Configuration	$\overline{\Delta X}_{meas} \pm \sigma$ [cm]	$\overline{\Delta Y}_{meas} \pm \sigma$ [cm]
C - A	68 ± 8	6 ± 8
C - B	32 ± 4	2 ± 5
A - C	50 ± 7	5 ± 6
B - A	69 ± 10	7 ± 9

On average, it is noticed that cyclist B performed best in maintaining a constant distance of 0.3 m from the leading rider, while cyclist A has twice the average longitudinal drafting distance. Also in terms of the lateral separation cyclist A is outperformed by the other cyclists. Thus ranking the three subjects from skilled to less skilled in drafting, subject B is the most skilled and A the least.

6.4.2. SINGLE CYCLIST

For each of the three cyclists, the planar cross sections (at $X = 0.5$ m) of the ensemble-average velocity and pressure coefficient in the wake are given in Figure 6.6 and Figure 6.8, respectively. In Figure 6.6, a high deficit region is observed at $Z < 0.5$ m, which is ascribed to the aerodynamic resistance from the rear wheel and the drive train. Such deficit is more pronounced as one approaches the rear wheel. A second important area of deficit is observed between $Z = 0.7$ m and $Z = 0.9$ m, which corresponds to the vortices shed from the inner thigh and lower hip of the cyclist (Crouch et al., 2014). Finally, the region of deficit at $Z = 1.2$ m corresponds to the upper body and head of the cyclist.

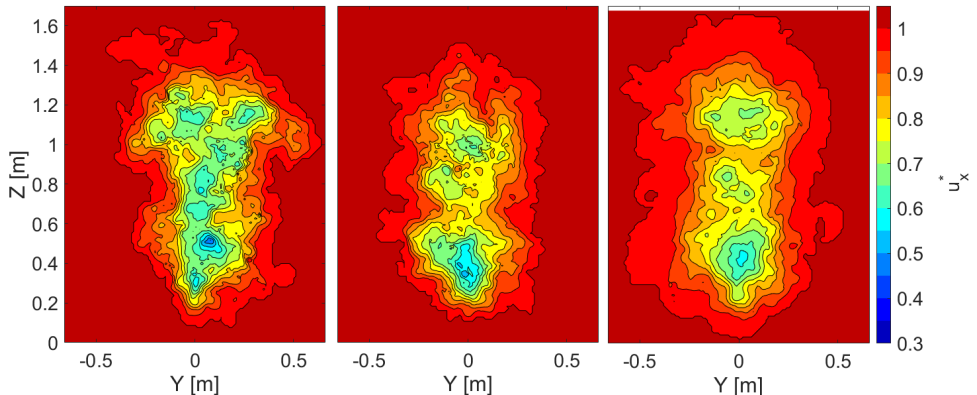


Figure 6.6: Ensemble-average velocity u_x^* at $X = 0.5$ m for cyclist A (left), B (middle) and C (right).

A detailed comparison of the ensemble-average wake region contours ($u_x^* = 0.9$) for

the three cyclists is illustrated in Figure 6.7. The wakes of cyclists B and C only differ in the upper part, consistent with their body size. Instead, the wake of cyclist A exhibits clear appendices indicating a wider position of the elbows/upper arms.

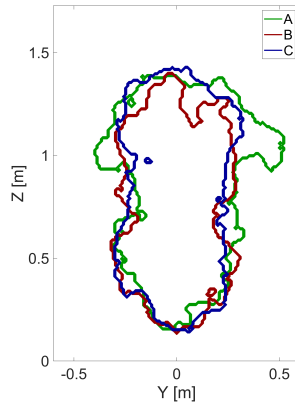


Figure 6.7: Comparison of isoline of the ensemble-average velocity u_x^* equal to 0.9 among the three cyclists ($X = 0.5$ m).

A comparison of the total pressure coefficient in the wake of the cyclists reveals that for all a low pressure is found in the lower half of the wake. Similar to the velocity fields, this is caused by the rear wheel and the drive train being closest to the measurement plane. For cyclist A, however, the low pressure is more spread out over the entire wake, which would indicate that the position of his upper body is less streamlined and thus acting more like a bluff body as compared to the other two cyclists. The similarity between velocity and total pressure here can be explained by the fact that the static pressure only accounts for roughly 10% of the total pressure and thus the total pressure is dominated by the dynamic pressure.

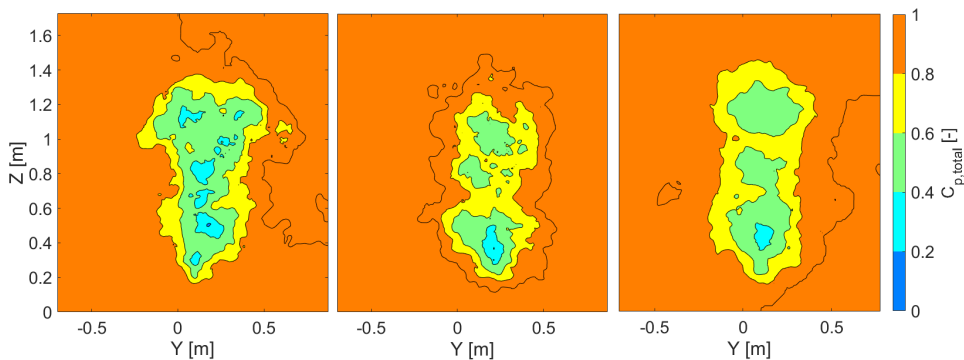


Figure 6.8: Comparison of ensemble-averaged total pressure coefficient at $X = 0.5$ m, for cyclist A (left), B (middle) and C (right).

The spatial evolution of the velocity field along the wake of cyclist C is shown in Figure 6.9. A deficit of 20% (10%) extends up to 6 m (beyond 10 m), indicating that drag benefits can be obtained from drafting even several meters behind the preceding cyclist. However, the high deficit region ($u_x^* < 0.6$) vanishes after 2 m in the wake. From the top view in Figure 6.9 one can appreciate the lateral spreading of the wake: at $X = 6$ m the velocity deficit exhibits approximately 1 m width. Comparatively the velocity distribution seems to spread less along the vertical direction. In particular, the flow downwash past the cyclist (indicating the presence of a mild upwards force) moves the center of the wake towards the road. These observations are consistent with those reported in Chapter 4, where a similar wake evolution was found.

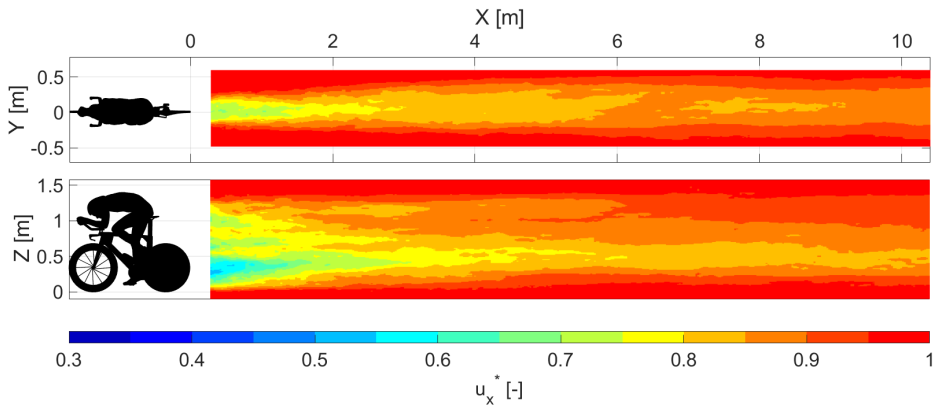


Figure 6.9: Top ($Z = 0.8$ m) and side view ($Y = 0$ m) of ensemble-averaged velocity past cyclist C.

The potential drag reduction by drafting is analyzed here observing the spatial evolution of the velocity past a single athlete. The average streamwise velocity ($\overline{u_x}$) versus distance as well as the rate of lateral wake expansion versus distance in the near wake are presented in Figure 6.10. The average streamwise velocity $\overline{u_x}$ is defined as the average velocity in the wake of the cyclist, where the wake is determined by the contouring approach discussed in 5.4.3. The lateral wake expansion is defined by the growth in the wake half-width y_w , which is evaluated as the distance from the maximum velocity to point where this velocity is half (Pope, 2000) in the XY-plane at $Z = 0.8$ m. In the near wake of the three cyclists the average streamwise velocity $\overline{u_x}$ decays with $\sim X^{-\frac{1}{3}}$ and their half-wake width y_w very slowly expands linearly with $\sim 0.04X$. These decay and expansion scales are represented by the gray dashed lines in Figure 6.10. Furthermore, as a reference, the scaling laws for an axisymmetric wake as reported by Pope (2000) are indicated by the gray dash-dotted lines. According to Pope (2000), the velocity decays as $X^{-\frac{2}{3}}$ and the wake half-width, y_w , expands as $0.1 \cdot X^{\frac{1}{3}}$.

Table 6.1 summarizes the ensemble-averaged drag area ($C_d A_0$), height, mass and projected frontal area measured for each cyclist participating in this experiment. As it can be observed, the projected frontal area is strongly dependent on the cyclist posture and as a result, it does not directly correlate with the athlete height or weight. The com-

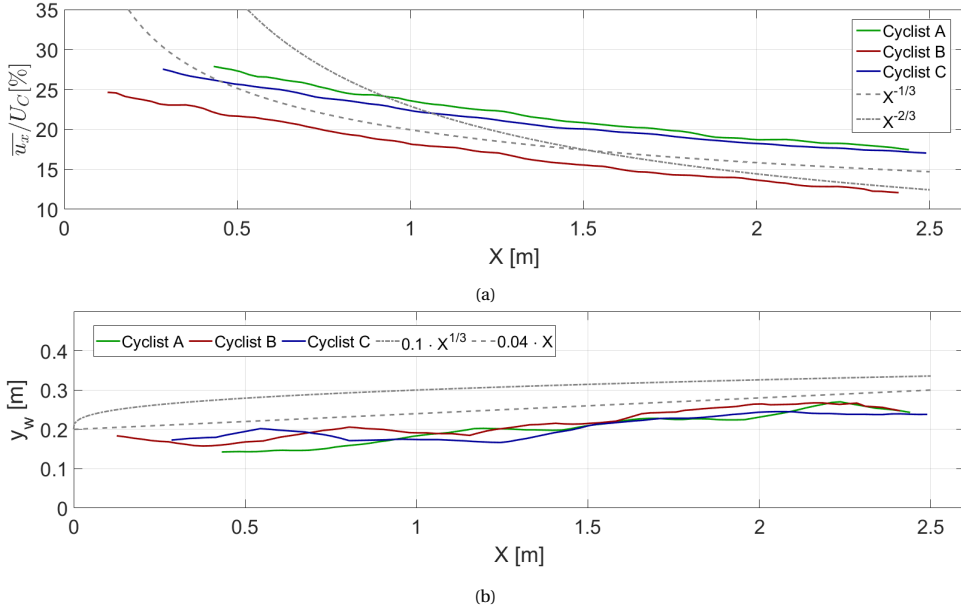


Figure 6.10: Average velocity decay and wake width. (a) The average streamwise velocity ($\overline{u_x}$) normalized by cyclist velocity (u_C) vs. distance in the wake for all three cyclists. (b) The average lateral wake expansion in the XY-plane at a height of $Z = 0.8$ m.

bination of frontal area and posture leads to a similar $C_d A_0$ value for cyclists A and C, whereas cyclist B exhibits a $C_d A_0$ about 10% smaller. The uncertainties of the drag area measurements are similar to those reported for previous RoF experiments, namely below 5% (Spoelstra et al., 2019).

6.4.3. TANDEM CONFIGURATION

FLOW FIELD ANALYSIS

Three runs are chosen for the investigation of the flow fields in the tandem configurations; one where both longitudinal and lateral separation are small, one where longitudinal separation is large but lateral separation is still small, and finally one where both longitudinal and lateral separation are large. Those runs are labelled as I, II and III in Figure 6.13, respectively. A summary of the separations for the three runs is presented in Table 6.3.

Table 6.3: Longitudinal and lateral separations for drafting runs I, II, III.

Configuration	Longitudinal separation	Later separation
	[m]	[m]
Run I (C - B)	0.35	0.01
Run II (B - A)	0.78	0.01
Run III (B - A)	0.85	0.18

The instantaneous velocity fields of the three runs are compared in Figure 6.11, with the first and second row corresponding to upstream and downstream of the trailing cyclist respectively. When comparing the inflow conditions of run I and II, it is observed that both trailing cyclists are fully submerged in the wake of the leading cyclist. Since the inflow at run II is further downstream of the leading cyclist, it was expected that the velocity deficit created by the lead cyclist was already partly recovered to freestream conditions.

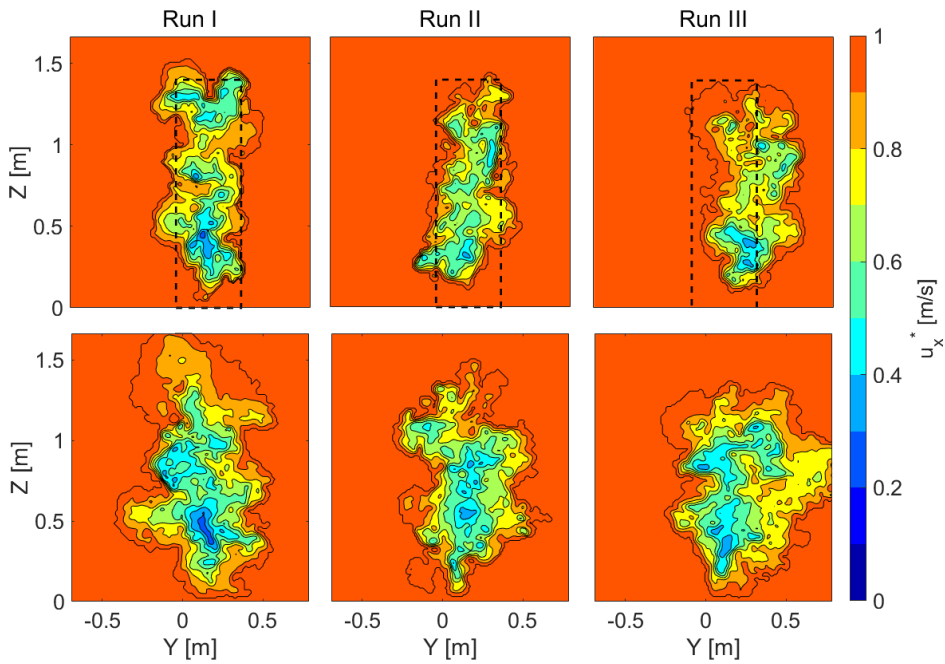


Figure 6.11: Instantaneous dimensionless filtered streamwise velocity (u_x^*) contours 0.1 m upstream of the trailing cyclist (top) and 0.5 m downstream of the trailing cyclist (bottom). The dashed rectangle indicates the location of the trailing cyclist relative to the wake of the leading cyclist.

When the longitudinal separation was similar, but the lateral separation was increased (run III compared to run II), the velocity deficit created by the lead cyclist was similar; however, because the trailing cyclist in run III was not fully submerged in the wake of the leading cyclist, on average he encountered a higher inflow velocity. This is confirmed in Figure 6.11.

The instantaneous velocity field in the wake of the trailing cyclist (bottom row of Figure 6.11) in all of the three cases shows a higher deficit than that of the ensemble-average velocity field in the wake of the isolated cyclist (Figure 6.6). With larger longitudinal separation (run II and run III), the velocity deficit more closely resembles the single cyclist due to reduction of the influence of the velocity components in the leader's wake. In terms of wake width it is observed that for run I and II, with null lateral separation, there is little difference w.r.t. the individual cyclist. When however the lateral separation is

increased (run III) the wake width significantly increases.

Under the assumption that the velocity deficit is small with respect to the cyclist velocity, using a simplified model, the drag of the cyclist is given by the difference in total pressure between upstream and downstream of the cyclist, times the wake area (Jones, 1936). Hence, a decrease of total pressure upstream of the rider, or an increase of total pressure downstream of the rider would result in lower drag. Therefore, the instantaneous total pressure coefficient upstream and downstream of the drafting cyclist is compared to the ensemble-average total pressure coefficient of the individual cyclists. In Figure 6.12, the total pressure coefficient is plotted at the same locations as the velocity fields in Figure 6.11. Similar observations can be made as were made for the velocity fields in Figure 6.11 in terms of changes w.r.t. the individual cyclist.

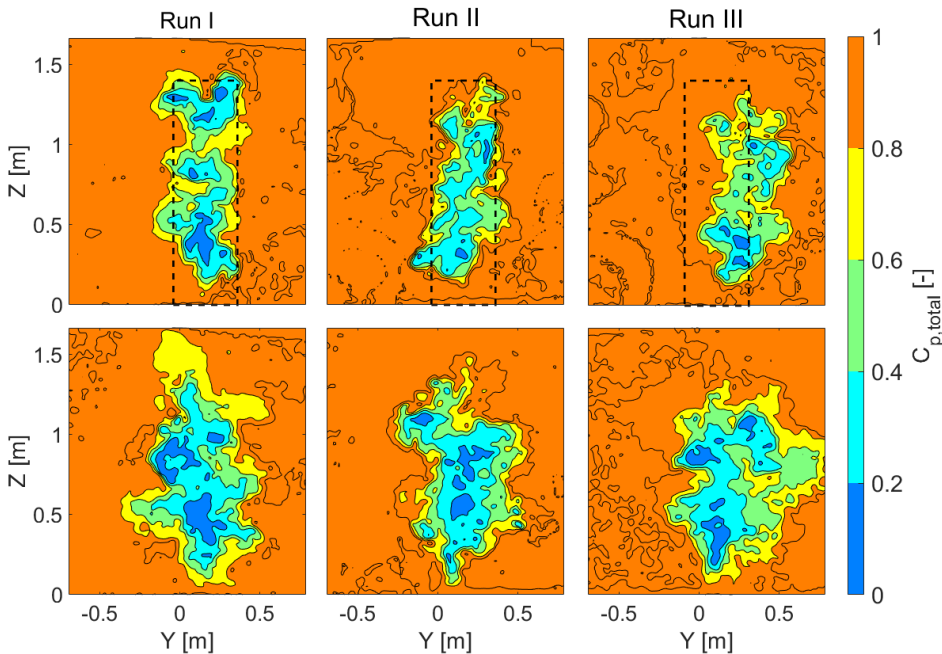


Figure 6.12: Instantaneous total pressure coefficient ($C_{p,total}$) contours 0.1 m upstream of the trailing cyclist (top) and 0.5 m downstream of the trailing cyclist (bottom). The dashed rectangle indicates the location of the trailing cyclist relative to the wake of the leading cyclist.

The differences in total pressure ($\Delta P_{tot} = (P_{tot,draft} - P_{tot,indv}) / P_{tot,indv}$) is presented in Table 6.4. Upstream ΔP_{tot} is defined as the difference in instantaneous total pressure in front of the drafting cyclist and the ensemble-average total pressure in front of that same cyclist riding alone. Downstream ΔP_{tot} is defined as the difference in instantaneous total pressure drop behind the drafting cyclist and the sum of the ensemble-averaged total pressure drop behind both individual cyclists participating in the drafting configuration; an example could be a drafting configuration where the total pressure coefficient behind each rider drops by 25% when riding individually, and the total pressure

drop behind the peloton is 40%, then downstream $\Delta P_{tot} = 40\% - (2 \times 25\%) = -10\%$.

The results presented in Table 6.4 show that upstream of the drafting cyclist there is an average decrease of 45%, 35%, and 23% in total pressure for runs I, II and III, respectively. Following the methodology described in section 2, the drag reductions for the drafting cyclists in the three cases are found to be equal to 52%, 46% and 31%. This shows that the average drop in total pressure in front of the drafting cyclist is still underestimating the observed drag reductions slightly and thus part of the drag reduction should be found in the downstream ΔP_{tot} . For run I the downstream ΔP_{tot} is -4%, for run II and III this is -9% and -10%, respectively. This means higher total pressures in the wake of the drafting cyclist as compared to the sum of both individuals, resulting in a further reduction in the drag of the trailing cyclist.

Table 6.4: Drag reduction measured per configuration and the changes in spatial-average $C_{p,tot}$ upstream and downstream of the cyclist when drafting as compared to riding alone.

Configuration	Upstream ΔP_{tot} [%]	Downstream ΔP_{tot} [%]	Sum P_{tot} reduction [%]	Drag reduction [%]
Run I (C - B)	-45	-4	49	52
Run II (B - A)	-35	-9	44	46
Run III (B - A)	-23	-10	33	31

6

According to these findings, the sum of the difference in total pressure upstream and downstream of the drafting cyclist is close to the total drag reduction. Similar to findings in literature, all three cases show that the change in inflow conditions is the main cause of the drag reduction; however, with a difference up to 10%, the change in total pressure in the wake cannot be neglected. Additionally, it is observed that the bigger the longitudinal gap becomes, the bigger the effect on total pressure in the wake becomes.

DRAG ANALYSIS

The results of the drag reduction from the RoF measurements as a function of the longitudinal and lateral spacing between the riders are summarized in Figure 6.13. To obtain a better overview, all positions are plotted with a positive lateral separation. In practice lateral separation occurred in both positive and negative direction. Drag reductions between 27% and 67% are observed with a general inverse relationship between drag reduction and drafting distance, with high reductions where both longitudinal and lateral distances are low and low drag reductions where the lateral offset is higher. It is observed that the effect of lateral separation is much stronger than longitudinal separation, which is in agreement with Barry et al. (2014) and Zdravkovich (1996). The drag reduction of cyclist C in the configuration A-C is significantly higher than that found in the other configurations in the current study as well as those found by Barry et al. (2014), up to 67%. However a similar trend is observed: the drag reduction shows higher dependency on lateral displacements than on the longitudinal one. The higher drag reduction in this configuration is associated with the higher frontal area of A; as a consequence, the cyclist drafting behind rider A experiences the minimum total pressure inflow.

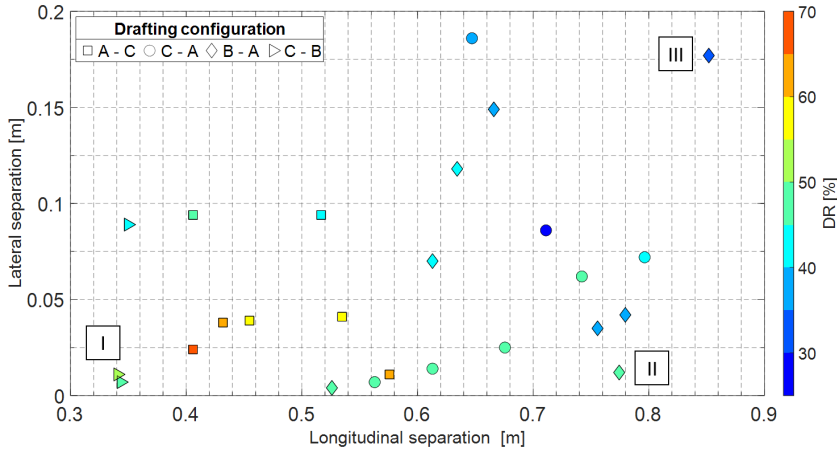


Figure 6.13: Reduction in drag area for the drafting cyclist at different positions behind the lead cyclist. To obtain a better overview, all positions are plotted with a positive lateral separation and the lateral separation is exaggerated. In practice lateral separation occurred in both positive and negative direction.

6.4.4. MODELLING DRAG REDUCTION

A semi-empirical model is attempted here for the use of predicting drag reduction under similar drafting conditions as the ones in the current experiment. In section 6.4.3 it was found that the drag reduction under drafting is proportional to the drop in total pressure, or kinetic energy (u^2), at the location of the drafting cyclist. In order to find a mathematical expression for the drag reduction, we need to find an expression for the spatial evolution of the velocity past a single athlete. The average streamwise velocity ($\overline{u_x}$) versus distance as well as the rate of lateral wake expansion versus distance in the near wake of a single athlete were presented in Figure 6.10 in section 6.4.2. It is assumed that the wake of a cyclist can be approximated as an axisymmetric wake flow behind a bluff body. Pope (2000) describes the following similarity relations for such a wake:

$$y_w(x) \sim x^{\frac{1}{3}}, \quad \frac{u_s(x)}{U_\infty} \sim x^{-\frac{2}{3}}, \quad f(\xi) = e^{B\xi^2}, \quad \xi = \frac{y}{y_w(x)} \quad (6.3)$$

where y_w is the wake half-width, u_s is defined as the centerline velocity deficit, U_∞ is the upstream velocity, ξ is the scaled cross-stream variable, $f(\xi)$ is the self-similar velocity defect and B is a non-dimensional constant. In section 6.4.2 we described that the velocity deficit in the wake of a cyclist approximately decays with $x^{-\frac{1}{3}}$, whereas the wake width expands linearly with x . Taking these findings into consideration, a mathematical expression for the drag reduction is proposed as follows:

$$DR(X, Y) = A \cdot X^{-\frac{1}{3}} \cdot e^{-B\left(\frac{Y}{X}\right)^2} \quad (6.4)$$

where A and B are parameters to be determined from the input of experimental or computational data. The parameters X and Y in equation 6.4 are the longitudinal and

lateral separation, respectively. The separation, in this work, is taken as the distance between the trailing edge of the rear wheel of the leading cyclist to the leading edge of the front wheel of the trailing one. The largest cross section and thus largest contributor to the drag force, however, is given by the athlete's body; at zero separation (no gap between the wheels), the distance between the bodies of the riders (from the lower back lead rider to head of trailing rider) is of the order of two characteristic length scales. The characteristic length scale for a cyclist wake c is considered to be the shoulder width, approximately $c = 0.5$ m.

MODEL INPUT DATA AND UNCERTAINTY

In order to estimate the model parameters described in equation 6.4, data needs to be fitted to the model. Since the data set obtained by the Ring of Fire, as described in section 6.4.3, only comprises 25 data points (50 when symmetry about the XZ-plane is assumed), the drag measurements from Barry et al. (2014) are added to the data set, increasing the total amount of data points to 100. Barry et al. (2014) carried out measurements in the wind tunnel with two full-scale models on time-trial bikes at a test velocity of 18 m/s. The drafting locations tested by Barry et al. (2014) are ranging from 0.1 – 0.7 m and 0 – 0.275 m in longitudinal and lateral direction, respectively. The combined data set was fitted to the model by the non-linear least-squares method and in order to minimize the influence of outliers, the method of Bi-square weights was applied (Yu and Yao, 2017). The parameters A and B are estimated with 95% confidence intervals, yielding $A = 35.3 \pm 2 \text{ m}^{1/3}$ and $B = 1.04 \pm 0.3$ respectively. The predicted DR obtained from the model has a RMSE of 9.9 and R-square of 0.28 and is plotted in Figure 6.14 alongside the data points used for fitting.

6

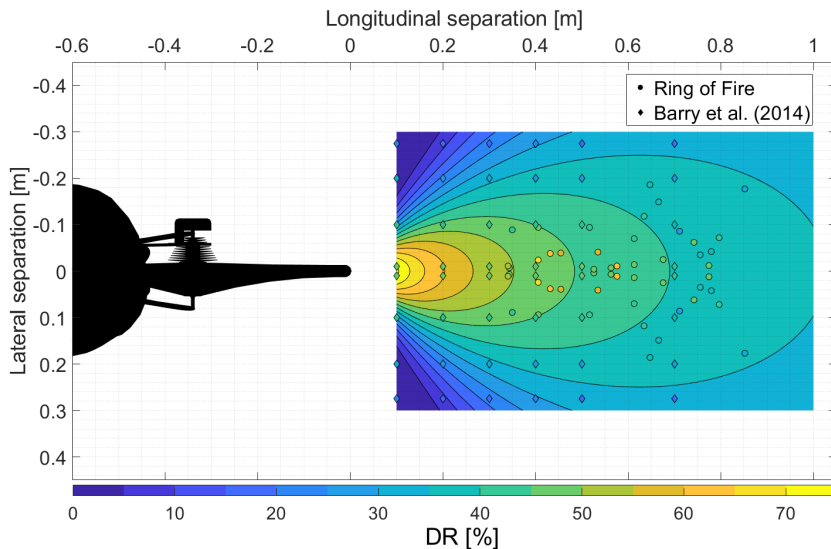


Figure 6.14: Drag reduction according to the mathematical model described by equation 5 (colour contours), based on data input from the current experiments (colour-coded circles) and from Barry et al. (2014) (colour-coded diamonds).

As the range of the combined data set is limited to $0.1 \text{ m} \leq X \leq 1 \text{ m}$ and $-0.3 \text{ m} \leq Y \leq 0.3 \text{ m}$, the range of validity of this model with the estimated parameters A and B is limited to this region. Furthermore, it should be noted that this model is only valid for two cyclists in time-trial posture, as adding more riders or changing posture will influence the drag reduction of the second rider (Blocken et al., 2013, 2018).

Figure 6.15 compares the DR reported in literature to the DR found by our model. On the left the change in DR w.r.t. change in longitudinal distance at 0 lateral offset is presented, in the middle and on the right the change in DR with lateral distance at 0.3 and 0.7 m longitudinal offset, respectively, is shown. Close to the leading cyclist, (longitudinal $< 0.3 \text{ m}$ and lateral = 0 m), the model yields some overestimated drag reduction compared to literature, which indicates that more data points might be needed close to the leading cyclist in order to get a better fit of the model. When the trailing cyclist is laterally offset, the predictions of the proposed model shows a similar rate of decline in DR as compared to what was found by Zdravkovich (1996); however the predicted DR by our model is higher, which may be due to the difference in experimental conditions.

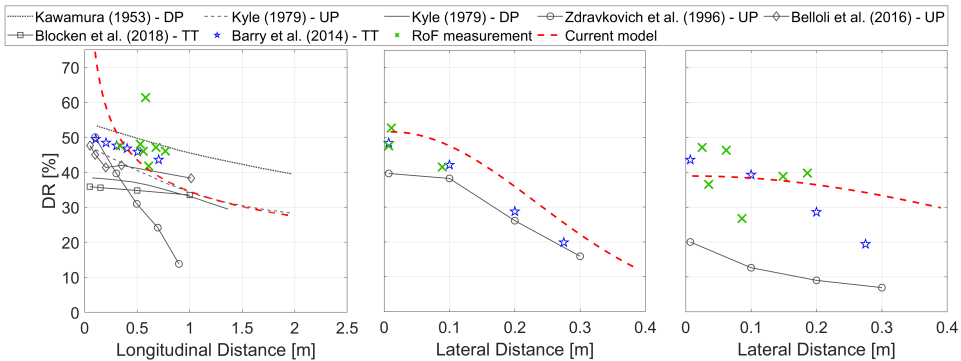


Figure 6.15: Trailing cyclist drag reduction by longitudinal and lateral offset reported in literature and from the mathematical model described in this work. Left: effect of longitudinal distance taken at zero lateral offset. Middle: effect of lateral distance taken at 0.3 m longitudinal separation. Right: effect of lateral distance taken at 0.7 m longitudinal separation.

6.5. CONCLUSIONS

Ring of Fire experiments have been carried out to investigate the aerodynamics of cyclists riding at short distance from each other (drafting). The drag force is inferred from a momentum conservation approach that is adapted from Spoelstra et al. (2019) where the aerodynamic drag from individual athletes was determined. The flow field visualizations show that the amount of drag reduction of the trailing rider should be mainly ascribed to the inflow conditions featuring a pronounced momentum deficit. Within the measured range of longitudinal separation, the drag reduction for the drafting cyclist ranges from 27% to 66%. The aerodynamic advantage, however, decreases as the lateral and longitudinal separation between riders is increased, where the lateral distance is found to produce a more rapid effect. A mathematical expression is proposed that describes a

model introduced to predict the drag reduction under drafting conditions. Input from current experiments as well as from literature data returns a realistic prediction of the drag reduction in the near wake with an overestimation of the drag reduction at longitudinal distance between 0.1 m and 0.3 m.

Besides the above results, the RoF demonstrates its potential to investigate cycling aerodynamics and simultaneously monitor the drafting skill level of cyclists, which is currently not practiced with the current state-of-the-art measurement techniques for cycling aerodynamics.

7

SPEED SKATING

This chapter demonstrates the range and flexibility of the Ring of Fire by deploying it to study the aerodynamic performance of speed skaters during their natural skating motion. An aerodynamic assessment is presented of two elite skaters, each in two different skating configurations. Athlete A skates with two hands on the back and with only one hand on the back. Athlete B skates with both arms loose in a low trunk posture and in a high trunk posture by varying his knee and trunk angles. Firstly, the wake velocity fields of skater A, with two hands on the back, are presented throughout five different phases of the skate stroke, providing a better understanding of the overall skater aerodynamics. Secondly, average streamwise velocity and vorticity field for all 4 different postures are presented and compared. Finally, the aerodynamic drag of the four postures is compared.

This chapter has been submitted for publication as: **Spoelstra A.**, Terra W. and Sciacchitano A. (2021) On-site aerodynamics investigation of speed skating. *Journal of Wind Engineering and Industrial Aerodynamics (under review)*.

7.1. INTRODUCTION

The aerodynamic drag plays a crucial role in elite speed skating performance. Oggiano and Sætran (2010) estimated the contribution of the aerodynamic drag, or air resistance, to about 90% of the overall drag (the opposing forces). Knowing that the speed of a skater depends on the balance between the propelling forces (generated by the athlete) and the opposing forces, reducing the main opposing force yields an increase of the skater's speed and in turn of the chances of winning races.

The aerodynamic drag can be reduced, among others, by streamlining the athlete's suit (Oggiano and Sætran, 2008; Timmer and Veldhuis, 2021; van Ingen Schenau, 1982), wearing a helmet (Puelles Magán et al., 2021) and changing the athlete's posture, e.g. optimizing the trunk or knee angle (van Ingen Schenau, 1982). To the best knowledge of the authors, all these aerodynamic studies have considered skaters, or skater models, in static poses in wind tunnels or numerical simulations in order to measure differences in drag. Skating, however, is a very dynamic sport in which the posture of the athlete continuously changes through a repetitive motion of skate strokes (e.g. Van der Kruk, 2018). Such changing posture also affects the aerodynamic drag (D'Auteuil et al., 2012) and, hence, when aiming to reduce the aerodynamic drag of a skater, the entire skating stroke should be subject of study, instead of a single pose only. Such an aerodynamic assessment, of a skater during its natural skating motion, is missing in the literature, presumably because it is technically challenging.

In other speed sports such as cycling, field testing or on-site aerodynamic testing has been successfully achieved. The most common approach relies on the use of power meters: cycling speed and the exerted power by the athlete on the bike are used to estimate aerodynamic drag (e.g. Broker et al., 1999). Instrumented clap skates can measure the power exerted to the ice. However, in contrast to cycling, in skating the relation between the exerted power and the forward motion is yet unknown (Van der Kruk, 2018); thus, instrumented clap skates cannot be used to assess the aerodynamic drag. An alternative is the application of the Ring of Fire system, which relies on measuring the air flow across a transiting athlete and, by invoking the conservation of momentum, provides the aerodynamic drag. This measurement system has been validated for aerodynamic investigation of elite cyclists in the previous chapters.

This chapter aims to use the Ring of Fire system to assess the aerodynamic performance of speed skaters on the ice during their natural skating motion. Velocity and vorticity fields, in a plane orthogonal to gross skating direction, downstream of two elite skaters are presented. These wake velocity fields are presented throughout the different phases of the skate stroke providing a better understanding of the overall skater aerodynamics. They are also compared to literature and the similarities and differences are discussed between the flow around a static skater and one in its natural motion. Furthermore, for each of the skaters two different skating configurations (skating with one arm vs. two arms on the back and low trunk vs high trunk) are investigated. Finally, the aerodynamic drag is presented of the different skating configurations.

7.2. EXPERIMENTAL SETUP AND PROCEDURES

7.2.1. TEST FACILITY AND SUBJECTS

Measurements were conducted at Thialf, an ice arena in Heerenveen in the Netherlands used for long track speed skating, short track speed skating, ice hockey, and figure skating (Thialf, 2021). Experiments were conducted on the 400 m track (see Figure 7.1 and Figure 7.2). A male and a female skater, both professional athletes, participated in the experiment. To keep their identities anonymous, we only report on their approximate anthropomorphic characteristics. Their body mass was in the range of 75 - 80 kg and 65 - 70 kg; and their height was in the range of 175 - 180 cm and 170 - 175 cm for the male and female athlete, respectively. Their shoulder width was approximately 60 cm. They wore a typical long leg and long arm hooded skate suit. In addition to the skin suit, the skaters wore laser safety goggles for protection against the PIV laser light. During the entire measurement campaign the air conditioning system of Thialf was shut off so to minimize any air recirculation.

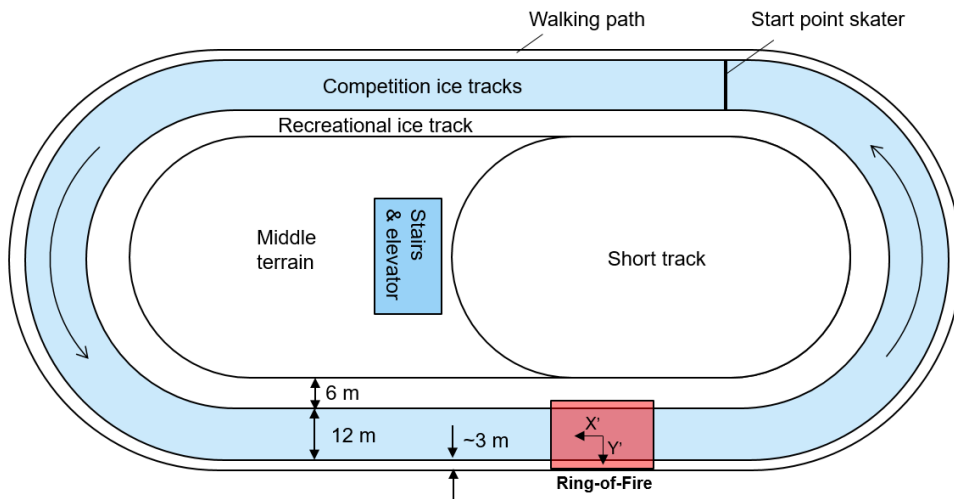


Figure 7.1: Top view of the testing facility.

For each of the participants, two different skating configurations were examined. The configurations were characterized by the position of the arms (loose vs. stuck to the body) and the knee θ_0 and trunk θ_1 angles (Figure 7.3). For the female participant, skating with two arms on the back vs. one arm on the back and one loose, was investigated for the body angles $\theta_0 = 97^\circ$ and $\theta_1 = 16^\circ$. The male participant, instead skated all the time with both arms loose changing his body angles between a high trunk posture ($\theta_0 = 92^\circ$ and $\theta_1 = 16^\circ$) and a low trunk posture ($\theta_0 = 84^\circ$ and $\theta_1 = 0^\circ$). A frontal and side view of each of the postures is shown in Figure 7.3.

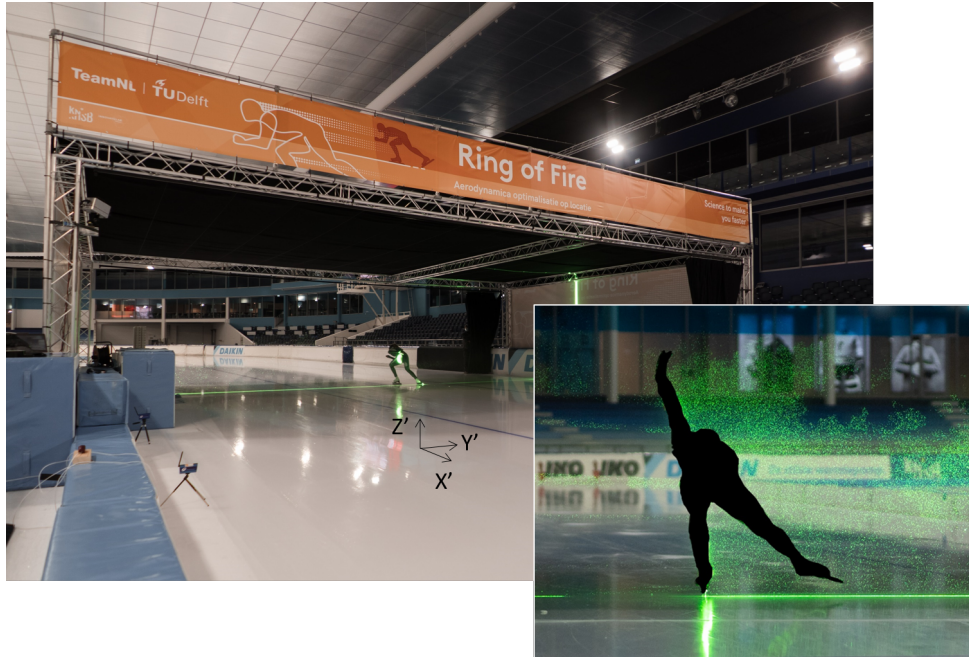


Figure 7.2: Ring of Fire on the ice of Thialf. An athlete skating through a cloud of helium filled soap bubbles.

7

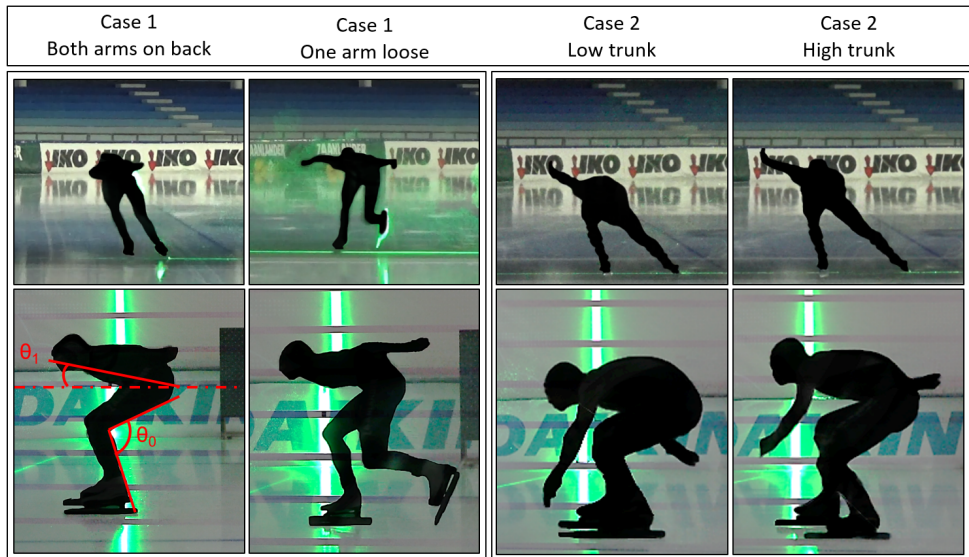


Figure 7.3: Frontal and side views of the four different postures studied in this work.

7.2.2. PIV SYSTEM

The velocity distribution upstream and in the wake of the skater was obtained by large-scale stereoscopic-PIV. The use of neutrally buoyant helium-filled soap bubbles (HFSB) as flow tracers (Scarano et al., 2015), with an average diameter of 0.3 to 0.4 mm, provided sufficient light scattering to visualize the flow in a field of view of approximately 7 m^2 . A tunnel of $10 \times 13 \times 3 \text{ m}^3$ in X, Y, and Z direction (see Figure 7.2) was used to confine the bubbles within the measurement volume. The tunnel had an open in- and outlet to allow the skater to transit and was equipped with optical access on one side for illumination purposes. The HFSB were introduced into the tunnel by a rake with 200 nozzles located 1 m upstream of the measurement plane and on the warm-up lane of the ice track. A Quantronix Darwin Duo Nd: YAG laser provided pulsed illumination (at a frequency of 1kHz, the pulse energy is $2 \times 25 \text{ mJ}$). The laser beam was shaped into a 50 mm thick sheet by means of laser optics. The field of view was imaged by two Photron Fast CAM SA1 cameras (CMOS, 1024×1024 pixels, 12 bits) equipped with 50 mm objectives at $f/5.6$ and a cropped sensor size of 1024×752 pixels. Images were acquired at 0.5 kHz. The cameras were mounted on the metal structure of the tunnel 6 m upstream of the measurement plane at a height of 2.5 m with an angular separation of 90 degrees, imaging a field of view of $3.2 \times 2.3 \text{ m}^2$. The resulting magnification factor was 0.006 and the digital image resolution 0.3 px/mm. The tracer particles were held in the measurement domain by closing entrance and exit gates of the tunnel before the passage of the skater, accumulating for about two minutes. A detailed sketch of the RoF setup is shown in Figure 7.4.

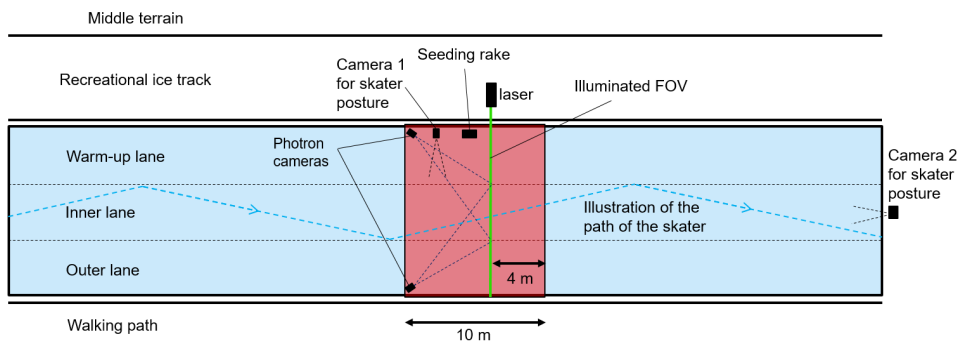


Figure 7.4: Schematic representation of the experimental layout of the RoF for the skating experiments.

7.2.3. MEASUREMENT PROCEDURE

The PIV system was calibrated at the beginning of each measurement day. Bubble production was initiated about two minutes before the start of each run to achieve a uniform tracer distribution with sufficient concentration in the measurement domain. For each posture, the experiment was repeated 10 times to build an ensemble average estimate of the aerodynamic drag from the RoF. For all trials, the athlete started on the opposite side of the track (marked in Figure 7.1), accelerated to the prescribed velocity of 11 m/s and maintained such velocity in the corner after the measurement region. The velocity

and position of the skater when gliding through the Ring of Fire setup were monitored with the ProChip Timing System by MYLAPS Sports Timing (Mylaps, 2021) and two extra cameras, respectively (see Figure 7.4). One of the cameras provided a side view of the skater and the other a frontal view. Images taken by these cameras can be seen in Figure 7.3.

7.2.4. DATA REDUCTION

During the experiments, the skaters were not specifically instructed to pass through the measurement plane in a specific phase of the skating motion and, hence, the pose of the skater, when passing through the measurement plane, varied between repeating passages through the Ring of Fire system. All skater poses are categorized into one out of five phases of the skating motion, which are described by Van der Kruk (2018) and shown in Figure 7.5. Phase 1 is the glide phase, during which the mass of the skater is supported over one leg and both skates are on the ice. When the skater moves his center of mass away from the support leg and hence introducing a leg extension, the second phase is entered, also known as the push-off phase. The push-off phase ends when the leg is at its maximal extension. In phase 3 the extended leg leaves the ice to be retracted under the body of the skater, which is phase 4. Phase 4 ends when the skate is placed on the ice again, whereby the glide phase (phase 5) begins again and completes one stroke. This categorization is used later in this work to discuss the variation of the skater's near wake during the skating motion.

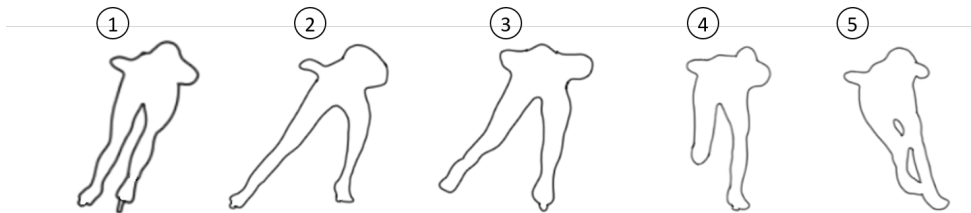


Figure 7.5: Contours of the skater (configuration: two hands on the back) in the five phases during the skating motion as introduced by Van der Kruk (2018). Contours obtained from the present experiment.

From the acquired PIV images (at 0.5 kHz) only 10 image pairs with a spacing of 50 images are processed. The first image pair is chosen directly after the skater passes through the laser sheet. In other words, in the wake of the skater ten velocity fields are processed with a 0.1 second interval, in which approximately 1 meter is covered by the skater. The down sampling process for the first 4 velocity fields is illustrated in Figure 7.6. The velocity field closest to the athlete is later used in this work to discuss the skater's near wake. The remaining ones are used only for drag determination.

The chosen image pairs are processed by cross-correlation analysis using the LaVision DaVis 8.4 software. Following the analysis in Chapter 5, the final interrogation window size is selected to be 32×32 pixels ($100 \times 100 \text{ mm}^2$), and the overlap factor is set to 75%. The evaluation of the skater's drag via the control volume approach requires that mass conservation at the inflow and outflow of the domain is accurately satisfied, assuming there is no momentum transfer through the side faces of the domain. However,

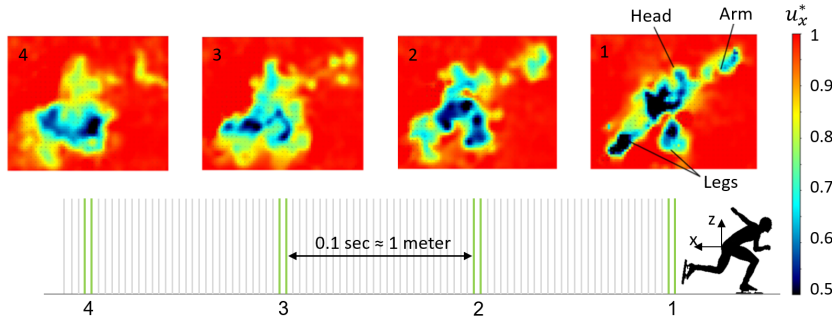


Figure 7.6: Example of velocity fields measured with the Ring of Fire for each passage of a skater. Grey are all acquired images, green are the ones used for processing.

since the velocity along the side of the measurement domain is unknown, this assumption cannot be made in the current measurement. One way to mitigate the errors associated with an approximate conservation of mass is to reduce the momentum analysis to the area where the largest deficit occurs. This is done by the wake contouring method discussed in Chapter 5. Furthermore, the pressure field is reconstructed by solving the pressure Poisson equation (PPE) (van Oudheusden, 2013). Neumann boundary conditions are applied at the boundaries and the resulting pressure distribution is scaled with the measured quiescent air pressure as reference.

The methodology for obtaining the drag force (Section 4.2) measures the force in the X-direction (lane direction), whereas the skater experiences a force in the direction opposite to its motion, which is generally not parallel to the skating lanes. Considering the typical angles of the skating path with respect to the lanes of the ice rink, the drag is underestimated typically by 2%. However, considering that the skating path does not vary among the different configurations investigated, this work is able to assess the drag differences among different skating configurations.

The time ensemble average drag area ($\overline{C_d A}$, Equation 4.4) is computed for each skating posture. The final number of passages used for ensemble-averaging after discarding the faulty ones varies for each case from 8 to 10. For the drag evaluation, the first velocity field, at 0.1 m behind the skater, of each skater passage is discarded because of reflections in the PIV images in some of the measurements.

7.3. RESULTS

7.3.1. ENVIRONMENTAL AIRFLOW CONDITIONS BEFORE TRANSIT

The environmental air conditions that are experienced by skaters can have a significant effect on the skaters aerodynamic drag (e.g. D'Auteuil et al., 2012). Therefore, the undisturbed air flow of the present experiments, so before the passage of the skater, is characterized. Prior to the passage of the skaters, the air flow rarely is completely still. External conditions and the seeding injection cause the environmental flow motions to have a velocity that is generally non-zero, non-uniform, and non-stationary. The time average environmental flow field, $\overline{u_1}$, and the RMS of its fluctuations, $u'_{1,RMS}$, is depicted in Fig-

ure 7.7 and Figure 7.8, respectively. These statistics are obtained from 20 skater passages.

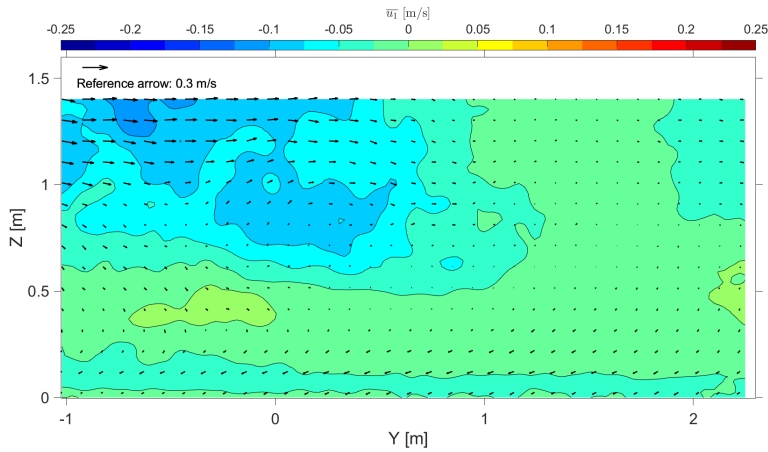


Figure 7.7: The environmental flow field before passage of the athlete averaged over 2 seconds and 20 runs (20×0.1 s). Velocity vectors and colour contours represent the in-plane velocity components and the streamwise velocity component, respectively.

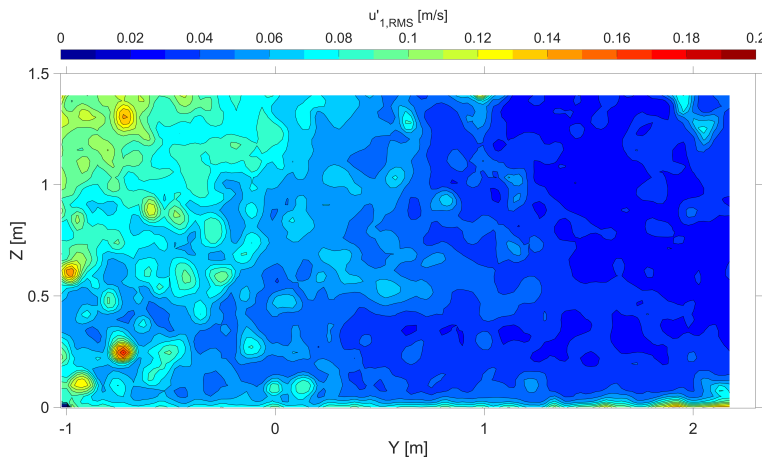


Figure 7.8: RMS of the velocity fluctuations in X-direction before passage of the athlete averaged over 2 seconds and 20 runs (20×0.1 s).

The seeding injection from the left (looking at the back of the skater) creates a clear inflow of momentum into the measurement region. Both out-of-plane and in-plane velocities up to 20 cm/s are observed on the left side, whereas in the rest of the measurement region the out-of-plane velocities are within ± 2.5 cm/s and the in-plane velocities are close to 0. Also in terms of fluctuations, the left side is clearly influenced by the seeding injection with peaks in RMS up to 15 cm/s. On the right side, on the other hand, the RMS values never exceed 2 cm/s. In almost all runs, the skaters passed through the

measurement region at $-1 \leq Y \leq 1$ and hence, for a correct estimate of the drag value, the velocity distribution prior to the passage is taken into account for the drag computation via equation 4.1 as it contributes to the overall momentum budget, as also discussed by Terra et al. (2018).

7.3.2. FLOW VISUALIZATIONS FOR THE DIFFERENT SKATING PHASES

In this section the near wake velocity of one skater is presented approximately 50 cm downstream of the athletes' thighs (plane one in Figure 7.6). Figure 7.9 present the streamwise velocity in the wake together with the corresponding skating phase for a skater with both arms on the back. Note that the skater contours in Figures 7.9 to 7.13 are meant as an indication of the location of the skater with respect to its wake and do not reproduce the exact location of the skater. From the instantaneous velocity fields (snapshots of a single skater passage) it is observed that the wake is clearly changing throughout the skating motion. In phase 1, with both skates on the ice and the legs relatively close together, areas of significant velocity deficit are observed downstream of the legs and the upper body. The wake of the left and the right leg are somehow merged, suggesting an interaction between the flow around these legs.

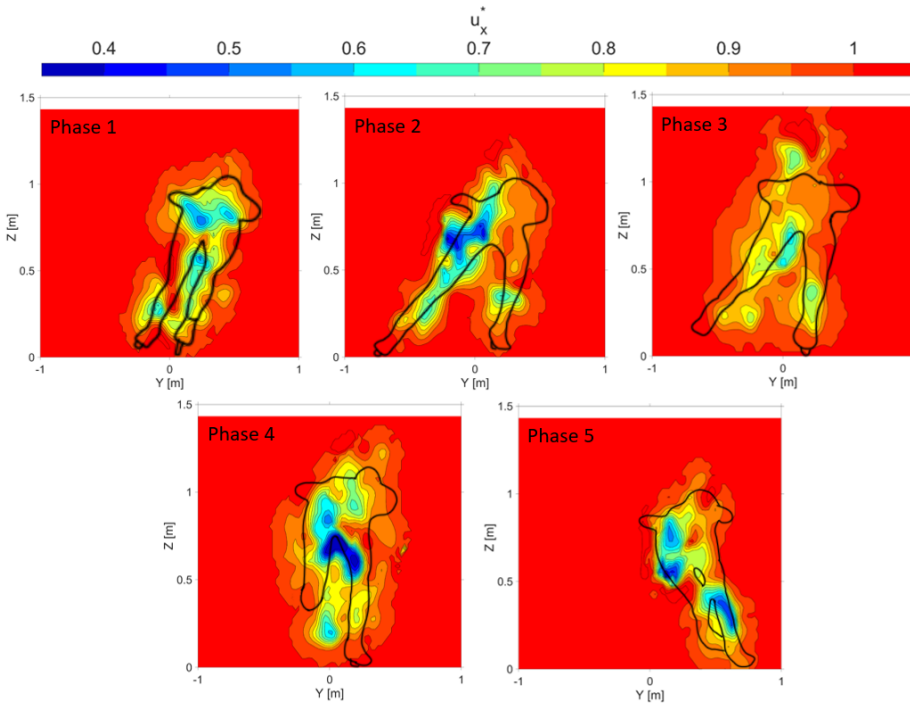


Figure 7.9: Instantaneous streamwise velocity u_x^* at $X = 0.5$ m for skater A with both arms on the back corresponding to the different skating phases as described by Van der Kruk (2018). The skater contours are meant as an indication of the location of the skater with respect to its wake and do not reproduce the exact location of the skater.

In phase 2, instead, the legs are further apart and the wakes of the lower legs and feet are clearly observed as individual flow structures. The wake in this phase is relatively large indicating that the aerodynamic drag is relatively high as well, which will be discussed further in the end of this section. When moving into phase 3, the skater lifts her left leg and retracts it. Hence, not only the orientation, but also the streamwise velocity of the lower leg itself is reduced. This reorientation of the legs results in reduction of the velocity deficit downstream of the left leg and hip as can be observed in Figure 7.9. In skating phase 4, the gliding phase, the legs are brought closer together and as a consequence their wake narrows and the peak velocity deficit increases. Finally, in phase 5, when the skater is leaning to the left, her wake is further narrowed and the velocity deficit behind the legs peaks. Another observation, when comparing the different phases, is that the height of the wake increases from phase 1 to 3 and, subsequently, decreases afterwards through phase 4 and 5. This variation in wake height is probably the result of an up-and-down movement of the upper body as reported by Van der Kruk (2018).

A reliable estimation of the aerodynamic drag of each of the skating phases requires a substantial ensemble of velocity snapshots in each phase. From the present data set only one, sometimes a few, snapshots per phase are available and, hence, an accurate estimation of the variation of the aerodynamic drag is not possible. Instead drag data from literature is used to relate to the present velocity fields. D'Auteuil et al. (2012) measured the aerodynamic drag on a static skater mannequin in three different poses, which may be categorized as phases 2, 4 and 5. In phase 2, the aerodynamic drag peaks, while it is minimum in phase 4. This corresponds to the relatively widespread and compact wakes in phase 2 and 4, respectively, resulting from the different leg orientations. Additional measurements on skaters on the ice are necessary for a more detailed discussion on the relation between the variation of the wake velocity and the aerodynamic drag throughout the skating motion.

7

7.3.3. FLOW VISUALIZATIONS FOR SKATER A: TWO ARMS VS. ONE ARM ON THE BACK (CASE 1)

The average streamwise velocity and vorticity fields measured 0.8 m behind the lower back of skater for both postures in case 1 are shown in Figure 7.10 and Figure 7.11, respectively. For both postures the average is obtained from 2 passages. As shown in Figure 7.3, the skater passed the laser sheet in phase 1 when both arms are on the back and in phase 4 when she passed with only one arm on the back.

The streamwise velocity contours clearly show two different shapes, which shows a strong dependence on the skating phase (as already discussed in Section 7.3.2) as well as the skating posture. The wake of the athlete with both arms on the back, Figure 7.10-left, shows three distinct regions of velocity deficit. The highest deficit (lowest u_x^*) is located behind the lower back ($Z = 0.8$ m & $X = 0$ m). A second big region of deficit is located behind the legs ($Z \leq 0.6$ m) and finally a small deficit is seen behind the left leg/foot ($Z = 0.3$ m & $X = -0.5$ m), which is slightly sticking out from under the body (see Figure 7.3). We observe a few differences when comparing these findings with the streamwise velocity contour behind the skater with only one arm on the back (Figure 7.10-right). Firstly, the strongest region of deficit is located behind the left leg/foot ($Z = 0.5$ m & $X = 0$ m). The minimum velocity of $u_x^* = 0.5$ is lower in this posture as the

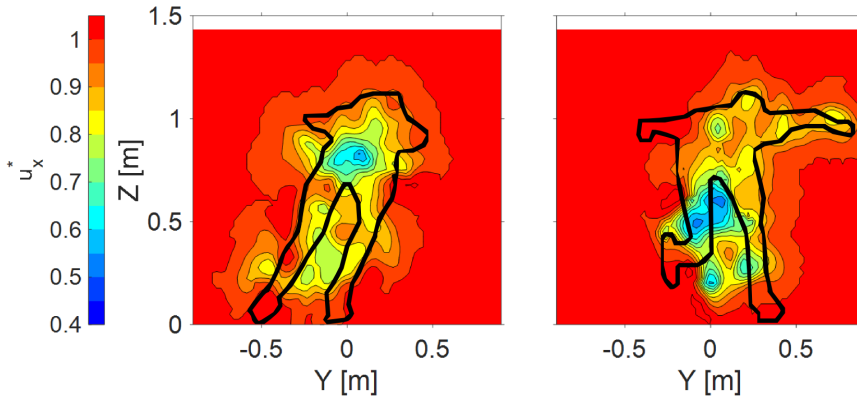


Figure 7.10: Average streamwise velocity u_x^* at $X = 0.8$ m for the skater with both arms on the back (left), and with only one arm on the back (right). Average obtained from two runs.

corresponding body segments (leg and foot) are located closer to the evaluated plane. Similar findings were reported by Puelles Magán et al. (2021), where the mannequin used in the numerical simulations was in a similar skating phase; however, with both arms on the back. Secondly, there is a clear region of deficit behind the right arm, ($Z = 1$ m & 0.4 m $\leq X \leq 0.6$ m) which, as can be seen in Figure 4, is loose from the body. Finally, there is a region of velocity deficit located behind the head ($Z = 1$ m & $X = 0.1$ m) which is not seen in the wake of the other posture.

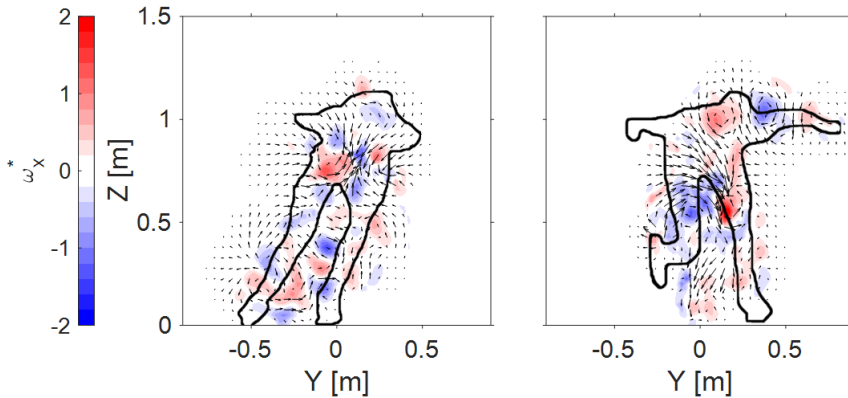


Figure 7.11: Average streamwise vorticity ω_x^* at $X = 0.8$ m for the skater with both arms on the back (left), and with only one arm on the back (right). Average obtained from two runs.

Puelles Magán et al. (2021) reported the presence of a counter rotating streamwise vortex pair in the wake of a skater. This characteristic vortex pair is also visible in Figure 7.11 for both postures. When both arms are on the back, this vortex pair is located at the height of the lower back ($Z = 0.8$ m), whereas when only one arm is on the back, the vortex pair is pushed down by a strong inwash flow over the left leg (side where the arm

is attached to the body). Furthermore, it has to be noted that, for the case where only one arm is on the back, a second counter-rotating vortex pair is originated behind the head ($Z = 1 \text{ m}$ & $X = 0.1 \text{ m}$), indicating a significant upwash trend.

7.3.4. FLOW VISUALIZATIONS FOR SKATER B: LOW TRUNK VS. HIGH TRUNK (CASE 2)

Similar as was done for case 1 above, the average streamwise velocity and vorticity fields measured 0.8 m behind the lower back of skater for both postures in case 2 are shown in Figure 7.12 and Figure 7.13, respectively. For both postures the average is obtained from 3 passages where the skater is in the gliding phase with the left skate out and the right arm loose from the body.

For both postures, the streamwise velocity contours clearly exhibit a similar shape, nevertheless the wake of the low trunk posture is smaller in height. Both show the strongest velocity deficit behind the trunk / upper legs and some smaller deficits behind the right arm and the left leg. In general, the wake of the high trunk posture seems to feature higher deficits compared to the wake of the low trunk posture.

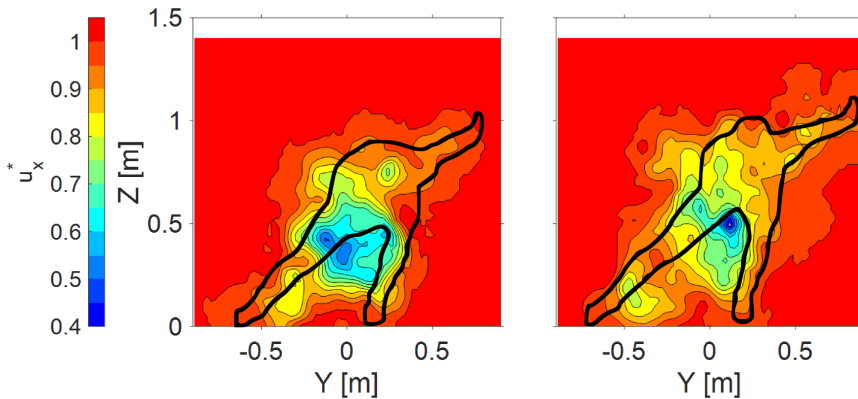


Figure 7.12: Average streamwise velocity u_x^* at $X = 0.8 \text{ m}$ for the skater in low trunk posture (left), and in high trunk posture (right). Average obtained from three runs.

In Figure 7.13 the same main counter rotating streamwise vortex pair behind the lower back / upper legs is again observed for both postures. Similar to the posture with one arm loose in the previous case, there is a strong inwash flow over the left leg (again the side where the arm is attached to the body) pushing the vortex pair down. Furthermore, the second counter-rotating vortex pair originating from the head ($Z = 0.8 \text{ m}$ & $X = 0.4 \text{ m}$) is visible for both high and low trunk posture. In contradiction with the upwash trend created by the head vortex pair in Figure 7.11-right, here the vortex pair produces a slight downwash trend. This possibly depends on the swing motion of the right arm. In case 1 the arm is almost horizontal, in a downward movement, whereas in case 2 the arm in both postures is pointing up 45 degrees with respect to the horizontal and is in an upward movement. These swing motions cause a downwards and upwards flow behind the arm, respectively. The effect of the frequency of the arm swing possibly also has an

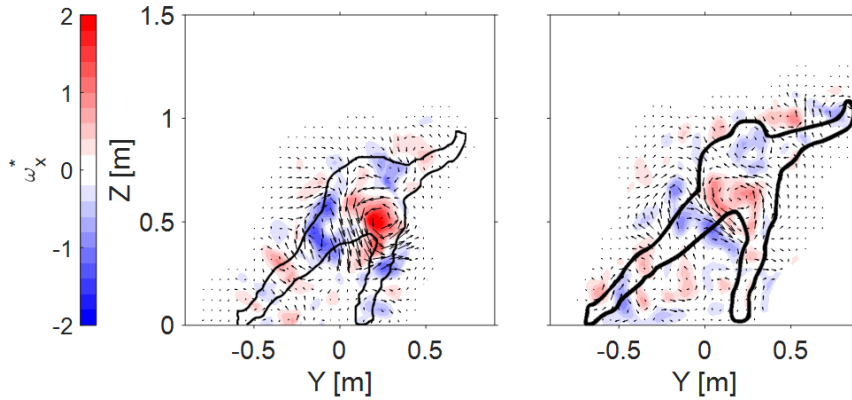


Figure 7.13: Average streamwise vorticity ω_x^* at $X = 0.8$ m for the skater in low trunk posture (left), in high trunk posture (right). Average obtained from three runs.

influence on the overall flow structures in the wake, however, this is outside of the scope of this work.

7.3.5. DRAG ANALYSIS

The time ensemble average drag area ($\overline{\overline{C_d A}}$, Equation 4.4) for the different skating configurations is calculated from the measurements of each individual passage through the Ring of Fire. Figure 7.14 and Figure 7.15 show the streamwise $C_d A(t)$ evolution in the wake for the different skating configurations for case 1 and case 2, respectively. The streamwise development of $C_d A(t)$ for each passage is presented separately in grey. The spread of these values provides insight into the repeatability of the measurements and thus, among other things, also into how well the skater could repeat his or her posture over multiple runs. Furthermore, the ensemble average drag area ($\overline{C_d A}$, Equation 4.3) is plotted in red in Figures 7.14 and 7.15.

For case 1 (Figure 7.14), it is observed that the skater exhibited a larger variation in the posture when skating with the two arms in the back. After inspection of the raw images, it was found that the larger spread was caused by the fact that for the ‘two arms on back’ posture the skater passed the measurement region almost every passage in a different skating phase, whereas for the ‘one arm on the back’ posture the skater was able to pass every run more or less in the same skating phase. This finding indicates that the aerodynamic drag varies during the skating motion. Therefore, it might be interesting to investigate this in a next study.

The spread between the streamwise drag area $C_d A(t)$ (grey lines) for the different passages in Figure 7.15 is clearly smaller than that in Figure 7.14 and the difference in the $\overline{C_d A}$ (red lines) between the two postures is also more visible than in the previous case, indicating a larger difference in time ensemble average drag area $\overline{\overline{C_d A}}$ and smaller uncertainties.

The data from the different passages is combined to obtain the time ensemble av-

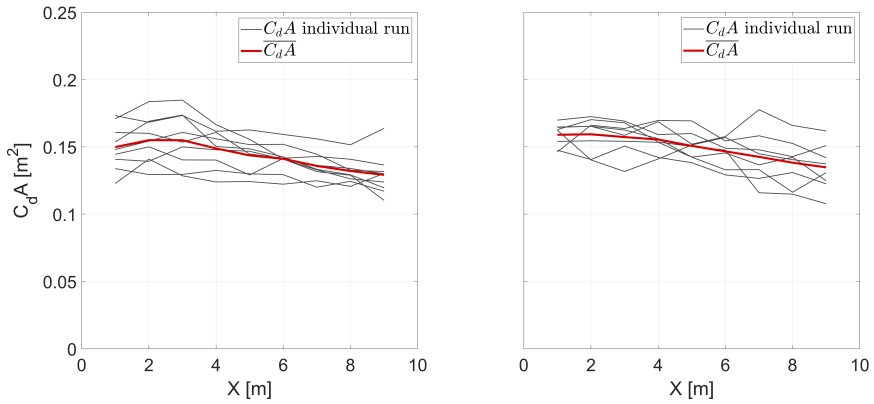


Figure 7.14: Streamwise $C_d A$ evolution in the wake for the case with both arms on the back (left) and with only one arm on the back (right).

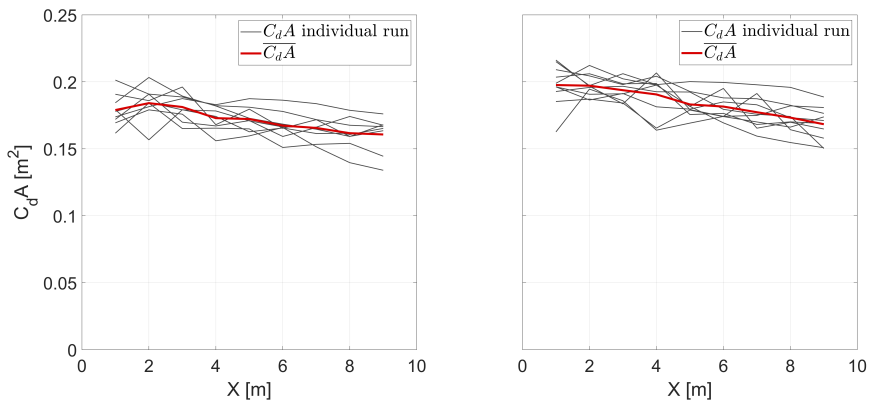


Figure 7.15: Streamwise $C_d A$ evolution in the wake for the low trunk posture (left) and for the high trunk posture (right).

average drag areas $\overline{\overline{C_d A}}$ for the different skate configurations, which are plotted in Figure 7.16. For the ‘two arms on back’ posture of case 1, the drag area is found to be 0.144 m^2 , with a 95% confidence level uncertainty of $\pm 0.009 \text{ m}^2$. For the ‘one arm on the back’ posture the drag is increased to 0.151 m^2 with an uncertainty of $\pm 0.008 \text{ m}^2$ at 95% confidence level. For case 2 the $\overline{\overline{C_d A}}$ for the high trunk is 0.185 m^2 and for the low trunk is 0.172 m^2 with a 95% confidence level uncertainty of $\pm 0.006 \text{ m}^2$ for both postures.

In order to determine whether the difference in mean drag area ($\overline{\overline{C_d A}}$) for the different configurations (one arm on back vs. two arms on back; and high trunk vs. low trunk) is statistically significant, the two-sample t-test is used (Snedecor and Cochran, 1996). For this test to be valid, the data is assumed to be independent, normally distributed, and the variances for the two independent groups are equal. The latter is confirmed by an F-test (Snedecor and Cochran, 1996). The significance level is $\alpha = 0.05$, and the null

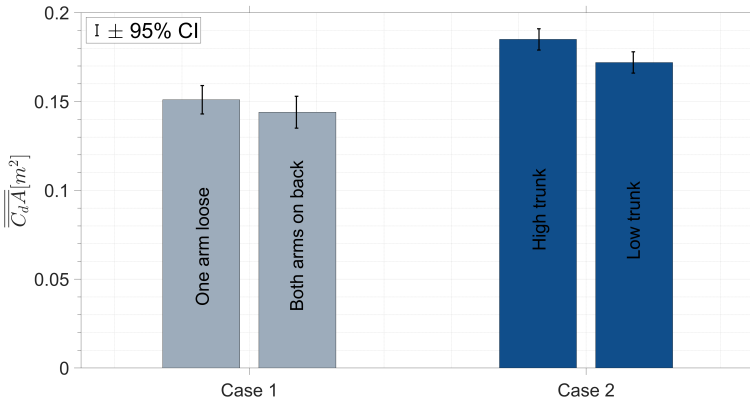


Figure 7.16: Comparison between the time ensemble average drag area $\overline{C_d A}$ for the different configurations; uncertainty bars for 95% confidence interval.

hypothesis is $\overline{C_d A_1} = \overline{C_d A_2}$. In other words, there is a 5% chance of concluding that a difference exists when there is no actual difference.

The results for the two-sided, two-sample t-test with assuming equal variances are presented in Table 7.1. The t-statistics for case 1 and 2 are 1.36 and 3.57, yielding p-values of 0.194 and 0.002, respectively. It is recalled that, when a p-value is less than or equal to the significance level α , the null hypothesis can be rejected, meaning that the measured difference between $\overline{C_d A_1}$ and $\overline{C_d A_2}$ is statistically significant. For case 1, the p-value is equal to 0.194, which is larger than $\alpha = 0.05$: thus, from the current measurements it is not possible to conclude if there is an aerodynamic benefit to skating with both arms on the back as compared to skating with only one arm on the back. On the other hand, for case 2, the p-value of 0.002 is clearly below the significance level: hence, it can be concluded that skating in the low trunk posture will provide the skater with a significant aerodynamic benefit.

Table 7.1: Two sample t-test parameters for the two different skating configurations.

	Case 1		Case 2	
	One arm loose	Both arms on back	High trunk	Low trunk
Mean $\overline{C_d A}$ [m ²]	0.151	0.144	0.185	0.172
Standard deviation [m ²]	0.009	0.012	0.008	0.008
Number of samples	8	9	10	9
Degrees of freedom (DF)	15		17	
t-statistic	1.36		3.57	
p-value	0.194		0.002	
Null hypothesis rejected (Difference statistically significant)	No		Yes	

7.4. CONCLUSIONS

In this chapter, the flow field in the wake of speed skaters in motion and their aerodynamic drag is measured using the Ring of Fire. A dedicated measurement setup was built on the 400 m track at Thialf in Heerenveen in the Netherlands. The skaters were skating through the Ring of Fire at a velocity of 11 m/s and the flow was measured before and after the passage of the skaters. Velocity fields in a plane orthogonal to gross skating direction, downstream of an elite skater are presented throughout the different phases of the skate stroke providing a better understanding of the overall skater aerodynamics. Furthermore, four different skating postures have been analysed with two different athletes. For the first athlete, the position of the arms was varied between both arms on the back and one arm swinging loose next to the body. The second athlete was swinging both arms loose for all the runs, but was varying his knee and trunk angles. For all the postures, an ensemble average streamwise velocity and vorticity field had been obtained. It was shown that in all cases the maximum velocity deficit in the wake was located behind the lower back and upper legs. Furthermore, the characteristic vortex pair in the wake of the skater model that was found by *Puelles Magán et al. (2021)*, was also seen here for all different test cases, indicating it is independent of the athlete, posture, and skating phase.

The time ensemble average aerodynamic drag is evaluated via a control volume approach along the wake behind the skater, accounting for the non-uniform flow conditions prior to the skater's passage. The uncertainty on the average drag measurements from the RoF is about 5%. To evaluate whether the differences between the mean drag areas were statistically significant, a two-sample t-test was performed. This test indicated that, with the RoF system, there is no measurable difference in drag between skating with both your arms on the back or with just one arm on the back. For the other case, skating with low trunk angle resulted in a drag reduction by 7.5% compared to skating with high trunk angle.

IV

EPILOGUE



8

CONCLUSIONS AND OUTLOOK

The work in this dissertation can be divided into two parts: firstly, development and assessment of the Ring of Fire system for full-scale, on-site aerodynamic investigations; and secondly the adoption of the system for different applications in speed sports. In total five experimental campaigns have been performed, three of them for development and assessment purposes and two for answering specific sport aerodynamics related research questions. The first part's findings provided practical criteria for performing Ring of Fire experiments in indoor facilities as well as outdoors. The aerodynamic drag accuracy has been determined based on a sensitivity analysis of the key parameters of the PIV technique and a linear error propagation. In the second part, the RoF was deployed to investigate drafting in cycling and aerodynamics of speed skating. The former led to the introduction of a mathematical expression that describes a model to predict the drag reduction under drafting conditions in cycling and the latter to the first aerodynamic assessment of a speed skater during its natural skating motion.

8.1. MEASUREMENT SYSTEM

8.1.1. FEASIBILITY AND FULL SCALE ASSESSMENT

Large-scale stereo-PIV measurements are conducted to determine the aerodynamic drag of a moving cyclist in indoor and outdoor on-site conditions using the control volume approach. The flow is measured in the wake of a cyclist moving at 5 m/s and 8 m/s for respectively the indoor and outdoor experiments. Instantaneous as well as ensemble average streamwise velocity fields have been obtained. Despite the differences between the two experiments in the cyclist geometry, bike model and the cycling speed, the flow fields in the near wake of the riders compare well between both experiments and to literature. The instantaneous and ensemble average aerodynamic drag is evaluated via a control volume approach along the wake behind the cyclist, taking into account the non-uniform flow conditions prior to the cyclist's passage. A clear distinction in upright vs. time-trial time ensemble average drag area is found for both experiments, with the upright posture yielding higher drag area by about 20-35% with respect to the time trial posture.

8.1.2. ASSESSMENT OF THE DRAG RESOLUTION

The drag resolution of the Ring of Fire is determined from measurements of the flow in the wake of a cyclist moving at 8.3 m/s. The single-passage and multi-passage average aerodynamic drag is evaluated via a control volume approach along the wake behind the cyclist, accounting for the non-uniform flow conditions prior to the cyclist's passage. A sensitivity analysis takes into account key parameters of the PIV technique, namely the interrogation window size and the control volume formulation, specifically determining the boundaries of the control volume. It is found that applying a dedicated wake contour and imposing the conservation of mass results in the most accurate drag measurements. Furthermore, the IW size should be within 0.05 c and 0.25 c , where c is the characteristic length scale representative for the wake topology. Finally, the drag values obtained with the RoF are compared against the drag estimates from simultaneously acquired power meter data. To assess the agreement between the two approaches in different regimes, three individual tests are performed where small drag variations due to different helmets as well as large drag variations due to different cyclist postures are produced. Regardless of the underlying input parameters in the power meter model, both small- and large scale deltas are well captured by both the Ring of Fire technique and the power meter approach and agree with available literature values (Barry et al., 2014; Blair et al., 2009; Spoelstra et al., 2019). The uncertainty on the average drag measurements from the RoF is within 5%. Although such value is considered rather coarse when compared with state-of-the-art force balance measurements conducted in a wind tunnel, it shows great potential for a range of other applications (drones, cars, trains, birds, ...) due to the possibility to determine the aerodynamic drag in-field rather than in the lab environment and simultaneously obtain flow visualization.

8.2. APPLICATIONS IN SPEED SPORTS

8.2.1. DRAFTING IN CYCLING

Ring of Fire experiments have been carried out to investigate the aerodynamics of cyclists riding at short distance from each other (drafting). The flow field visualizations show that the amount of drag reduction of the trailing rider should be mainly ascribed to the inflow conditions featuring a pronounced momentum deficit. Within the measured range of longitudinal separation, the drag reduction for the drafting cyclist ranges from 27% to 67%. The aerodynamic advantage, however, decreases as the lateral and longitudinal separation between riders is increased, where the lateral distance is found to produce a more rapid effect. A mathematical expression is proposed that describes a model introduced to predict the drag reduction under drafting conditions. Input from current experiments as well as from literature data returns a realistic prediction of the drag reduction in the near wake with an overestimation of the drag reduction at longitudinal distance between 0.1 m and 0.3 m.

Besides the above results, the RoF demonstrates its potential to investigate cyclists aerodynamics and also give an indication of the drafting skill level of cyclists, which is currently not practiced with the current state-of-the-art measurement techniques for cycling aerodynamics.

8.2.2. SPEED SKATING

In this chapter, the flow field in the wake of speed skaters in motion and their aerodynamic drag is measured using the Ring of Fire. A dedicated measurement setup was built on the 400 m track at Thialf in Heerenveen in the Netherlands. The skaters were skating through the Ring of Fire at a velocity of 11 m/s and the flow was measured before and after the passage of the skaters. Velocity fields in a plane orthogonal to gross skating direction, downstream of an elite skater are presented throughout the different phases of the skate stroke providing a better understanding of the overall skater aerodynamics. Furthermore, four different skating postures have been analysed with two different athletes. For the first athlete, the position of the arms was varied between both arms on the back and one arm swinging loose next to the body. The second athlete was swinging both arms loose for all the runs, but was varying his knee and trunk angles. For all the postures, an ensemble average streamwise velocity and vorticity field had been obtained. It was shown that in all cases the maximum velocity deficit in the wake was located behind the lower back and upper legs. Furthermore, the characteristic vortex pair in the wake of the skater model that was found by Puelles Magán et al. (2021), was also seen here for all different test cases, indicating it is independent of the athlete, posture, and skating phase.

The time ensemble average aerodynamic drag is evaluated via a control volume approach along the wake behind the skater, accounting for the non-uniform flow conditions prior to the skater's passage. The uncertainty on the average drag measurements from the RoF is about 5%. To evaluate whether the differences between the mean drag areas were statistically significant, a two-sample t-test was performed. This test indicated that, with the RoF system, there is no measurable difference in drag between skating with both your arms on the back or with just one arm on the back. For the other case,

skating with low trunk angle resulted in a drag reduction by 7.5% compared to skating with high trunk angle.

8.3. OUTLOOK

8.3.1. APPLICATION IN AUTOMOTIVE INDUSTRY

The Ring of Fire allowed to investigate the aerodynamic performance of individual cyclists (Chapters 4 and 5), drafting cyclists (Chapter 6), and speed skaters (Chapter 7). These studies have shown the potential of the system and a natural next step would be to apply it for automotive applications.

Aerodynamic investigations in the automotive industry are of paramount importance to reduce fuel consumption and for driver and passengers comfort among others. They generally consist of measurements of aerodynamic loads through wind tunnel experiments, CFD simulations, or track testing. The advantages and limitations of the use of these methods in cycling were discussed in Chapter 2 and are very similar for automotive aerodynamics.

An experimental campaign has been conducted in the autumn of 2020 to demonstrate the applicability of the Ring of Fire to automotive aerodynamics. Measurements were conducted at the test track of Volkswagen AG in Wolfsburg, Germany. A black painted VW-Up car equipped with 220 pressure taps, which is shown in Figure 8.1a, was used in the experiment. The test vehicle performed a series of tests at a constant velocity of 60 km/h. In this study Volkswagen AG was able to investigate the flow field in the region around the side-mirror, indicated as region 2 in Figure 8.1b. This location was chosen with the aim to show the potential of the Ring of Fire to visualize the local flow field around the car. Future experiments will also focus on the full wake of the car, depicted as region 1 in Figure 8.1b.

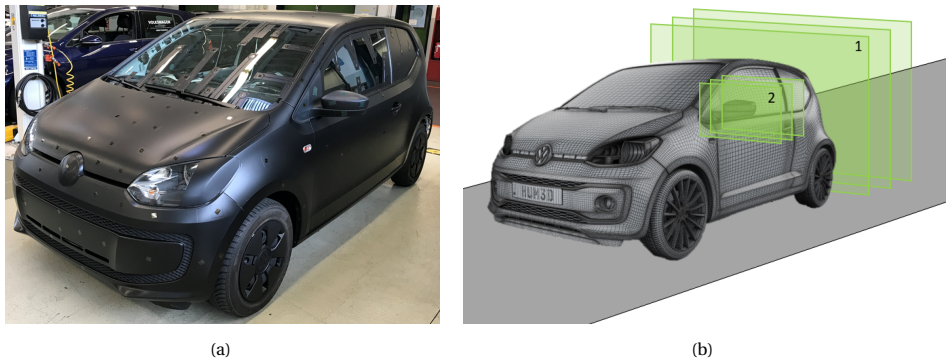


Figure 8.1: (a) Picture of the VW Up used during the experiment; (b) Schematic indication of the measurement regions.

Velocity measurements in both regions were acquired simultaneously with a large-scale stereoscopic-PIV system. Neutrally buoyant helium filled soap bubbles (HFSB) were used as tracer particles. They were introduced in the measurement area by two 100 nozzles LaVision seeding rakes. A LaVision HFSB fluid supply unit (FSU) controlled

soap, air and helium rates towards the seeding rakes. To contain these particles close to the measurement plane, fences were placed on the test track. A schematic of the setup is shown in Figure 8.2.

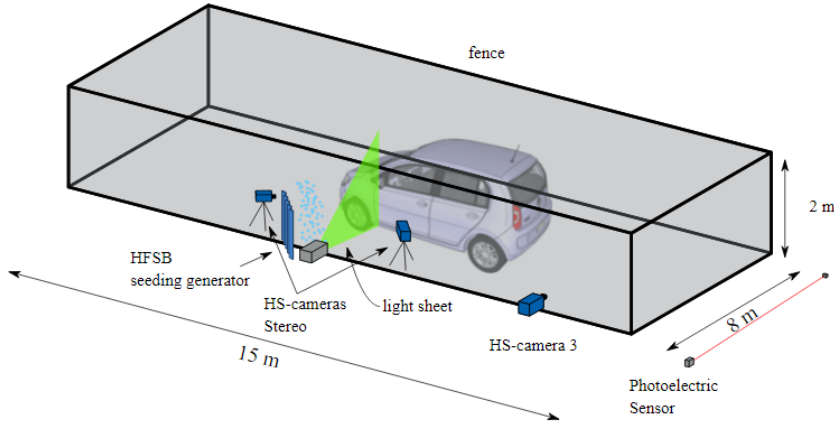


Figure 8.2: Schematic of the setup of the experiment at the VW proving ground in Wolfsburg.

The image acquisition is triggered by a photoelectric sensor and images were acquired at 6 kHz in continuous mode, which, at a car velocity of 60 km/h (16.67 m/s), corresponds to a measurement every 3 mm displacement of the car. The illumination was provided by a Hawk Pro 40-M laser, emitting a green light with a wavelength of 532 nm, a maximum pulse energy of 6 mJ, at repetition rate of 6 kHz. Two Photron FastCAM SA-X2 cameras (1024 × 1024 pixels, 12 bit, pixel pitch 20 μm), positioned at opposite sides of the laser sheet, were used to capture the flow field. The cameras were equipped with a Nikon Nikkor AF 60 mm objective at an $f_{\#} = 4$, yielding a field of view of $0.8 \times 0.8 \text{ m}^2$, a magnification factor $M = 0.031$, and a digital imaging resolution of 0.78 mm/px.

The recorded images are analysed with the LaVision DaVis 8 software. The pre-processing removes background light by subtracting the minimum intensity over time at each pixel. The recordings are analysed with a sliding sum of correlation algorithm (Sciaccitano et al., 2012). The analysis performs an average of the correlation map from 10 frames sliding a time interval of 1.7 ms. The final interrogation window size is chosen to be 48×48 pixels and the overlap factor is set to 75%. Figure 8.3 presents the streamwise velocity field behind the side-mirror. These results show the capabilities of the RoF to investigate and quantify the flow structures around the side-mirror of the vehicle under Real Driving Conditions. Some clear features in the wake of the side-mirror can already be distinguished, such as the strong up-wash behind the center of the side-mirror.

Further analysis of all the results will show if these type of measurements can potentially function as a new benchmark or reference for validation of CFD simulations in the automotive industry. In addition, following the momentum balance approach described in Sections 3.4.1 and 4.2, the drag of the vehicle can be calculated and compared to wind tunnel and track measurements.

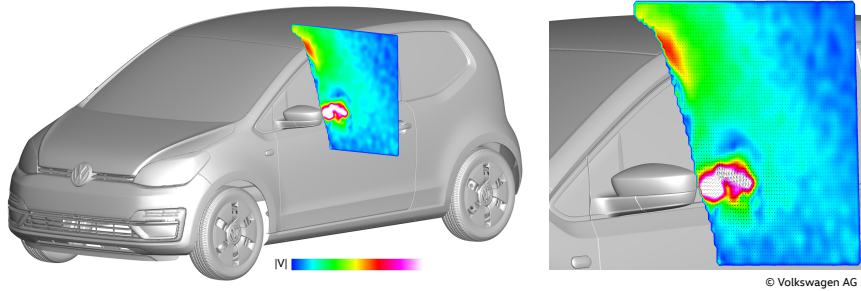


Figure 8.3: Streamwise velocity component behind the side-mirror.

8.3.2. FUTURE PROSPECTS

Finalising this booklet it might be interesting to contemplate on the future of the Ring of Fire system. The extent to which future applications will make use of the Ring of Fire is difficult to predict, but its broad applicability and the fact that it is based on common PIV processing both work in its favour. Applications one could think of, besides the ones already presented, can be the visualization of vortices in F1 under Real Driving Conditions, study of the free flight of drones or the Delfly (Martínez Gallar et al., 2019), and take-off and landing of airplanes, among others. Whether the Ring of Fire will ever become mainstream for such applications is by no means certain, especially if one considers that the application of PIV is far from industry standard. In addition, the wide-spread adoption of the Ring of Fire in industry is currently also hampered by other factors, arising mainly from limitations of the hardware:

- Slow data transfer from cameras to PC do not allow for continuous measurements. Use of state-of-the-art cameras could solve this.
- The current seeding system is optimised for use in a wind tunnel. The compact, aerodynamic shape of the system is not beneficial for homogeneous seeding in the tunnel. A more distributed seeding system can lead to more homogeneous seeding.
- High power lasers are expensive and need experience to operate safely. Use of LED for illumination could be more cost efficient.

Nevertheless, I am excited to see the potential of the Ring of Fire being exploited in industry and to see on-site flow visualizations and drag measurements for applications where this was not possible before, thus enabling new insights and better validation of numerical simulations.

A

ENERGIZED MASS CONCEPT FOR DRAG DETERMINATION

Drag determination with the Ring of Fire by applying the momentum balance in a control volume has been proven to produce satisfying results. In order to apply this method, however, the user needs to be experienced with setting up and performing PIV measurements. When only on-site drag determination is of interest, one alternative to the momentum balance approach that shows promise in delivering a more user-friendly solution is the energized mass concept, as discussed and tested on an accelerating sphere by (Galler et al., 2021).

The energized mass approach is based on the principle of conservation of energy. Considering a body moving in a fluid, the drag force on the body is the mechanism by which the body can modify the kinetic energy of the fluid. In other words, any change in the kinetic energy of the fluid is caused by the work done by the body on the fluid, through the drag force.

In the case of a fluid at rest where a body is moving, this means that any kinetic energy in the fluid is caused by the drag force of the body. The energized mass comprises all of the fluid that has undergone a change in kinetic energy, and includes a measure of the normalized kinetic energy of the fluid:

$$m_e = \rho \iiint_V \frac{u^2 + v^2 + w^2}{U^2} dV \quad (\text{A.1})$$

where m_e is the energized mass, U is the body velocity, and u , v , w are the velocity components of the fluid. The control volume over which the integral is taken would comprise the entire volume of fluid that has experienced a change in kinetic energy. Within the above framework the work done by the object to the fluid is equal to the time derivative of kinetic energy in the fluid:

$$F_D U = \frac{dK}{dt} = \frac{d}{dt} \iiint_V \left[\frac{1}{2} \rho (u^2 + v^2 + w^2) dV \right] \quad (\text{A.2})$$

A

Hence, the drag force is:

$$F_D = \frac{\rho}{2U} \frac{d}{dt} \iiint_V [(u^2 + v^2 + w^2) dV] \quad (\text{A.3})$$

The variation of kinetic energy can be assumed to be due to an additional mass of fluid dm_e (corresponding to an additional volume of fluid dV_e) moving at the fluid velocity U , and can thus also be expressed as:

$$\frac{dK}{dt} = \frac{1}{2} \rho U^2 \frac{\Delta V_e}{\Delta t} \quad (\text{A.4})$$

Assuming no mixing normal to the axis of motion, this volume of affected fluid can be thought of as nothing more than volume stretching out along the axis of motion of the body, with cross-sectional area A_w , and length l :

$$\frac{\Delta V_e}{\Delta t} = \frac{\Delta(A_w l)}{\Delta t} = A_w U \quad (\text{A.5})$$

Combining Equations A.2, A.4, and A.5 the expression of the drag force becomes:

$$F_D = \frac{1}{2} \rho U^2 A_w \quad (\text{A.6})$$

Measuring A_w would directly result in the object's drag; however, in order to do so, one would need to perform time-resolved volumetric measurements all around the object:

$$A_w = \frac{1}{U^3} \frac{d}{dt} \iiint_V [(u^2 + v^2 + w^2) dV] \quad (\text{A.7})$$

These type of measurements are often not available and hence, A_w needs to be estimated based on its physical meaning (again, A_w is the wake area; $A_w U$ is the volume of fluid per unit time energized by the object). The estimated could, for example, be obtained by linear interpolation of a measured area $A_m(x)$ at a distance x from the object:

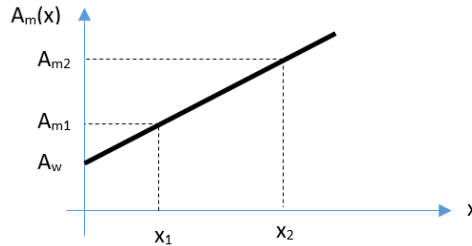


Figure A.1: Linear interpolation of $A_m(x)$ to obtain A_w .

$$A_m(x) = \frac{A_{m2} - A_{m1}}{x_2 - x_1} x + A_w \quad (\text{A.8})$$

Hence, the drag force can also be expressed in terms of A_m :

$$F_D = \frac{1}{2}\rho U^2 A_w = \frac{1}{2}\rho U^2 \left(A_m(x) - \frac{A_{m2} - A_{m1}}{x_2 - x_1} x \right) \quad (\text{A.9})$$

where the second term in parenthesis accounts for the flow entrainment occurring in the wake. Applying the energized mass methodology would make it possible to derive information about the drag of an object based on its wake development only, without requiring detailed velocity fields upstream and downstream of the body. One camera perpendicular to the measurement plane in theory would be sufficient to track the wake size development and no knowledge about PIV would be needed.



REFERENCES

- Adrian (1997). Dynamic ranges of velocity and spatial resolution of particle image velocimetry. *Measurement Science and Technology*, 8(12):1393–1398.
- Adrian and Westerweel (2011). *Particle Image Velocimetry*. Cambridge University Press.
- Allen, M. (1982). Image mark allen.
- Anderson, J. D. (2011). *Fundamentals of aerodynamics*. McGraw-Hill.
- Andrews, E. (2021). The bicycle's bumpy history.
- Baldissera, P. and Delprete, C. (2016). Rolling resistance, vertical load and optimal number of wheels in human-powered vehicle design. *Proceedings of the Institution of Mechanical Engineers, Part P: Journal of Sports Engineering and Technology*, 231(1):33–42.
- Barlow, J. B., Rae, W. H., Pope, A., and Pope, A. (1999). *Low-speed wind tunnel testing*. Wiley, New York.
- Barry, N. (2015). *Aerodynamic Interactions Between Multiple Cyclists*. Thesis.
- Barry, N., Burton, D., Sheridan, J., Thompson, M., and Brown, N. A. (2015a). Aerodynamic performance and riding posture in road cycling and triathlon. *Proceedings of the Institution of Mechanical Engineers, Part P: Journal of Sports Engineering and Technology*, 229(1):28–38.
- Barry, N., Burton, D., Sheridan, J., Thompson, M., and Brown, N. A. T. (2015b). Aerodynamic drag interactions between cyclists in a team pursuit. *Sports Engineering*, 18(2):93–103.
- Barry, N., Burton, D., Sheridan, J., Thompson, M., and Brown, N. A. T. (2016a). flow field interactions between two tandem cyclists. *Experiments in Fluids*, 57(12).
- Barry, N., Burton, D., Sheridan, J., Thompson, M., and Brown, N. A. T. (2016b). an analysis of the wake of pedalling cyclists in a tandem formation. In *Procedia Engineering*, volume 147, pages 7–12.
- Barry, N., Sheridan, J., Burton, D., and Brown, N. A. (2014). The effect of spatial position on the aerodynamic interactions between cyclists. *Procedia Engineering*, 72:774 – 779. The Engineering of Sport 10.
- Bassett, D. R., J., Kyle, C. R., Passfield, L., Broker, J. P., and Burke, E. R. (1999). Comparing cycling world hour records, 1967-1996: modeling with empirical data. *Med Sci Sports Exerc*, 31(11):1665–76.

- Beaumont, F., Taiar, R., Polidori, G., Trenchard, H., and Grappe, F. (2018). Aerodynamic study of time-trial helmets in cycling racing using cfd analysis. *Journal of Biomechanics*, 67:1–8.
- Belloli, M., Giappino, S., Robustelli, F., and Somaschini, C. (2016). Drafting effect in cycling: Investigation by wind tunnel tests. *Procedia Engineering*, 147:38 – 43. The Engineering of SPORT 11.
- Bertucci, W., Duc, S., Villerius, V., Pernin, J. N., and Grappe, F. (2005). Validity and reliability of the powertap mobile cycling powermeter when compared with the srm device. *Int J Sports Med*, 26(10):868–873.
- Bierman, J. (2016). Bicycle rolling resistance: Rolling resistance tests.
- Blair, K., Sidelko, S., and Estivalet, M. (2009). *Aerodynamic Performance Of Cycling Time Trial Helmets (P76)*, pages 371–377.
- Blocken, B., Defraeye, T., Koninckx, E., Carmeliet, J., and Hespel, P. (2011). Numerical study of the interference drag of two cyclists. In *Proceedings of the 13th International Conference on Wind Engineering (ICWE13), 10-15 July 2011, Amsterdam, The Netherlands*, pages 1–8.
- Blocken, B., Defraeye, T., Koninckx, E., Carmeliet, J., and Hespel, P. (2013). Cfd simulations of the aerodynamic drag of two drafting cyclists. *Computers and Fluids*, 71:435–445.
- Blocken, B., Toparlar, Y., and Andrianne, T. (2016). Aerodynamic benefit for a cyclist by a following motorcycle. *Journal of Wind Engineering and Industrial Aerodynamics*, 155:1–10.
- Blocken, B., Toparlar, Y., van Druenen, T., and Andrianne, T. (2018). Aerodynamic drag in cycling team time trials. *Journal of Wind Engineering and Industrial Aerodynamics*, 182:128–145.
- Bosbach, J., Kühn, M., and Wagner, C. (2009). Large scale particle image velocimetry with helium filled soap bubbles. *J Experiments in Fluids*, 46(3):539–547.
- Broker, J. P. and Kyle, C. R. (1995). Pursuit aerodynamics, project 96: Wind tunnel test results. *USOC Sport Science and Technology Report*, pages 1–46.
- Broker, J. P., Kyle, C. R., and Burke, E. R. (1999). Racing cyclist power requirements in the 4000-m individual and team pursuits. *Medicine and Science in Sports and Exercise*, 31(11):1677–1685.
- Brownlie, L., Aihara, Y., Carbo, J., Harber, E., Henry, R., Ilcheva, I., and Ostafichuk, P. (2016). The use of vortex generators to reduce the aerodynamic drag of athletic apparel. *Procedia Engineering*, 147:20–25.
- Buckley, F. T. (1995). Abcd - an improved coast down test and analysis method. *SAE Transactions*, 104:1136–1148.

- Burke, E. R. (2003). *High tech cycling the science of riding faster*. Human Kinetics, Champaign, Ill.; Leeds.
- Candau, R., Grappe, F., Ménard, M., BARBIER, B., Millet, G., Hoffman, M., Belli, A., and ROUILLON, J. (1999). Simplified deceleration method for assessment of resistive forces in cycling. *Medicine and science in sports and exercise*, 31:1441–7.
- Capelli, C., Rosa, G., Butti, F., Ferretti, G., Veicsteinas, A., and Prampero, P. (1993). Energy cost and efficiency of riding aerodynamic bicycles. *European journal of applied physiology and occupational physiology*, 67:144–9.
- Caridi, G. (2018). *Development and application of helium-filled soap bubbles*. PhD thesis, Repository TU Delft.
- Caridi, G. C. A., Ragni, D., Sciacchitano, A., and Scarano, F. (2016). Hfsb-seeding for large-scale tomographic piv in wind tunnels. *Experiments in Fluids*, 57(12):190.
- Celis, B. and Ubbens, H. H. (2016). Design and construction of an open-circuit wind tunnel with specific measurement equipment for cycling. *Procedia Engineering*, 147:98–103. The Engineering of SPORT 11.
- Chabroux, V., Mba, M. N., Sainton, P., and Favier, D. (2010). Wake characteristics of time trial helmets using piv-3 c technique. In *Proceedings of the 15th international symposium on application of laser and imaging techniques to fluid mechanics, Lisbon*.
- Chowdhury, H. and Alam, F. (2012). Bicycle aerodynamics: An experimental evaluation methodology. *Sports Engineering*, 15.
- Crouch, T., Sheridan, J., Burton, D., Thompson, M., and Brown, N. A. (2012). A quasi-static investigation of the effect of leg position on cyclist aerodynamic drag. *Procedia Engineering*, 34:3–8. ENGINEERING OF SPORT CONFERENCE 2012.
- Crouch, T. N., Burton, D., Brown, N. A. T., Thompson, M. C., and Sheridan, J. (2014). Flow topology in the wake of a cyclist and its effect on aerodynamic drag. *Journal of Fluid Mechanics*, 748:5–35.
- Crouch, T. N., Burton, D., LaBry, Z. A., and Blair, K. B. (2017). Riding against the wind: a review of competition cycling aerodynamics. *Sports Engineering*, 20(2):81–110.
- Crouch, T. N., Burton, D., Thompson, M. C., Brown, N. A. T., and Sheridan, J. (2016). Dynamic leg-motion and its effect on the aerodynamic performance of cyclists. *Journal of Fluids and Structures*, 65:121–137.
- Dantec Dynamics (2021). Measurement principles of piv.
- D'Auteuil, A., Larose, G. L., and Zan, S. J. (2012). Wind turbulence in speed skating: Measurement, simulation and its effect on aerodynamic drag. *Journal of Wind Engineering and Industrial Aerodynamics*, 104-106:585–593. 13th International Conference on Wind Engineering.

- Davies, C. T. M. (1980). Effect of air resistance on the metabolic cost and performance of cycling. *European Journal of Applied Physiology and Occupational Physiology*, 45(2):245–254.
- de Groot, G., Sargeant, A., and Geysel, J. (1995). Air friction and rolling resistance during cycling. *Medicine and science in sports and exercise*, 27(7):1090–1095.
- De Kat, R. and Bleischwitz, R. (2016). Towards instantaneous lift and drag from stereo-piv wake measurements. In *Proceedings of the 18th international symposium on application of laser and imaging techniques to fluid mechanics, Lisbon*.
- de Martino Norante, L. (2018). *Advances and assessment of the Ring of Fire concept for on-site cycling aerodynamics*. PhD thesis.
- Debraux, P., Grappe, F., Manolova, A. V., and Bertucci, W. (2011). Aerodynamic drag in cycling: methods of assessment. *Sports Biomechanics*, 10(3):197–218.
- Defraeye, T., Blocken, B., Koninckx, E., Hespel, P., and Carmeliet, J. (2010a). Aerodynamic study of different cyclist positions: Cfd analysis and full-scale wind-tunnel tests. *Journal of Biomechanics*, 43(7):1262 – 1268.
- Defraeye, T., Blocken, B., Koninckx, E., Hespel, P., and Carmeliet, J. (2010b). Computational fluid dynamics analysis of cyclist aerodynamics: Performance of different turbulence-modelling and boundary-layer modelling approaches. *Journal of Biomechanics*, 43(12):2281–2287.
- Defraeye, T., Blocken, B., Koninckx, E., Hespel, P., Verboven, P., Nicolai, B., and Carmeliet, J. (2014). Cyclist drag in team pursuit: Influence of cyclist sequence, stature, and arm spacing. *Journal of Biomechanical Engineering*, 136(1).
- di Prampero, P. E., Cortili, G., Mognoni, P., and Saibene, F. (1979). Equation of motion of a cyclist. *Journal of Applied Physiology*, 47(1):201–206. PMID: 468661.
- Dirksen, F. (2019). Swiss side launches new aero technologies with patrick lange and laura philipp.
- Duc, S., Villerius, V., William, B., and Grappe, F. (2007). Validity and reproducibility of the ergomo@pro power meter compared with the srm and powertap power meters. *International journal of sports physiology and performance*, 2:270–81.
- Duncan, C. (2017). Master your bike position: Stac’s virtual wind tunnel technology.
- Edwards, A. G. and Byrnes, W. C. (2007). Aerodynamic characteristics as determinants of the drafting effect in cycling. *Medicine and Science in Sports and Exercise*, 39(1):170–176.
- Faleiros, D. E., Tuinstra, M., Sciacchitano, A., and Scarano, F. (2018). Helium-filled soap bubbles tracing fidelity in wall-bounded turbulence. *Experiments in Fluids*, 59(3):56.
- Faleiros, D. E., Tuinstra, M., Sciacchitano, A., and Scarano, F. (2019). Generation and control of helium-filled soap bubbles for piv. *Experiments in Fluids*, 60(3):40.

- Fitton, B., Caddy, O., and Symons, D. (2018). The impact of relative athlete characteristics on the drag reductions caused by drafting when cycling in a velodrome. *Proceedings of the Institution of Mechanical Engineers, Part P: Journal of Sports Engineering and Technology*, 232(1):39–49.
- Fitzgerald, S., Kelso, R., Grimshaw, P., and Warr, A. (2019). Measurement of the air velocity and turbulence in a simulated track cycling team pursuit race. *Journal of Wind Engineering and Industrial Aerodynamics*, 190:322–330.
- Galler, J. N., Weymouth, G. D., and Rival, D. E. (2021). On the concept of energized mass: A robust framework for low-order force modeling in flow past accelerating bodies. *Physics of Fluids*, 33(5):057103.
- García-López, J., Rodríguez-Marroyo, J. A., Juneau, C.-E., Peleteiro, J., Martínez, A. C., and Villa, J. G. (2008). Reference values and improvement of aerodynamic drag in professional cyclists. *Journal of Sports Sciences*, 26(3):277–286.
- Gardan, N., Schneider, A., Polidori, G., Trenchard, H., Seigneur, J., Beaumont, F., Fourchet, F., and Taiar, R. (2017). Numerical investigation of the early flight phase in ski-jumping. *Journal of Biomechanics*, 59:29–34.
- Gibeau, B., Gingras, D., and Ghaemi, S. (2020). Evaluation of a full-scale helium-filled soap bubble generator. *Experiments in Fluids*, 61(2):28.
- Gibertini, G. and Grassi, D. (2008). *Cycling Aerodynamics*, volume 506 of *CISM International Centre for Mechanical Sciences*, pages 23–47. Springer, Vienna.
- Godo, M., Corson, D., and Legensky, S. (2009). *An Aerodynamic Study of Bicycle Wheel Performance Using CFD*.
- Grappe, F. (2009). *Resistance totale qui s'oppose au déplacement en cyclisme [Total resistive forces opposed to the motion in cycling]*, page 604. De Boeck Université, Collection Science et Pratique du Sport, 2 edition.
- Grappe, F., Candau, R., Belli, A., and Rouillon, J. D. (1997). Aerodynamic drag in field cycling with special reference to the obree's position. *Ergonomics*, 40(12):1299–1311.
- Griffith, M., Crouch, T., Thompson, M., Burton, D., Sheridan, J., and Brown, N. (2014). Computational fluid dynamics study of the effect of leg position on cyclist aerodynamic drag. *Journal of Fluids Engineering*, 136:101105.
- Hanna, R. K. (2012). Cfd in sport - a retrospective; 1992 - 2012. *Procedia Engineering*, 34:622–627. ENGINEERING OF SPORT CONFERENCE 2012.
- Heijmans, J. and Mallon, B. (2011). *Historical dictionary of cycling*. Scarecrow Press, Inc.
- Hilger, M. (2018). Image patrick lange aerobar scan.
- Hill, H. (2006). Image norman stadlet.

- Hill, R. D. (1993). The design and development of the lotussport pursuit bicycle. *Proceedings of the Institution of Mechanical Engineers, Part D: Journal of Automobile Engineering*, 207(4):285–294.
- Hirsch, M. (2018). *Accuracy assessment of the Ring of Fire system for on-site aerodynamic drag measurements*. PhD thesis.
- Huhn, F., Schanz, D., Gesemann, S., Dierksheide, U., van de Meerendonk, R., and Schröder, A. (2017). Large-scale volumetric flow measurement in a pure thermal plume by dense tracking of helium-filled soap bubbles. *Experiments in Fluids*, 58(9):116.
- Huizinga, A. (2020). De tour van 1989: hoe donald trump een handje hielp met de zege van lemond.
- Íñiguez De-La Torre, A. and Íñiguez, J. (2009). Aerodynamics of a cycling team in a time trial: Does the cyclist at the front benefit? *European Journal of Physics*, 30(6):1365–1369.
- Jeukendrup, A. and Martin, J. (2001). Improving cycling performance: How should we spend our time and money. *Sports medicine (Auckland, N.Z.)*, 31:559–69.
- Jones, B. (1936). Measurement of profile drag by the pitot-traverse method. *ARC R&M*, 1688.
- Jux, C., Sciacchitano, A., and Scarano, F. (2020). Flow pressure evaluation on generic surfaces by robotic volumetric ptv. *Measurement Science and Technology*, 31(10):104001.
- Jux, C., Sciacchitano, A., Schneiders, J. F. G., and Scarano, F. (2018). Robotic volumetric piv of a full-scale cyclist. *Experiments in Fluids*, 59(4):74.
- Kawamura, T. (1953). Wind drag of bicycles. (Report No.1, Tokyo University).
- Keane, R. D. and Adrian, R. J. (1992). Theory of cross-correlation analysis of piv images. *Applied Scientific Research*, 49(3):191–215.
- Kühn, M., Ehrenfried, K., Bosbach, J., and Wagner, C. (2011). Large-scale tomographic particle image velocimetry using helium-filled soap bubbles. *Experiments in Fluids*, 50(4):929–948.
- Kordi, M., Galis, G., van Erp, T., and Terra, W. (2021). Reliability and sensitivity of the nio konekt to quantify coefficient of drag area in elite track cyclists. *European Journal of Sport Science*, 0(0):1–6. PMID: 33590804.
- Kurtulus, D. F., Scarano, F., and David, L. (2007). Unsteady aerodynamic forces estimation on a square cylinder by tr-piv. *Experiments in Fluids*, 42(2):185–196.
- Kyle, C. (1991). The effect of crosswinds upon time trials. *Cycling Sci*, 3(3-4):51–6.
- Kyle, C. R. (1979). Reduction of wind resistance and power output of racing cyclists and runners travelling in groups. *Ergonomics*, 22(4):387–397.

- Kyle, C. R. (1989). The aerodynamics of helmets and handlebars. *Cycling Science*, 1(1):122–125.
- Kyle, C. R. (2001). The mechanical efficiency of bicycle derailleur and hub gear transmissions. *Human Power*, 52:3.
- Kyle, C. R. and Burke, E. (1984). Improving the racing bicycle. *Mechanical Engineering*, 106(9):34–35.
- Lavision Gmbh (2018). Product-manual flow master // advanced piv/ptv systems for quantitative flow field analysis.
- Lim, A. C., Homestead, E. P., Edwards, A. G., Carver, T. C., Kram, R., and Byrnes, W. C. (2011). Measuring changes in aerodynamic/rolling resistances by cycle-mounted power meters. *Medicine and science in sports and exercise*, 43(5):853–860.
- Lukes, R., Hart, J., and Haake, S. (2012). An analytical model for track cycling. *Proceedings of the Institution of Mechanical Engineers, Part P: Journal of Sports Engineering and Technology*, 226(2):143–151.
- Lukes, R. A., Chin, S. B., and Haake, S. J. (2005). The understanding and development of cycling aerodynamics. *Sports Engineering*, 8(2):59–74.
- Martin, J., Gardner, A., Barras, M., and Martin, D. (2006). Modeling sprint cycling using field-derived parameters and forward integration. *Medicine and science in sports and exercise*, 38:592–7.
- Martin, J., Milliken, D., Cobb, J., McFadden, K., and Coggan, A. (1998). Validation of a mathematical model for road cycling power. *Journal of Applied Biomechanics*, 14:276–291.
- Martínez Gallar, B., van Oudheusden, B. W., Sciacchitano, A., and Karásek, M. (2019). Large-scale volumetric flow visualization of the unsteady wake of a flapping-wing micro air vehicle. *Experiments in Fluids*, 61(1):16.
- Mertens, C., de Rojas Cordero, T., Sodja, J., Sciacchitano, A., and van Oudheusden, B. W. (2021). Aeroelastic characterization of a flexible wing using particle tracking velocimetry measurements. *AIAA Journal*, 0(0):1–11.
- Mohebbian, A. and Rival, D. (2012). Assessment of the derivative-moment transformation method for unsteady-load estimation. *Experiments in Fluids*, 53.
- Mylaps (2021). Prochip system.
- Nonweiler, T. (1956). The air resistance of racing cyclists. *Technical report, College of Aeronautics Cranfield*.
- Nonweiler, T. (1958). The work production of manstudies on racing cyclists. *Journal of Physiology London*, 141:8–9.

- Oggiano, L. and Sætran, L. (2008). Effect of different skin suits on speed skating performances. *Computer Science in Sports*, 3:139–144.
- Oggiano, L. and Sætran, L. R. (2010). Experimental analysis on parameters affecting drag force on speed skaters. *Sports Technology*, 3(4):223–234.
- Okuno, Y., Fukuda, T., Miwate, Y., and Kobayashi, T. (1993). Development of three dimensional air flow measuring method using soap bubbles. *JSAE Rev*, 14(4):50–55.
- Olds, T. (1998). The mathematics of breaking away and chasing in cycling. *European Journal of Applied Physiology and Occupational Physiology*, 77(6):492–497.
- Olds, T. (2001). Modelling human locomotion. *Sports Medicine*, 31(7):497–509.
- Padilla, S., Mujika, I., Angulo, F., and Goiriena, J. (2000). Scientific approach to the 1-h cycling world record: A case study. *Journal of applied physiology (Bethesda, Md. : 1985)*, 89:1522–7.
- Passfield, L., Hopker, J. G., Jobson, S., Friel, D., and Zabala, M. (2017). Knowledge is power: Issues of measuring training and performance in cycling. *Journal of Sports Sciences*, 35(14):1426–1434.
- Petrushov, V. A. (1998). Improvement in vehicle aerodynamic drag and rolling resistance determination from coast-down tests. *Proceedings of the Institution of Mechanical Engineers, Part D: Journal of Automobile Engineering*, 212(5):369–380.
- Pope, S. B. (2000). *Turbulent Flows*. Cambridge University Press, Cambridge.
- Prasad (2000). Stereoscopic particle image velocimetry. *Experiments in Fluids*, 29(2):103–116.
- Páscoa, J., Brojo, F., Charrua Santos, F., and Fael, P. (2012). An innovative experimental on-road testing method and its demonstration on a prototype vehicle. *Journal of Mechanical Science and Technology*, 26.
- Puelles Magán, G., Terra, W., and Sciacchitano, A. (2021). Aerodynamics analysis of speed skating helmets: Investigation by cfd simulations. *Applied Sciences*, 11(7).
- Pugh, L. G. (1974). The relation of oxygen intake and speed in competition cycling and comparative observations on the bicycle ergometer. *J Physiol*, 241(3):795–808.
- Raffel, M., Willert, C. E., Scarano, F., Kähler, C. J., Wereley, S. T., and Kompenhans, J. (2018). *Particle image velocimetry: a practical guide*. Springer.
- Rauschendorfer, M. (2017). Image sebastian kienle.
- Rauschendorfer, M. (2018). Image patrick lange with new cockpit.
- Revolver (2021). Aerodynamic performance data.
- Samimy, M. and Lele, S. K. (1991). Motion of particles with inertia in a compressible free shear layer. *Physics of Fluids A: Fluid Dynamics*, 3(8):1915–1923.

- Scarano, F. (2001). Iterative image deformation methods in piv. *Measurement Science and Technology*, 13(1):R1–R19.
- Scarano, F., Ghaemi, S., Caridi, G. C. A., Bosbach, J., Dierksheide, U., and Sciacchitano, A. (2015). On the use of helium-filled soap bubbles for large-scale tomographic piv in wind tunnel experiments. *Experiments in Fluids*, 56(2):42.
- Scarano, F. and Riethmuller, M. L. (2000). Advances in iterative multigrid piv image processing. *Experiments in Fluids*, 29(1):S051–S060.
- Schneiders, J. F. G., Caridi, G. C. A., Sciacchitano, A., and Scarano, F. (2016). Large-scale volumetric pressure from tomographic pvt with hfsb tracers. *Experiments in Fluids*, 57(11):164.
- Sciacchitano, A. (2019). Uncertainty quantification in particle image velocimetry. *Measurement Science and Technology*, 30(9):092001.
- Sciacchitano, A., Caridi, G. C. A., and Scarano, F. (2015). A quantitative flow visualization technique for on-site sport aerodynamics optimization. *Procedia Engineering*, 112:412–417. 'The Impact of Technology on Sport VI' 7th Asia-Pacific Congress on Sports Technology, APCST2015.
- Sciacchitano, A., Scarano, F., and Wieneke, B. (2012). Multi-frame pyramid correlation for time-resolved piv. *Experiments in Fluids*, 53(4):1087–1105.
- Sciacchitano, A., Wieneke, B., and Scarano, F. (2013). Piv uncertainty quantification by image matching. *Measurement Science and Technology*, 24(4):045302.
- Sharp, A. (1896). *Bicycle and Tricycles*. Longmans, Green, and Co.
- Snedecor, G. W. and Cochran, W. G. (1996). *Statistical methods*. Iowa State Univ. Press, Ames, Iowa, 8 ed., 7. print edition.
- Spicer, J., Richardson, C., Ehrlich, M., Bernstein, J., Fukuda, M., and Terada, M. (2001). Effects of frictional loss on bicycle chain drive efficiency. *Journal of Mechanical Design - JMECH DESIGN*, 123.
- Spoelstra, A., de Martino Norante, L., Terra, W., Sciacchitano, A., and Scarano, F. (2019). On-site cycling drag analysis with the ring of fire. *Experiments in Fluids*, 60(6):90.
- Spoelstra, A., Hirsch, M., Sciacchitano, A., and Scarano, F. (2021). Uncertainty assessment of the ring of fire concept for on-site aerodynamic drag evaluation. *Measurement Science and Technology*, 32(4):044004.
- Terra, W. (2020). *Cyclist Aerodynamic Drag Analysis through Large-Scale PIV*. TU Delft.
- Terra, W., Sciacchitano, A., and Scarano, F. (2016). Drag analysis from piv data in speed sports. *Procedia Engineering*, 147:50–55.
- Terra, W., Sciacchitano, A., and Scarano, F. (2017). Aerodynamic drag of a transiting sphere by large-scale tomographic-piv. *Experiments in Fluids*, 58(7):83.

- Terra, W., Sciacchitano, A., and Scarano, F. (2020). Cyclist Reynolds number effects and drag crisis distribution. *Journal of Wind Engineering and Industrial Aerodynamics*, 200:104143.
- Terra, W., Sciacchitano, A., Scarano, F., and van Oudheusden, B. W. (2018). Drag resolution of a piv wake rake for transiting models. *Experiments in Fluids*, 59(7):120.
- Terra, W., Sciacchitano, A., and Shah, Y. H. (2019). Aerodynamic drag determination of a full-scale cyclist mannequin from large-scale pTV measurements. *Experiments in Fluids*, 60(2):29.
- Thialf (2021). Ijsfaciliteiten.
- Timmer, N. and Veldhuis, L. (2021). The impact of skinsuit zigzag tape turbulators on speed skating performance. *Applied Sciences*, 11(3).
- Tropea, C., Yarin, A., and Foss, J. F. (2016). *Springer Handbook of Experimental Fluid Mechanics*. Springer Berlin.
- Unal, M., Lin, J., and Rockwell, D. (1997). Force prediction by piv imaging: A momentum-based approach. *Journal of Fluids and Structures*, 11:965–971.
- Underwood, L. (2012). *Aerodynamics of Track Cycling*. Thesis.
- Underwood, L., Schumacher, J., Burette-Pommay, J., and Jermy, M. (2011). Aerodynamic drag and biomechanical power of a track cyclist as a function of shoulder and torso angles. *Sports Engineering*, 14.
- Van der Kruk, E. (2018). *Parameter analysis for speed skating performance*. Phd thesis.
- van Ingen Schenau, G. (1982). The influence of air friction in speed skating. *Journal of Biomechanics*, 15(6):449–458.
- van Oudheusden, B. W. (2013). Piv-based pressure measurement. *Measurement Science and Technology*, 24(3):032001.
- van Oudheusden, B. W., Scarano, F., Roosenboom, E. W. M., Casimiri, E. W. F., and Souverein, L. J. (2007). Evaluation of integral forces and pressure fields from planar velocimetry data for incompressible and compressible flows. *Experiments in Fluids*, 43(2):153–162.
- Westerweel, J. (1993). Digital particle image velocimetry - theory and application.
- Westerweel, J. and Scarano, F. (2005). Universal outlier detection for piv data. *Experiments in Fluids*, 39(6):1096–1100.
- Wilcox, D. C. (2008). Formulation of the k-w turbulence model revisited. *AIAA Journal*, 46(11):2823–2838.
- Wilson, D. G., Papadopoulos, J., and Whitt, F. R. (2004). *Bicycling science*. MIT Press, Cambridge, Mass.

- Yu, C. and Yao, W. (2017). Robust linear regression: A review and comparison. *Communications in Statistics - Simulation and Computation*, 46(8):6261–6282.
- Zaman, K. and Hussain, F. (1981). Taylor hypothesis and large-scale coherent structures. *Journal of Fluid Mechanics*, 112:379 – 396.
- Zdravkovich, M. (1996). *Effect of cyclist's posture and vicinity of another cyclist on aerodynamic drag*. Balkema, Rotterdam.
- Zdravkovich, M. M. (1990). Conceptual overview of laminar and turbulent flows past smooth and rough circular cylinders. *Journal of Wind Engineering and Industrial Aerodynamics*, 33(1):53–62.



ACKNOWLEDGEMENTS

*If I have seen further, it is by standing
upon the shoulders of Giants.*

Sir Isaac Newton

The realization of this PhD has been a challenging but rewarding task. It has been a fantastic journey. I consider myself extremely fortunate with the support I have had over the years and I would like to express my gratitude to several people who have contributed to this work.

First and foremost, I would like to express my sincere gratitude to my promotor Prof. dr. Fulvio Scarano, for his support and sharp supervision throughout the course of my PhD research. Fulvio, your creative thinking and scientific rigor have been instrumental in my formation as a researcher. Your valuable comments brought my papers and dissertation to a higher level, and your professional knowledge and experience in aerodynamics and PIV helped me complete the most challenging parts of my research.

I would like to equally thank my co-promotor Dr. Andrea Sciacchitano, who has been my daily supervisor during the last five years. Andrea, your friendly behaviour, continued support and scientific guidance were invaluable to all the challenges I faced as a Master's student and PhD candidate at TU Delft. Thank you for your constructive criticism of my work and your motivation to keep enhancing the quality of my research.

I would like to offer my special thanks to all members of my doctoral committee for their assessment and useful comments on my thesis. I would also like to thank the anonymous reviewers who improved my journal publications through their constructive comments.

NWO, Team DSM, LaVision, WABCO, Sportzone Limburg, the ice rink in Leiden, Thialf, KNSB, Innovatielab Thialf, and Volkswagen AG collaborated on this dissertation. The outcome would not have been achieved without the help of these partners, to whom I owe my appreciation. Thank you also to all the individuals who made time for me to ride or skate through the Ring of Fire an uncountable number of times.

During the PhD, I had the opportunity to supervise some amazing master students. Luigi, Maximilian, Nikhil, Guus, and Laura, I hope that you learned at least as much as I did from your work and that you look back on it with the same positivity as I do. Special thanks to Luigi, Maximilian, Nikhil, who have directly contributed to significant portions of this thesis.

I need to thank the HSL's technical and administrative staff for helping and facilitating my work, by, for example, assisting me in the construction of enormous tunnels all around the Netherlands. Thanks to Frits for volunteering to try out the first Ring of Fire

on ice. Special thanks to Peter and Dennis for their support in the workshop, whether it was for work or to help me fix my race bike once again. I would like to thank Nico for ensuring that everything IT-related was functioning properly and I wish to thank Henk-Jan for guaranteeing and improving the safety of the lab. Finally, special thanks go to Colette for assisting me with all the bureaucratic procedures on several occasions.

I also want to give my thanks to all the fellow PhD candidates with whom I shared the office over the years. To Constantine, thank you for the close friendship. I really enjoyed the countless lunch runs, cycling adventures, triathlons, and swims in the Delftse Hout we experienced together. To Wouter, thank you for the support and supervision during my master thesis project, for the many discussions about cycling, and for assisting me during several experiments. To Edoardo, thank you for all the times you saved my day. You were always ready to help out, no matter how small or big my problem was. To Gabriel, Alessandro and Varun, thank you for the occasional distraction from work with some beers in 'De Atmosfeer'. To Sagar, I hoped that we could go cycling together before I finished my PhD, unfortunately, covid19 has prevented us from doing so. Maybe in the future, who knows! Thanks also to Alberto, Beppe, Christoph, David, Haohua, Jacopo, Jane, Jordi, Kushal, Luis, Martin, Ming, Mohamad, Tiago, Weibo, Xiaodong, Yi, and Zeno. Thanks for all the talks and discussions we had during all kinds of lectures, workshops, and conferences. I also quite enjoyed the time we spent together during the lunches, coffee breaks, barbecues, dinners, and other activities.

There is more to life than work and my life wouldn't be the same without my friends of JC BAM. I don't even know where to begin when thinking about the crazy things we shared together since we all arrived in Delft more than 11 years ago. Whether it was a diner, watching a movie, a trip abroad, or just having a coffee, spending my time with you guys could turn a week of bad results into a night to vaguely remember based on the pictures. Thanks for everything, and there is no doubt in my mind that we'll keep having fun in the future.

I cannot forget thanking my family. The amount of unconditional(!) support over the years has been truly invaluable. I realize I don't express my appreciation often enough, and I am not sure how to repay this 'debt', but I hope you being able to read through a 150-page thesis on sports aerodynamics is a good start.

This thesis is dedicated to my mother, a woman like no other, a woman I loved with all of my heart. I wish I could have shared this work with you — I like to think it would've made both of us proud.

Last but not least, Irene, thank you! There are not enough words to express how important you are to me, how much love and support you have given me throughout the years. Your smile, humor, encouragement, patience, and true love, made this journey more joyful and I am very happy to have been able to share it with you. For all the love and happiness we shared and for all the patience you dedicated to me, "Gracias".

CURRICULUM VITÆ



**Alexander Marc Carl Maartin Graad
SPOELSTRA**

31-07-1991 Born in Halle, Belgium.

EDUCATION

2010–2013 Bachelor Aerospace engineering
Delft University of Technology

2014–2017 Master Aerospace engineering
Specialisation: Aerodynamics
Delft University of Technology

2017–2021 PhD Aerospace engineering
Delft University of Technology

PROFESSIONAL EXPERIENCE

2015 Industrial placement
BMW group - Munich, Germany

2021 - present Data science consultant
ElastIQ-Connect - 's-Hertogenbosch, The Netherlands

AWARDS

2018 Higher Degree Research student Prize
12th Conference of the International Sports Engineering Association

2020 Best Paper award
13th Conference of the International Sports Engineering Association



LIST OF PUBLICATIONS

JOURNAL ARTICLES

Spoelstra A., Terra W. and Sciacchitano A. (2021) On-site aerodynamics investigation of speed skating. *Journal of Wind Engineering and Industrial Aerodynamics* (*under review*).

Spoelstra A., Sciacchitano A., Scarano F. and Mahalingesh N. (2021) On-site drag analysis of drafting cyclists. *Journal of Wind Engineering and Industrial Aerodynamics* 219 104797.

Spoelstra A., Hirsch M., Sciacchitano A. and Scarano F. (2021) Uncertainty assessment of the Ring of Fire concept for on-site aerodynamic drag evaluation. *Measurement Science and Technology*, 32(4):044004.

Spoelstra A., de Martino Norante L., Terra W., Sciacchitano A. and Scarano F. (2019) On-site cycling drag analysis with the Ring of Fire. *Experiments in Fluids*, 60(6):90.

CONFERENCE PROCEEDINGS

Spoelstra A., Terra W., Sciacchitano A. (2021) On-site aerodynamic investigation of speed skating. 14th Conference of the International Sports Engineering Association, West Lafayette, Indiana, USA.

Spoelstra A., Mahalingesh N., Sciacchitano A. (2020) Drafting Effect in Cycling: On-Site Aerodynamic Investigation by the 'Ring of Fire'. 13th Conference of the International Sports Engineering Association, online.

Spoelstra A. and Sciacchitano A. (2019) The Ring of Fire concept for on-site aerodynamic drag evaluation: a resolution assessment. SAE Commercial Vehicle Engineering Congress, Indianapolis, USA.

Spoelstra A. and Sciacchitano A. (2019) Accuracy assessment of the Ring of Fire system for on-site aerodynamic drag measurements. *Journal of Science and Cycling* vol 8, issue 2.

Spoelstra A., de Martino Norante L., Sciacchitano A. and Scarano F. (2018) An assessment of the Ring of Fire approach for indoor and outdoor on-site sports aerodynamic investigation. 19th International Symposium on Applications of Laser and Imaging Techniques to Fluid Mechanics, Lisbon, Portugal.

Spoelstra A., Terra W., Sciacchitano A. (2018) The Ring of Fire for in-Field Sport Aerodynamic Investigation. 12th Conference of the International Sports Engineering Association, Brisbane, Queensland, Australia.